Melanoma Detection Using Image Processing and Computer Vision Algorithms

Peyman Sabouri

A thesis submitted to
Auckland University of Technology
in fulfillment of the requirement for the degree of
Doctor of Philosophy

2016

School of Engineering, Computer and Mathematical Sciences

Abstract

Melanoma is the most serious form of skin cancer and is estimated to be the 19th most frequently occurring type of cancer worldwide, with approximately 232,000 new cases diagnosed in 2012. It is widely accepted that early diagnosis of melanoma significantly reduces morbidity, mortality and the cost of medication.

Computer-aided systems can be applied for a quantitative and objective evaluation of pigmented skin lesions to assist the clinical assessment process. Increasing innovation in non-invasive methods can be of significant help in the early detection of malignant melanoma, thus minimising the need for biopsies. The initial step is to analyse and develop efficient algorithms for melanoma detection. This thesis is mainly focused on two main areas: a) developing an efficient lesion border detection algorithm, and b) developing an efficient classification system.

For lesion border detection, several edge detection techniques are evaluated. We implemented a basic border detection algorithm on the ZYNQ-7000 System-on-Chips, which suggests a proper portable vision system could be designed for early detection of melanoma with high resolution and performance.

A semi-automatic algorithm consisting of eight steps is proposed for detecting the borders of skin lesions in clinical images. Using this approach, the user selects a small patch of the lesion to specify the foreground lesion area. The results show that the proposed method achieved the accuracy of 89.32%.

We present a multi-layer feed-forward deep neural networks (DNN) as a preferred lesion segmentation and recognition method. The algorithm can detect lesion borders without using any pre-processing algorithms; however, a pre-processing step e.g. hair removal and illumination correction has been essential in the previous systems.

In order to develop a classification system, we investigated two different approaches: a) using hand-engineered feature data that are extracted from the segmented lesion and b) using a deep learning method which learns features automatically from the original images.

The feature extraction algorithms that are used in this study are shape, colour and texture features. Correlation-based feature selection method is applied for feature selection. A performance evaluation of several supervised classifiers are discussed based on different feature sets. Two novel cascade classification architectures are proposed to improve accuracy. The second proposed cascade classifier achieved an overall accuracy of 83.3%, sensitivity of 85.1%, specificity of 80% and ROC area of 90% using ten-fold cross-validation.

Finally, we present a multi-layer DNN to distinguish melanoma from benign nevi as our preferred method for classification. Our preliminary work shows that networks trained with no preprocessed and segmented images, using directly learned features instead of applying feature extraction; achieved an average accuracy of 72.53%. However, a larger dataset and more investigations are required to train a better classifier.

Acknowledgements

Firstly, I would like to express my sincere gratitude to my primary academic supervisor, Associate Professor Hamid Gholamhosseini for the continuous support of my Ph.D study and related research, for his patience, motivation, and immense knowledge. His guidance helped me in all the time of research and writing of this thesis. It has been a great pleasure for me to have had a chance to work with him.

Special thanks to my second supervisor, Dr. John Collins for his support, guidance and helpful suggestions throughout this research work. His guidance has served me well and I owe him my heartfelt appreciation.

I would like to thank my loving wife Hoda Nozari for her great patience, love and unequivocal support throughout, who was always standing by me in my hard times during this work. Hoda has supported me in each and every way, believed in me permanently and inspired me in all dimensions of life.

I also wish to thank my parents, Maryam Zinatbakhsh and Faizallah Sabouri, for the emotional and financial support through this period of my life.

In addition, I wish to thank AUT University for providing me postgraduate scholarship and summer research award from the faculty of Design and Creative Technologies-AUT.

Dedicated with extreme gratitude to

My beloved family,

Dr. Hamid Gholamhosseini,

And all of my friends,

Without whom none of my success would be possible.

List of Publications

Conferences Papers:

- P. Sabouri, and H. Gholamhosseini, "Computer vision and image processing for diagnosis of melanoma using clinical images", presented at the meeting of the *13th International Conference on Neuro-Computing and Evolving Intelligence 2015 (NCEI'15).* Auckland, New Zealand, February 2015.

- P. Sabouri, H. Gholamhosseini, T. Larsson, and J.Collins, "A cascade classifier for diagnosis of melanoma in clinical images", presented in *Engineering in Medicine and Biology Society (EMBC), 2014 36th Annual International Conference of the IEEE.* IEEE, USA, 2014, pp. 6748–6751.

- P. Sabouri, and H. Gholamhosseini, J. Collins, and M. M. Baig, "Smart skin cancer diagnosis using advanced embedded vision systems", presented at the meeting of the *Annual Health Informatics New Zealand (HINZ).* Rotoroa, New Zealand, November 2013.

Book Chapter:

- P. Sabouri, H. Gholamhosseini and J. Collins, "Border detection of skin lesions on single system on chip", in *Advanced Technologies, Embedded and Multimedia for Human-centric Computing.* Springer, 2014, pp. 465–471.

Journal Papers:

- P. Sabouri, H. Gholamhosseini and J. Collins, "Border Detection of Melanoma Skin Lesions on a Single System on Chip (SoC)", *Journal of Computer (JoC)*, vol. 25, pp. 28–34, 2014.

Accepted Conference Papers:

- P. Sabouri and H. Gholamhosseini, "Lesion border detection using deep learning", accepted in *IEEE Congress on Computational Intelligence (WCCI)*, IEEE 2016. Presented: July 2016.

Contents

Attestation of Authorship

I hereby declare that this submission is my own work and that, to the best of my knowledge and belief, it contains no material previously published or written by another person (except where explicitly defined in the acknowledgements), nor material which to a substantial extent has been submitted for the award of any other degree or diploma of a university or other institution of higher learning.

Peyman Sabouri _____

List of Figures

List of Tables

List of Abbreviations

ACC Accuracy

ALU Arithmetic Logic Unit

ANN Artificial Neural Network

APU Application Processor Unit

AUC Area Under Curve

CAD Computer Aided Diagnosis

CCD Charge-coupled Device

CDE Colour Distribution Entropy

CFS Correlation-based Feature Selection

CMOS Complementary Metal Oxide Semiconductor

CNN Convolutional Neural Network

CPU Central Processing Unit

CT Computed Tomography

DNN Deep Neural Network

DPR Dynamic Partial Re-configuration

DSP Digital Signal Processor

ELM Epiluminescence Microscope

EPP Extensible Processing Platform

FPF False Possitive Fraction

FPGA Field Programmable Gate Array

FSS Feature Subset Selection

FW Feature Weighting

GLCM Grey-Level Co-occurrence Matrix

GPP General Purpose Processor

GPU Graphics Processing Unit

HDL Hardware Description Language

HLIF High-Level Intuitive Features

HLS High Level Synthesis

HSI Hyper Spectral Imaging

HSV Hue-Saturation-Value

HW Hardware

ICA Independent Component Analysis

IP Intellectual Property

KNN K Nearest Neighbours

LoG Laplacian of Gaussian

MCU Micro Controller Unit

MLP Multi-layer Perceptron

MRI Magnetic Resonance Imaging

NB Naive Bayes

PCA Principal Component Analysis

PMD Percentage Mammographic Density

PSL Pigmented Skin Lesion

RBF Radial Basis Function

ReLU Rectified Linear Unit Layer

RGB Red-Green-Blue

ROC Receiver Operating Characteristic

ROI Region of Interest

RTL Register Transfer Level

SE Sensitivity

SoC System-on-Chip

SP Specificity

SVM Support Vector Machine

SW Software

TBSI Total Body Skin Imaging

TI Texas Instruments

TPF True Possitive Fraction

USA United States of America

UV Ultraviolet

WBP Whole Body Photography

Chapter 1

Introduction

1.1 Research Motivation

Skin cancer is among the top twenty most common cancers and it can be divided into two main categories: melanoma and non-melanoma. Malignant melanoma is one of the leading causes of death due to skin cancer [1]. While prevention of this malignancy is the best approach, early diagnosis of existing melanoma is crucial. One reason is that melanoma generally develops on the skin surface; however, it can metastasise to other parts of the body if it is not detected in its early stages. When melanoma is detected in an early stage of its development, it is highly treatable; thus, early detection can significantly reduce morbidity, mortality and cost of medication [2].

The clinical reference standard for melanoma diagnosis is visual examination of skin lesions by a dermatologist, followed by biopsy and histopathological analysis. In a visual examination, dermatologists decide which moles are of interest based on size, border, shape, and colour. It is well known that early stage melanomas can be difficult to diagnose in some circumstances. The main problem is that a melanoma may mimic a benign melanocytic/non-melanocytic lesion and vice versa [3]. Dermatologists' accuracy varies [4] and this is an issue of concern. It has been reported that the overall estimated sensitivity (percent of melanoma diagnosed as melanoma) is around 80% [5].

Several non-invasive methods have been developed to improve dermatologists' discrimination of melanomas from benign nevi. In recent years, multi-spectral and hyper-spectral imaging systems have led to renewed interest in the diagnosis of melanoma [6, 7]. The dermoscope is another non-invasive imaging device for the diagnosis of pigmented skin lesions (PSLs) such as melanoma. This device illustrates

pigmented lesions clearly and visually; however, the accuracy is less than 85% and it is highly dependent on the opinion of a well-trained dermatologist. Unfortunately, even with dermoscopy, it is still a challenging task for dermatologists to distinguish some melanomas from other lesions [3].

Computer aided diagnosis (CAD) systems and image processing, used to help skin cancer specialists achieve better detection of melanoma, have been widely studied in the last two decades. This idea was first proposed around 1985 [5]. Using image processing, skin lesion images are assessed to detect certain features that expect to be characteristic of malignancy. For instance, melanoma's characteristics such as asymmetrical shape, irregular border, colour variety and diameter greater than 6 millimetre [8] can be extracted using high performance image processing techniques.

However, these approaches are not considered to be the best diagnostic method or an alternative for histopathology and they are mainly used for educating clinicians by using image processing and computer vision techniques as a second opinion at the primary health care level [8, 9].

As stated by Tyagi et al. [10], "While early detection is key to improved melanoma survival in general, adherence to screening guidelines is low; with population-based estimates of approximately 26% for physician-based skin cancer screening and 20-25% for skin self-examination. The individuals in certain populations are at increased risk of poor outcomes as a result of advanced-stage diagnosis."

A potential new technique for skin screening and melanoma detection is the development of innovative digital patient-oriented "e-Health" devices that are low-cost and widely available [11]. These could help to reduce the practical and psychological issues relating to the early detection of melanoma.

Increasing innovation in non-invasive methods can significantly improve the early detection of malignant melanoma as an alternative to biopsy. Therefore, developing novel methods may lead to increasing accuracy in melanoma detection. Furthermore, due to the rapid growth of embedded system applications, there has been a great opportunity to develop portable vision systems for medical diagnosis and applications, with good resolution and performance. Portable devices enable diagnosis in remote locations for patients who do not have access to expert dermatologists at an affordable cost [12].

1.2 Research Objectives

- **Use of Clinical Images Instead of Dermoscopy Images:**

  In order to develop such a portable application the first step is image acquisition. There are various methods for image acquisition of skin lesions, such as clinical photography, dermoscopy, and multi-spectral and hyper-spectral imaging. For instance, the significant difference between dermoscopic and clinical image acquisition is in screen visualisation of a lesion [8]. Clinical images illustrate skin lesions on the surface of the skin, similar to what a dermatologist observes with the naked eye [5]. Figure 1.1 shows two lesion photographs that are captured by a normal camera and a dermoscopy device[1].

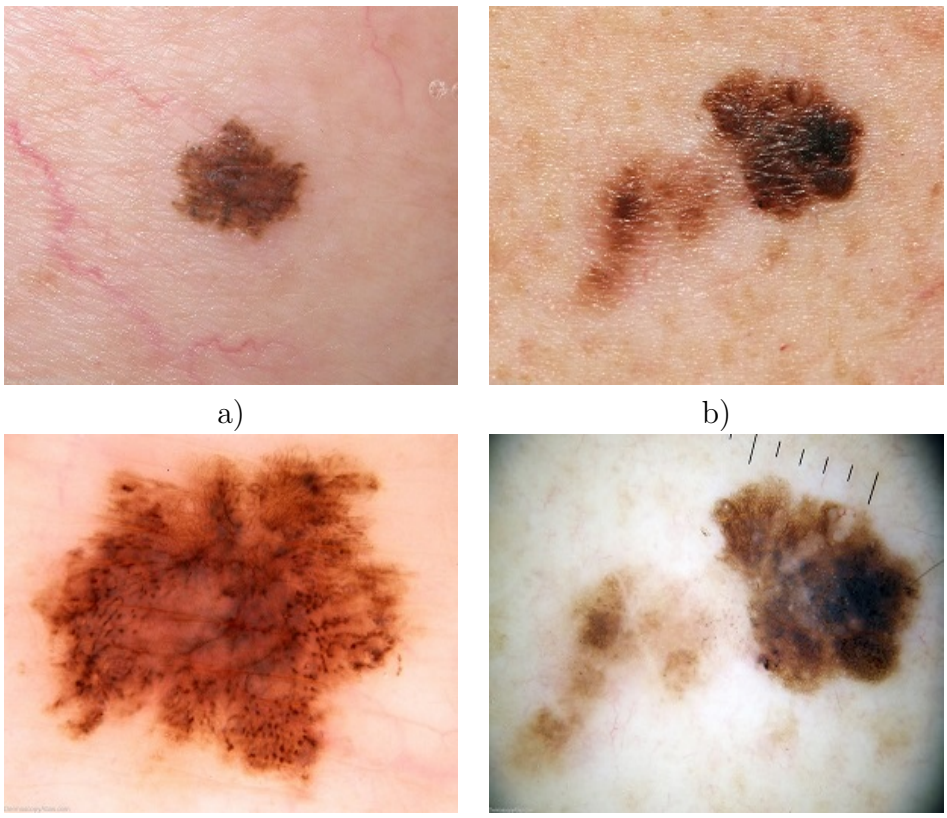

a) b) c) d)

Figure 1.1: Clinical images (top) versus dermoscopy images (bottom); (a) and (c): in-situ melanoma, (b) and (d): invasive.

  It has been reported that using diagnostic dermoscopy is more accurate than other traditional examinations employed by experts; however, this tool is less common in the USA than in Australia and Europe [13]. The main advantage of using clinical images in the proposed system is that it allows the user to scan lesions as simply as possible via a normal camera compared with other types of visual detection devices such as dermoscopy. In addition, it is more

[1]source: http://www.dermoscopyatlas.com with permission.

affordable and not necessary to use extra devices or specific conditions for photography (e.g. applying gel or controlling lighting conditions).

Difficulties arise, however, when attempts are made to create image processing algorithms to increase the accuracy of the system. Image processing of clinical images collected in uncontrolled conditions and unknown environments is more challenging compared with the processing of standard dermoscopy images.

- **Lesion Border Detection:**

  This study attempts to investigate the current methods used in melanoma CAD systems and consider new techniques for creating a practical system for the diagnosis of melanoma.

  The presence of artefacts such as hairs, ruler marks, variable illumination and shadows in clinical images may affect segmentation and result in imperfect feature extraction. Therefore, preprocessing of melanoma images, which is the process of removing these artefacts, is essential and is a major area of interest in the field of computer-aided diagnosis of melanoma. Following the preprocessing of skin images, lesion segmentation (border detection) is performed in order to separate the undesirable background skin section from the foreground lesion. One of the issues that arose in this study was lesion segmentation where each image was captured via a different camera in uncontrolled settings. There are various factors that may result in imperfect segmentation; for example, an image from a public dataset may have high light illumination inside the lesion or may have hair artefacts. In addition, usually the region of interest (ROI) of the lesion and surrounding skin is located on a curved surface, and this may produce a shadow on the image and therefore imperfect segmentation. Another objective of this study is to find an efficient technique for lesion border detection which requires the minimum use of image preprocessing computations.

- **Melanoma Classification:**

  After performing lesion segmentation, feature extraction is an important step to extract meaningful attributes from the segmented lesion. We need to use features that characterise the lesion and are not detectable using the naked eye. These features should interpret the visual signs of melanoma that are similar to the clinical ABCD rule in dermatology (ABCD rule is explained in Section 2.3.1). In addition, feature selection should be applied in order to find the best and most practical feature set, with the highest impact for classification accuracy. An objective of this study is to find an efficient technique for lesion classification (distinguishing melanoma from benign nevi). We investigate feature extraction by applying shape, colour and texture analysis and then

finding the most powerful set to diagnose melanoma. Following feature extraction and selection of the optimal feature set, we need to apply classification in order to diagnose the mole as a melanoma or benign nevi. Another objective of this study is proposing cascade classification architecture to achieve a high accuracy with high sensitivity and specificity. In addition, we investigate the use of deep neural networks for melanoma detection.

- **Investigation of an Embedded System for Implementation of Image Processing Algorithms:**

  Recently, with the revolution in the production of smart-phone devices, developing medical applications that run on mobile devices has become a high priority in the health science field. Modern mobile devices include mega-pixel cameras, multi-core CPUs/GPUs and a collection of sensors. Smart-phone sensors can be set up to distinguish a broad range of medical applications such as cough diagnosis, irregular heartbeat diagnosis, and lung function assessment [14]. "The ability to diagnose ailments in the convenience of patients' homes using smart-phones that they already possess could lead to early detection, which could ultimately reduce health-care costs", stated by Agu et al. [14].

  A number of smart-phone applications related to melanoma diagnosis have been developed for both Android and Apple phones. For instance, Wadhawan et.al. developed a portable library to detect skin cancer automatically, using an iPhone-4 smart phone; however, its performance in reality is not promising [15]. Chadwick et.al. reviewed available skin cancer detection applications running on different mobile platforms (e.g. Apple and Android devices). They tested five applications using 15 images of previously diagnosed skin cancers (tested by biopsy) and compared the risk accuracy to the recognised histopathologic diagnoses of the lesions. The results of this study indicated that current CAD lesion analysis applications in the market are as yet neither reliable nor ready for use as a triage tool [16].

  The ultimate objective of the research was to investigate and develop fast and efficient embedded vision algorithms for implementation of melanoma detection. It could be implemented on an embedded system such as fast system-on-chip SoC technologies such as Field Programmable Gate Arrays (FPGAs) devices or Digital Signal Processors and Graphical Processor Units (DSPs/GPUs), or could be integrated as a medical application on smart phones or tablets. However, the first step and main focus of this thesis is to analyse and develop efficient algorithms for melanoma detection. In a general melanoma diagnosis system, the major components of the system are image acquisition, image pre-processing, border detection, feature extraction and classification.

ZYNQ-7000 System-on-Chip (SoC) platform is investigated in terms of speed of processing and feasibility of implementation of image processing and computer vision algorithms on the hardware and software sides of this platform.

1.3 Research Contribution

The primary contributions of this research are as follows:

- **Data Collection:**

  A first step in this study was data collection. A collection of 650 clinical images was collected from on-line web resources [17–21] to be used for image analysis and to develop the system. The following image problems were excluded from the collection in order to generate the dataset:

  - poor-quality images,
  - images with uncertain class labels,
  - images in which the ratio of the size of lesions was very low in comparison with other images,
  - images in which significant numbers of hairs covered the surface of the lesion.

  Each image was cropped so that the lesion was located in the centre of the image and then each sample was resized to 512 $\times$ 512 pixels. The generated dataset contained 400 images and was divided into two groups: melanoma and non-melanoma. There were 195 images of melanoma and 205 images of benign nevi. The dataset of non-melanoma images included atypical (compound, junctional, dermal, and combined), dysplastic, seborrheic keratosis, blue nevus, congenital, spitz, halo and neurofibromatosis. Information about clinical images is provided in Section 2.3.1.

- **Development of Lesion Border Detection Algorithm:** One of the main contributions of this study was to develop a fast and efficient algorithm to enable border detection to be implemented on a portable system. We proposed three different techniques as follows:

  - **Based on Image Edge Detection Techniques:** Several edge detection methods were investigated after applying morphological operations as the pre-processing step for border detection of melanoma images. We considered this method due to its speed and computational simplicity.

  - **Based on Colour features:** A semi-automatic method for lesion segmentation of clinical images based on lesion colour features was developed in order to improve the accuracy of border detection.
  - **Based on Convolutional Neural Network (CNN):** A novel border detection approach based on CNNs was developed. The main reason for proposing this method is that it would be able to recognize lesions without needing a pre-processing approach. We tested our method based on the most challenging images in the literature and achieved good results compared with other methods.

- **Hardware Implementation on ZYNQ-7000:**
  - Investigation of the state-of-the-art platforms for creating hand-held medical imaging applications and evaluation of the required Hardware/Software techniques for efficient and rapid prototyping design.
  - Developing the image acquisition system followed by a border detection algorithm which works successfully with a number of image and video LogiCore IPs implemented on the FPGA (logic programming) side and with related software running on the ARM processor (software programming) side. The border detection algorithm also includes morphological filters for applying hair removal for preprocessing of images. The main advantage of the proposed implemented embedded system is that it is reconfigurable so that the implemented IP can be modified/changed to suit other methods.

- **Feature Extraction and Lesion Classification:**
  - Feature extraction based on shape, colour and texture features.
  - Investigation of accuracy of several supervised classifiers based on extracted features.
  - Designing a two-stage cascade classifier using SVM to increase accuracy.
  - Designing a cascade classifier with rejection criteria at the first stage of the classifier to increase the reliability of classification and achieve higher performance for the diagnostic system
  - Developing a multi-layer deep neural network for melanoma detection. A deep learning model based on convolutional neural network is proposed for melanoma detection. The main advantages of the proposed model is that it can learn feature of melanoma without applying feature extraction and feature selection methods. Another point of this model is that it can detect melanoma even better than applying segmentation step.

1.4 Thesis Structure

Following this introduction, the thesis is structured into six chapters:

- **Chapter 2:** presents background information about skin cancer and melanoma. In addition, it provides a literature review and background of the current CAD systems, including previous work in lesion segmentation, feature extraction and classification.
- **Chapter 3:** deals with embedded vision platforms used for the implementation of image processing algorithms and provides information about hardware and software programming of the proposed system.
- **Chapter 4:** describes the proposed method for lesion segmentation including experimental results and discussion.
- **Chapter 5:** describes the methodologies used for feature extraction.
- **Chapter 6:** deals with the methods proposed for image classification. Performance of various supervised classifiers are analysed for discriminating melanoma from benign nevus based on selected features. Two novel cascade classification architectures are presented to improve reliability as well as the accuracy of the system.

  In addition, we investigate the use of deep learning based on supervised and unsupervised methods. It compares the result of proposed model using segmented images and raw (no segmentation and pre-processing) images.
- **Chapter 7**: includes overall conclusion and discusses the future direction of the research.

Chapter 2

Background and Literature Review

2.1 Introduction

The purpose of this chapter is to review the literature on clinical and computer-aided diagnostic approaches used for melanoma examination. It begins by providing a brief summary of the human skin's structure, the nature of malignant melanoma and the existing screening tools. Clinical methods and current computer-aided approaches used in melanoma detection are described. This chapter also reviews the existing image processing methods as applied to the development of melanoma CAD systems, and recent works that have used deep neural networks based on general machine vision application are reviewed.

2.2 The Human Skin Structure and Malignant Melanoma

The epidermis, the dermis and the hypodermis (also called as subcutaneous) compose the three main layers of human skin. Each of these connected layers has an important role (Figure 2.1) [22]. The dermis is made of collagen (a type of protein), and elastic fibres. It contains two layers: a) the papillary dermis (thin upper layer) that contains the epidermis and dermis; and b) the reticular dermis (thick layer) consists of blood and lymph vessels, nerve endings, sweat glands and hair follicles. It supplies energy and nutrition to the epidermis and is a key factor in thermo-regulation, healing and the touch sensation [22–24].

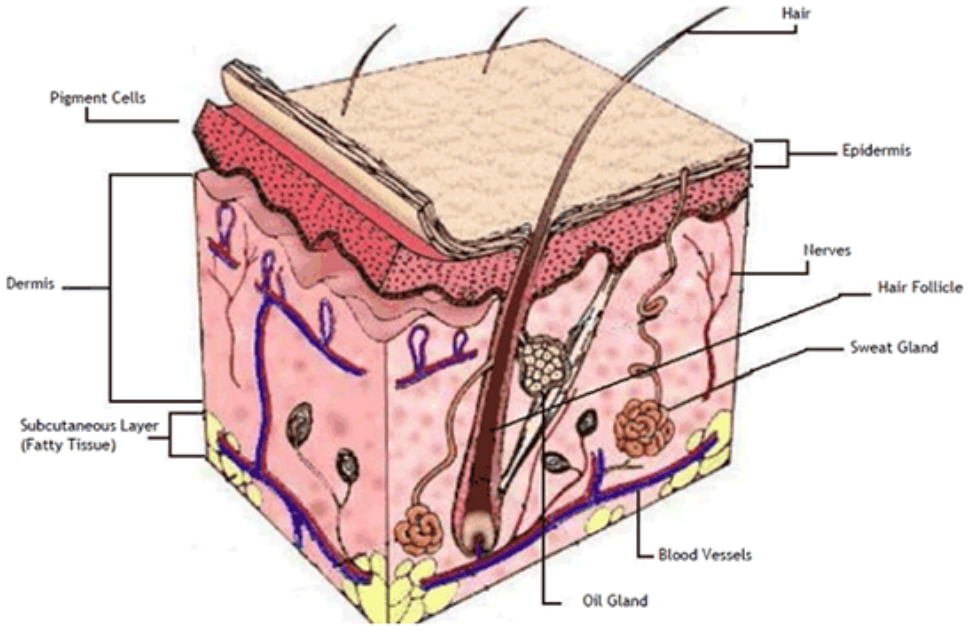

Figure 2.1: Skin's anatomy illustrating the epidermis, the dermis and the subcutaneous (hypodermis) layers (source: americanskin.org).

The epidermis is the protecting (outermost) layer of the skin, which can be divided into four layers: basal layer (Stratum Basale); stratum spinosum; stratum granulosum; and stratum corneum. There are four types of cells in the epidermis: keratinocytes (95% of cells), melanocytes, Langerhans' cells and Merkel cells [25]. The melanin produced by melanocytes can spread to the surrounding keratinocytes [25]. This procedure can be increased by tanning reactions to sun exposure or Ultraviolet UV radiation and may increase the possibility of malignant transformation. Basal cell carcinoma and squamous cell carcinoma are the most common types of skin cancer and develop from non-pigmented basal and squamous keratinocytes; malignant melanoma is less frequent but is much more dangerous and sometimes fatal [26].

2.2.1 Global Prevalence of Melanoma

Melanoma is the deadliest form of all skin cancers and is estimated to be the 19th most frequent cancer worldwide, "With approximately 232,000 new cases diagnosed in 2012" [27]. The prevalence of melanoma is highest in New Zealand/Australia and lowest in South Africa and south-central Asia [26]. According to the Ministry of Health of New Zealand [28], this country had an age-standardised rate of 42.8 per 100,000 in men and 33.6 per 100,000 in women in 2009. The World Health Organisation (WHO) estimates that "the current rate of new melanoma cases annually is 132,000 worldwide, and one in every five American citizens is expected to develop malignant melanoma in their lifetime" [29]. The average age for diagnosis

of melanoma in the USA is 61. Although the melanoma incidence rate in USA is said to be less than 2%, it causes death in many cases; the risk of melanoma among the white population is more than 20 times that in African Americans [26, 30]. In Europe, the mortality rate of melanoma was estimated, showing that Switzerland ranked the highest while Romania and Greece ranked the lowest [31].

2.2.2 Types of Melanoma

The most common form of melanoma, encompassing 70% of melanomas, is superficial spreading melanoma, which frequently appears in a pre-existing mole (benign nevus). Other types include nodular melanomas as the second most commonly occurring (15-30%), lentigo malignant (5%) and acral lentiginous melanoma, which accounts for 2-10% of melanomas [32].

2.3 Screening of Melanoma

Photography has been widely employed as a standard tool in dermatological practice in both the health care and research environments [33]. Nowadays, with the development of low-cost and practical imaging systems, clinicians can take advantage of medical images with higher quality resolution of the region of interest. There are various clinical criteria for the differential diagnosis of melanoma and benign nevi. However, performing these tests often requires special imaging techniques and experience. Screening PSLs helps clinicians and dermatologists obtain better realisation and observation. It is also useful for documenting and registering PSLs. One of the significant benefits of lesion documentation is that clinicians can track evolution and changes in the lesion over time. There are two standard melanoma screening methods that are widely used in primary health care and research studies: clinical photography and dermoscopy. There are other non-invasive screening devices in this field such as multi-spectral or hyper-spectral imaging systems; but because one of the aims of this research was to develop a portable system and because of the limited access to medical image databases that we encountered in this study, this thesis deliberately did not focus on other imaging techniques. Before describing the clinical criteria, it is worth pointing out the similarities and differences between clinical photography and dermoscopy.

2.3.1 Clinical Images

Clinical imaging or clinical photography provides a traditional screening method for pigmented skin lesions in which images are captured from the surface of the skin using a customer-grade camera. It represents the region of interest, "similar to what a clinician observes with unaided eye" [5]. The term clinical photography can also refer to macroscopic images or dermatologists' pictures. Clinical images are useful for documenting PSLs and registering their locations on the human body in order to track changes over time. Total body skin imaging (TBSI) and whole body photography (WBP) are two clinical methods of scanning the whole human body [34]. The most important parts that should be scanned are the face, the ears, the anterior, posterior and palms and soles [35]. It has been reported that one advantage of using this method is that it helps the patient to feel less anxiety compared with other methods [36, 37].

2.3.2 Dermoscopy

Dermoscopy is a non-invasive imaging method that has been used widely for the screening of PSLs. A dermoscope (also known as an epiluminescence microscope (ELM)) as is a hand-held device for magnifying and visualising the patterns and substructure of a lesion that are not visible to the naked eye [38].

These features include pigment networks, dots, globules, branched streaks, streaks, structure-less areas, blotches, regression, blue-white veil, milia-like cysts, comedo-like openings, fingerprint-like structures, moth-eaten borders, fissure ridges or brain- or leaf-like areas, wheel-spoke-like structures, and large blue-grey ovoid nests [39]. The user needs to apply a liquid such as gel, oil or alcohol to the skin and analyse the pigmented lesion by contacting it with the dermoscope.

In expert hands and when used by trained general practitioners, dermoscopy has been shown to improve both the sensitivity and specificity of melanoma diagnosis, elevating the diagnostic accuracy by 5%-30% [40, 41].

2.3.3 Spectral Imaging

Recently, Hyper Spectral Imaging (HSI) has been used for the analysis of physiologic and pathologic developments in living tissue in animal and human studies, to investigate the health or disease of tissues [42]. HSI could be a useful tool for diagnostic procedures to determine healthy/unhealthy tissues. HSI is a remote sensing technol-

ogy that provides images, which contain multiple optical spectral data in each pixel. The combination of these images is called a hypercube, where the two-dimensional image captures the spatial features of an object and the third dimension shows the spectral wavelength [43]. The HSI has also been used in non-medical applications e.g. satellite investigations to determine different type of area such as chemical weapons production and agricultural fields [44]. In HSI the spectrum of each pixel is correlated with the presence and concentration of various chemical species. HSI is a method of 'imaging spectroscopy' in which the light element is separated into several wavelengths using a spectral separator and collected using a charge-coupled device (CCD) or a complementary metal oxide semiconductor (CMOS) by an ordinary camera [45]. Figure 2.2 illustrates an overview of a spectral imaging system.

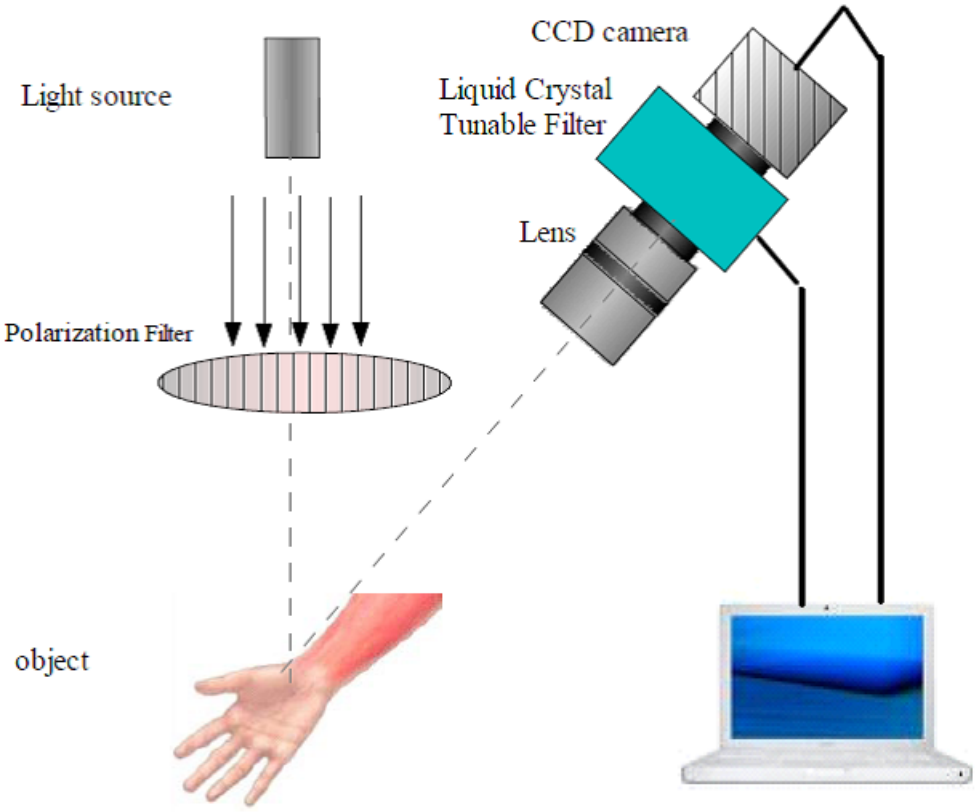

Figure 2.2: An overview of spectral imaging system for skin cancer detection [46]

To date, a number of spectral imaging systems designed for use in skin cancer detection have been developed, in which the processing system is based on CPU-based desktop computers [46–55]. A basic HSI method uses a sequence of 2D images which are captured in different wavelengths by adding a rotating filter on the lens of camera (Figure 2.3).

As mentioned in Chapter 1, we decided to work on clinical images instead of other dermatological screening types. The main advantage of using clinical images

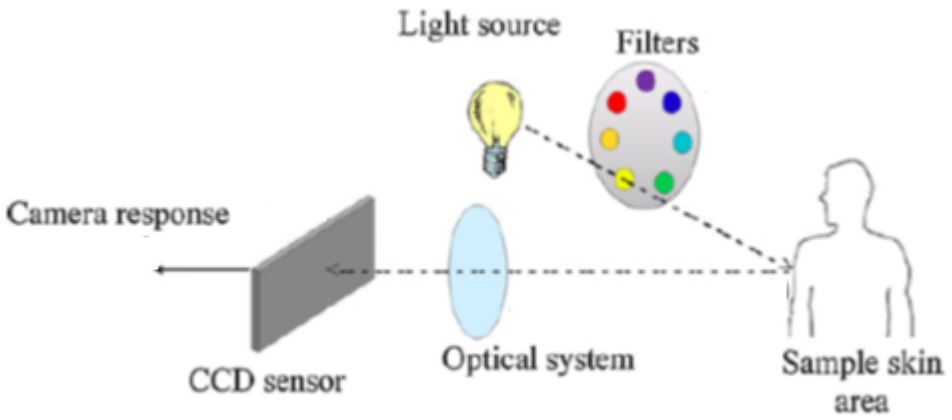

Figure 2.3: An overview of the spectral model of the acquisition process in a multi-spectral system [48].

over dermoscopy is the simplicity, and it allows the user to scan lesions via a typical camera. This approach is also more accessible and does not need extra devices such as dermoscopes or specific conditions for photography.

2.4 Clinical Criteria for Melanoma Diagnosis

Various methods have been introduced and adapted for melanoma detection, using either clinical images or dermoscopy. A list of diagnostic criteria and corresponding imaging methods is provided in Table 2.1. This table shows that only two methods are adaptable for clinical images: the ABCD rule and Glasgow's 7-point check-list. Since our image dataset is based on clinical photographs, we only describe these two methods that can be applied for our images.

Table 2.1: Clinical diagnosis methods and related screening tools [8, 56].

Clinical Criteria	Clinical Images	Dermoscopy Images
ABCD(E)	yes	yes
Glasgow 7-point checklist	yes	no
7-point checklist	no	yes
Pattern analysis	no	yes
Menzies' method	no	yes
7 feature of melanoma	no	yes
3-point checklist	no	yes

2.4.1 ABCD Rule

The ABCD rule is a clinical method proposed in 1985 by Friedman et al. [57]. This approach has been widely used, mainly because of its ease of use in assigning the lesion to benign, suspicious or malignant categories [58]. In this method, the lesion is analysed using four criteria: (A) Asymmetry, (B) Border irregularity, (C) Colour variegation and (D) Diameter, which is normally greater than six millimetres [59, 60]. Recently another important criterion has been added to expand the ABCD rule to the ABCDE rule. The term E (evolution) describes the measurement of changes such as size, shape, and texture and colour of the surface of the lesion over a given period of time [59]. Table 2.2 shows the difference in definitions of the ABCD(E) rule between clinical images and dermoscopy.

Table 2.2: Difference of ABCD(E) rule in clinical and dermoscopy images.

Criteria	Clinical photography	Dermoscopy
A	Asymmetrical shape	Asymmetrical counter, colour and structure
B	Irregular border	Border sharpness, cut-off pigmentation
C	Colour variation	Colour variation
D	Diameter > 6mm	Differential structure
E	Changes in size	Changes in size, Colour and pattern

2.4.2 Glasgow's Seven-point Check-list

The expansion of E (evolution) adds three major criteria to the ABCD rule. The idea of lesion evolution is emphasised more in Glasgow's 7-point check-list, which highlights changes in size, shape, and colour as major features for early melanoma detection [61]. However, there are four minor criteria in the Glasgow's seven check-list (including sensory change, diameter of 7 mm or greater, and the presence of inflammation, crusting or bleeding) that are not easy adaptable by clinicians [59, 61, 62]. Table 2.3 also demonstrates the differences between the Glasgow (clinical images) and dermoscopy seven-point check-list .

Table 2.3: Variation of definition in seven-point checklist criteria [59].

Criteria	Clinical images	Dermoscopy images
(1)	Changes in size	Atypical pigment network
(2)	Changes in shape	Blue-whitish veil
(3)	Colour variation	Atypical vascular pattern
(4)	Diameter greater than 7mm	Irregular streaks
(5)	Inflammation	Irregular dots/globules
(6)	Crusting or bleeding	Irregular blotches
(7)	Sensory change	Regression structures

According to the table above, there are significant differences in interpretation of the seven-point check-list method in clinical and dermoscopy photographs. Therefore, one should consider certain feature extraction methods and algorithms for image analysis of clinical or dermoscopy images. For example, a pattern recognition algorithm can be applied to detect atypical pigment network in dermoscopy images. By contrast, shape analysis can be applied to detect change in size of the lesion in clinical images.

2.5 Computer-aided Analysis of Melanoma

A computer-based melanoma diagnostic system or a computer-aided diagnostic system (CAD) can be used for quantitative and objective evaluation of PSLs to assist clinical assessment. Such systems can be used to provide a second opinion for physicians, allowing automatic and semi-automatic diagnosis to overcome the variability of observation and the challenging tasks that occur in dermatologists' examinations. Figure 2.4 illustrates five essential components for the development of melanoma CAD tools. These components, which are in fact an image processing algorithm, are deployed in a CAD system with the end goal of diagnosis of the type of lesion. This section reviews image processing algorithms that have been used for the development of CAD of melanoma based on clinical images rather than dermoscopy images and each subsection deals with a separate group of the literature classification.

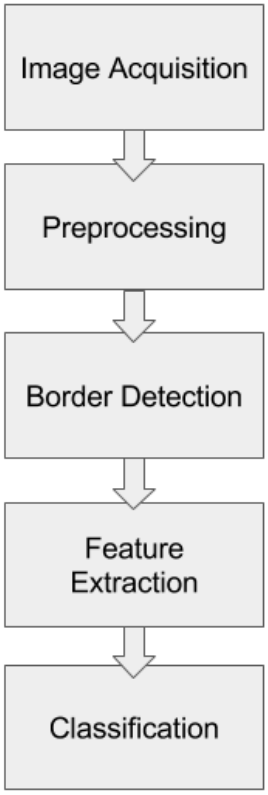

Figure 2.4: Components of a melanoma CAD system.

This section reviews image processing algorithms that have been used for the development of CAD of melanoma based on clinical images rather than dermoscopy images and each subsection deals with a separate group of the literature classification.

2.5.1 Image Pre-processing

This component is used between the image acquisition and border detection steps and is mostly performed in order to enhance the border detection accuracy by correcting/removing undesirable imaging information. The presence of artefacts such as hairs, ruler marks, and variable illumination in clinical and dermoscopy images may affect the following steps, such as segmentation, and thereby cause imperfect feature extraction results [63]. Existing research has primarily focused on two distinct areas: artefact (e.g. hair) removal and image enhancement (illumination correction).

2.5.1.1 Hair Removal

Hair removal is the principal task in the preprocessing step, with the aim of removing existing hairs in the image with the help of software rather than shaving. The

challenge is to remove occluded hairs on PSLs compared with the regular part of the surface. However, use of hair removal algorithms depends on the image dataset. Based on our experiments, if there is no hair in a particular image, applying these algorithms may change the lesion's patterns. In addition, if significant numbers of hairs covered the surface of the lesion, applying these algorithms may significantly change the lesion's pattern.

The literature has emphasised the importance of this step. Lee et al. (1997) proposed the first method of hair removal from dermoscopy images [64] and since then this approach has been widely adapted and improved [65–70]. This algorithm performs three main tasks: 1) Detecting the location of dark hairs in the image using morphological filters; 2) Replacing the identified hairs with neighbouring pixels; and 3) Applying an adaptive median filter to smooth the final image. Several other studies have been carried out to remove hair artefacts, especially dark ones that are more dominant than other artefacts, particularly in dermoscopy images [70–73]. These hair rejection algorithms can be divided into two steps: hair detection and hair restoration. Hair restoration is a necessary step and consists of filling the detected hairs with suitable intensity values; however, this may corrupt the texture of the PSL and cause imperfect texture analysis or border detection. According to the literature, most hair removal algorithms that have been proposed for clinical images are based on median filtering [66, 74, 75]. The median filter is effective for removing noise spikes that cover a few pixels [74]. For instance, Zagrouba and Barhoumi (2004) applied median filtering to reduce the weight of small structures for thin hairs (e.g. blond hairs), and used DullRazor for thick hairs. Also, they used a Karhunen-Loeve transform to enhance the edges of the lesion against the surrounding skin [66].

In recent work, Abass et al. [76] proposed an automatic feature-preserving hair removal algorithm for dermoscopy images. The proposed algorithm was tested on 100 dermoscopy images. In addition, they compared their work with two in-painting methods such as non-linear partial differential equations (PDE) and exemplar-based repairing approaches, and as well as a linear interpolation method. The proposed algorithm outperformed the others, with an accuracy of 93.3%.

The hair removal issue has not completely addressed in previous studies. There is no hair detection algorithms reported to detect hair first and then decide to remove them. Applying most of these algorithms might change the pattern of the lesion. Development of a hair removal algorithm is not the objective of this study and we used DullRazor software for removing hairs in our image dataset (described in Chapter 4).

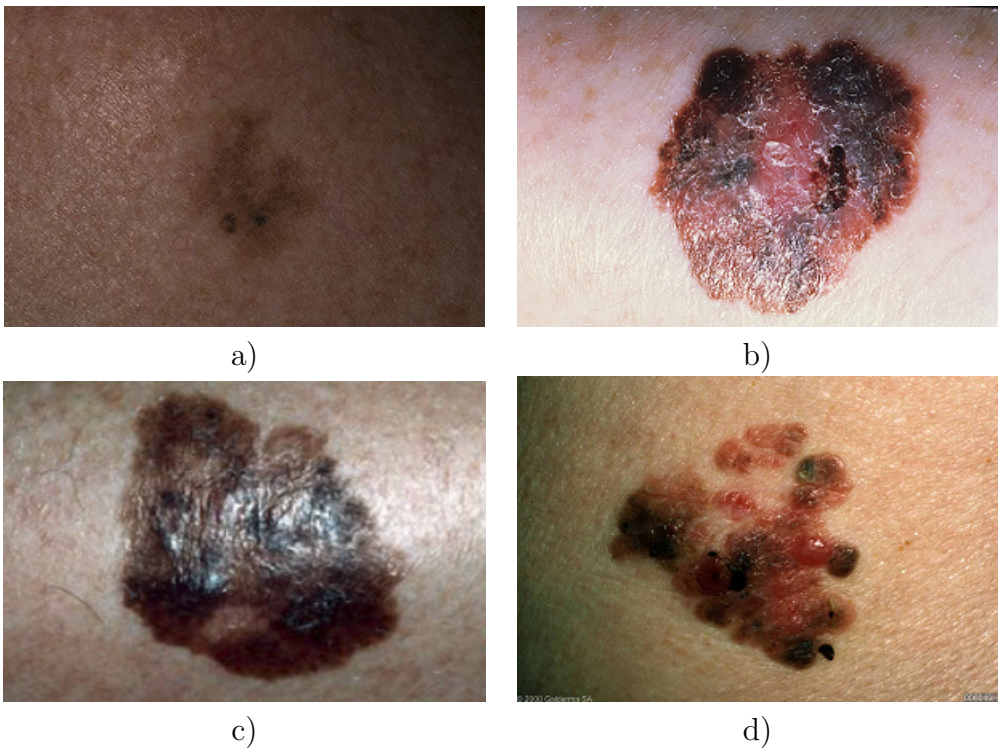

a) b)

c) d)

Figure 2.5: Example of images including shading and illumination issues.

2.5.1.2 Illumination Correction:

Reflected illumination from the skin surface can result in misclassification of skin lesions. For instance, see the shading and highlight effects in Figure 2.5 (a-c): the healthy section of the skin is covered by shadows and highlights and appears similar to the colour of the lesion. Another example is shown in Figure 2.5 where bright/intense highlight reflection impacts colour features within the lesion area (specular reflection).

Several techniques have been reviewed for enhancing both shading and illumination effects. Although there has been a considerable amount of research in this area, few studies have focused on clinical and dermoscopy images. Several techniques such as morphological filters, bilateral filters and Monte Carlo sampling have been used for estimation of illumination [77]. Most of the available methods are based on histogram equalisation or the illumination-reflectance model. Histogram equalisation minimises variations in illumination by adjusting the global distribution of pixel intensities. This method is limited to local illumination [78]. In the illumination-reflectance model, with the assumption of a direct relationship between illumination and reflectance components, the illumination map is determined to output the reflectance map. Glaister et al. [79] stated that these applications are typically limited and have issues when applied to skin lesion images.

Among the existing studies on the pre-processing of PSLs, there are three pub-

lications in which illumination correction is specifically proposed for clinical and dermoscopy images [79–81]. These algorithms involve the estimation of initial and final illumination; the significant difference between them is the initial illumination estimation. A method proposed by Cavalcanti et al. [80] uses morphological filters to determine an illumination map. This work was improved by Glaister et al. [79], who proposed a multi-stage illumination modelling of dermatological images for illumination correction. The proposed method first estimates a non-parametric model of illumination using Monte Carlo sampling, followed by final illumination estimation which is based on quadratic surface modelling. This method outperforms the method introduced. However, this technique is criticized in a comparison study; Zhao et al. proposed an illumination modelling and chromophore identification method which is compared with the two previously mentioned techniques. More information about the performance analysis of these three approach methods is discussed in [81]. In these studies, there is no indication that these computationally expensive methods are able to detect the variations in illumination first and then decide to correct them.

2.5.2 Lesion Border Detection

Much of the current literature on melanoma CAD systems pays particular attention to developing border segmentation techniques. Border detection is an important component in CAD systems and plays a critical role in melanoma detection accuracy. Morphological structure of skin lesions may often result in difficulties with lesion border detection. A broad range of lesion segmentation algorithms have been developed to address these difficulties. However, these algorithms are designed based on particular imaging modalities (e.g. clinical and dermoscopy images) due to variations in the appearance of PSLs, and their performance is subject to variations in factors such as lesion type, colour, and light condition or angle of view [8]. Various techniques for border detection (also known as lesion segmentation) of clinical images have been proposed. Celebi et al. [82] categorised the segmentation algorithms used in border detection in clinical and dermoscopy images as follows:

- **Histogram thresholding methods:** The region of interest (ROI) is separated from the background by exploiting one or more estimated threshold values.
- **Colour-clustering methods:** Using unsupervised clustering and colour intensities, pixels are classified into homogeneous subdivisions.
- **Edge-based methods:** By applying edge detection algorithms such as Sobel

kernel, the edges between the lesion and the background can be used for border detection.

- **Region-based methods:** Classify the pixels into smaller parts by deploying region-merging/splitting algorithms.
- **Morphological methods:** Watershed transform is considered an example in this group, which can be used in contour detection algorithms.
- **Model-based methods:** These methods model the image as random fields and deploy optimisation solvers to estimate the optimal parameters of the model.
- **Active-contour methods:** Using these techniques the contour of the lesion is determined in order to separate the ROI from the background.
- **Soft-computing methods:** In this category, a classification algorithm such as a neural network or fuzzy logic is applied to classify pixel values into separable regions.

Lesion order detection methods (for clinical images) can also be categorised into simpler groups such as:

- Histogram thresholding [83–87];
- Discontinuity-based (detecting lesion edges using active contours, radial search techniques and Laplacian of Gaussian (LoG): active contour [88, 89], radial search [90, 91] and edge detection [92–94];
- Based on colour features [95–97];
- Based on Texture features [98–101];
- Based on combination of colour and Texture features [102];
- Region-based: watershed [84] and statistical region merging (SRM) [79, 103].

In a comparison study conducted by Hance et al. [104], six colour segmentation methods were assessed including fuzzy c-mean adaptive thresholding, spherical-coordinate transform/center split, principal-component transform/median cut, split and merge, and multi-resolution techniques for border detection of clinical images. The common idea behind these methods is based on setting the number of colours within the images to three (four for spherical-transform). The result of this study illustrated that adaptive thresholding and principal-component transform/median

cut performed with a lower average error than other reported methods. In addition, the authors proposed a method which improved this accuracy using a combination of these six approaches. In a recent article [98], Glaister et al. proposed a novel texture-based segmentation method, using joint statistical texture distinctiveness, and compared their result with three other state-of-the-art segmentation algorithms. Their result showed that their algorithm was more accurate than other reported techniques.

Pirnog et al. [86] proposed a simple automatic segmentation method for skin lesion identification for macroscopic images. They used only the saturation channel of the HSV (Hue-Saturation-Value) image. They claimed that using this channel component, two unwanted skin lesion components (hair and illumination variation) were addressed. They also compared their algorithm with the well-known grey-level Otsu's thresholding [105] as well as an active contour (Chan-Vese [106]) method, using 40 clinical images containing 30 benign and 10 malignant images; the 30 benign images were captured using a smart-phone camera. The accuracy of the proposed method was 98.49% against 79.81% and 65.53% for the Chan-Vese and Grey-level Otsu respectively, using the Dice similarity performance index.

In another comparison of segmentation by Maglogiannis et al. [85], global thresholding was proposed, which outperformed region growing and window thresholding techniques. Gradient Vector Flow Snake was proposed by Tang [89] to perform the segmentation. Cavalcanti et al. [107] proposed using Independent Component Analysis (ICA) to perform the initial skin lesion segmentation and the Chan method for the final segmentation. Cavalcanti and Scharcanski [108] deployed Otsu's Thresholding. The preprocessing step is applied to maximise the discrimination between healthy and unhealthy skin areas on the image. Kmeans clustering algorithm [109] is applied to project the pixels into two groups (patches); this increased segmentation accuracy compared with other algorithms mentioned. In a recent paper, Flores and Scharcanski [110] proposed a novel method for border detection of melanocytic skin lesions. After performing the pre-processing shading correction algorithm proposed in [80], the image is converted to a 3-channel image for better discrimination between the normal background and the lesion area. Then the converted image is divided into a set of image patches. They created an image patch dictionary using the Information-theoretic Dictionary Learning method to smooth the discrimination of these image patches. At the final stage, using Normalised Graph-Cut, the set of image patches is projected into two groups to create a binary mask. The binary mask labels the pixels as skin or lesion regions. They also evaluated their algorithm using 152 clinical images collected from the Dermnet (online resource) [17] and compared it with other previous segmentation methods which is briefly provided in Table 2.4:

Table 2.4: Comparison of the previous lesion segmentation algorithms with their performance (with two significant figures) accuracy used in [80].

Method	Performance
Tang's Snake [89]	59%
Otsu's Thresholding on the Gray-scale channel [111]	42%
Otsu Thresholding on the R channel [87]	38%
Thresholding on Multichannel Image [108]	34%
ICA-Based Active-Contours [107]	28%
NMF Segmentation [109]	25%
Scharcanski's method [110]	21%

One significant theoretical issue that has dominated the field is the lack of a proper definition of the ground truth (GT) for lesion boundaries [112, 113]. Generally, GT must be assessed and determined manually by an expert; however, significant disagreement is reported due to the various subjective criteria in specifying the boundary of lesion in dermoscopy images [112, 113]. Based on our knowledge, to date, there is no available public dataset including a standard GT definition for clinical images. A GT definition could allow researchers to evaluate the performance of their algorithms, achieve the desired results and make considerable progress in this context.

A limitation for assessing lesion border detection algorithms is that there are not enough comparative study for performance comparison of these techniques (based on clinical images). Comparison of these techniques is not easy because the researches investigated their algorithms by a limited number of clinical images, not a dataset including challenging cases. Moreover, the performance of these algorithms can be highly conditional and variable if an efficient preprocessing algorithm applies before this stage.

2.5.3 Feature Extraction

In the field of melanoma detection using CAD systems, feature extraction is the process of applying mathematical operations to measure particular properties from the output image of the lesion segmentation step. As mentioned in Chapter 1, the aim of feature extraction is to reduce the original image information by estimating particular attributes, differentiating between one object pattern and another in the picture. Therefore, it is crucial to determine the most powerful and effective features to be extracted from melanoma and other lesions images that will be used for the next step, which is diagnosis by a classifier.

It is worth mentioning that in the majority of melanoma CAD systems, the feature extraction algorithms are inspired by the clinical ABCD rule of dermatology due to its simplicity and effectiveness of implementation [114]. Feature extraction algorithms deployed in this field can be categorised into three main groups: a) shape-based (geometrical features); b) colour-based; and c) texture-based.

Tasoulis et al. [115] used these three types of features followed by feature selection. They used border features to cover the A and B parts of the ABCD-rule, colour features for the C rule and textures features for the D rule. Although D corresponds to a diameter greater than 7 mm in clinical images they used this term to extract differential structures of the lesion. Korotkov and Garcia [8] summarized feature descriptors used in melanoma CAD systems and noted that the feature descriptors used in dermoscopy images are completely different from those used for clinical images (using a standard camera) in terms of definition and meaning. Therefore, in this study we review and address the feature descriptors used for melanoma detection based on clinical images.

Shape features:

- **Asymmetry:** Several algorithms have been proposed for the asymmetry analysis of clinical images. To measure the asymmetry of a shape, image processing operations apply the binary mask obtained from the segmented lesion. The asymmetry descriptors used in the literature are based on
  - Centroid of lesion and moments of inertia e.g. asymmetry index;
  - Symmetry Distance.
- **Geometrical features:** The geometrical features are mainly area, major and minor diameter, perimeter, circularity, and standard deviation [115, 116].
- **Lesion's Boundary analysis :** A number of techniques were used to extract the border irregularity criteria of the lesions such as convex hull [12]; bounding box [117]; fractional geometry [116]; centroid distance diagram [118] and polygon approximation methods [119].

Colour Features: Colour features or histogram features include statistical parameters measured from different colour channels such as conventional Red, Green and Blue (RGB) channels [115, 116]. The following provides some information about colour features used for clinical image analysis:

- **Statistical features based on RGB images:** The descriptors in this class include measuring a number of statistical parameters from every channel of an RGB image, including min, max, average, standard deviation, skewness, Kurtosis, and entropy.

- **Statistical features based on colour space conversion of RGB images:** These features can be obtained by measuring the above-mentioned statistical parameters using the converted version of the RGB image in other colour domains such as: HSV (Hue, Saturation and Value), HSI, CIELUV, CMYK, Lab, Normalized-RGB and others.

- **Colour quantization:** Colour quantization is a procedure of reducing the number of similar colours existing in an image, so that the reproduced image is as visually similar to the original as possible. The features used in this class are based on relative colours used in the image and include, for example, statistics of relative difference and the aspect ratios of distinct colour channels in the RGB domain [120].

Texture Features: For texture feature extraction, the use of GLCM-based texture features (grey-level co-occurrence matrices) such as energy, entropy, mean, angular second moment, maximum probability, contrast and correlation have been reported [121, 122].

Calvacandi and Scharcanski compared five state-of-the-art texture descriptors applied to clinical images (107 melanoma and 45 atypical nevi) [123]. In this study, they investigated five texture descriptors including a) co-occurrence matrices, b) intensity variability, c) local binary patterns (acLBP), d) independent component analysis (ICA), e) and fractal measurement. They compared these features using two classifiers: SVM and KNN. The result was as follows:

- Co-occurrence matrices ranked the best option by:
  - classifier= KNN, accuracy= 84.21%,
  - classifier =SVM, accuracy= 79.60%.
- The fractal ranked the second by:
  - classifier =KNN, accuracy= 75.65% and
  - classifier =SVM, accuracy= 78.28%.

Amelard et al. [77], presented a framework for melanoma detection using clinical images, which consisted of pre-processing (illumination correction presented in [79]),

feature extraction and a simple classification algorithm (soft-margin SVM model). They applied the pre-processing step to correct illumination variation on the images because they believed that shadows can affect the lesion colours and thereby result in poor colour feature extraction. For feature extraction, a combination of high-level intuitive features (HLIF) that characterize asymmetry and border irregularity were extracted and combined with low-level features described in [80].

In this study we use shape, colour and texture features followed by feature selection, which is described in more detail in Chapter 5.

2.5.4 Classification

Classification is the final step in computerized melanoma detection. Various methods have been applied for melanoma detection, including artificial neural networks (ANN), Multi-layer Perceptron (MLP), Support vector machines (SVM), K-Nearest Neighbour (KNN) [121], as well as ensembles such as Bagging, AdaBoost (boosting), Rotation Forest, and Dagging. The accuracy of classification is highly related to the feature data collected from the previous step, as well as the type of classifier chosen."The comparison of classification approaches gives optimal results when performed on the same dataset and using the same set of descriptor" [8].

The number of prediction exemplars in a classification algorithm is related to the number of classes used for the training phase. For example, if the lesion types in the training phase are "benign" and "melanoma", the output of classifiers is binary; it is ternary when we have three types of lesion such as "benign", "melanoma" and "dysplastic".

Masoud and Al-Jumaily described classification algorithms that have been used in melanoma detection, with relevant references [124]. However, a comparative study including algorithmic calculations for feature extraction and classification was not provided. A comparison of classification methods was reported by Maglogiannis et al. [121]; the authors compared eleven classifiers (such as Bayes Networks, NBL, MLP, RBF network, classification via regression, CART, NBTree) using 3639 dermoscopic images and reported that their SVM out-performed other methods. They showed that feature selection and the learning process play significant roles in determining the accuracy of the system. As mentioned in the previous subsection, in [123], two classifiers (KNN and SVM) were compared using five different sets of texture features. The results showed that KNN performed with a higher overall accuracy, using the same dataset.

In many research studies published in the field of melanoma detection, the SVM

classifier has been one of the most widely used [76, 77, 114, 123, 125–127]. There is no evidence to date suggesting possible ways to increase the reliability of these biomedical diagnosis systems. High sensitivity is more important than high specificity in melanoma diagnosis systems. Although precise detection of all melanoma samples is crucial, a high false positive rate is not suggested.

Faal et al. [128] proposed using combination of three different classifiers (KNN, SVM and LDA) with the deployment of a different feature set for each classifier (trinary classification of benign, dysplastic and melanoma lesions), which helped to increase diagnostic accuracy for dysplastic and melanoma lesions.

In order to evaluate the performance of the state-of-the-art classifiers based on the feature data extracted from the clinical image dataset, we compared the accuracy of nine classifiers. We also address improvement in accuracy of the system as described in Section 6.2.3.

2.6 Deployment of Deep Neural Networks (DNN) in Machine Vision and Medical Imaging

Recently, deep learning has been the subject of renewed interest in machine learning due to very encouraging results in speech recognition and computer vision. Deep learning is a set of algorithms including Neural Network (NN) as an architecture [129, 130]. "A standard neural network (NN) is consisted of many simple connected processors called neurons, which produce a sequence of activation functions" [131]. Although the field of artificial neural networks (ANN) dates back to the 1950s [132], nowadays they are more popular with taking advantage of parallel hardware processors such as GPUs and FPGAs. It has been reported that a shallow network obtained the same level of accuracy as a deep network with many more connections in a speech recognition application [133, 134]. Figure 2.6 shows the difference between a shallow and a deep network. It can be seen that in the deep network, the activation function obtained by the red neuron in the layer one is reused three times in the computation of the output function; in the shallow network, the function computed by the red neuron is only used once [131]. Therefore, a shallow network is more computationally expensive when the problem has non-linear properties.

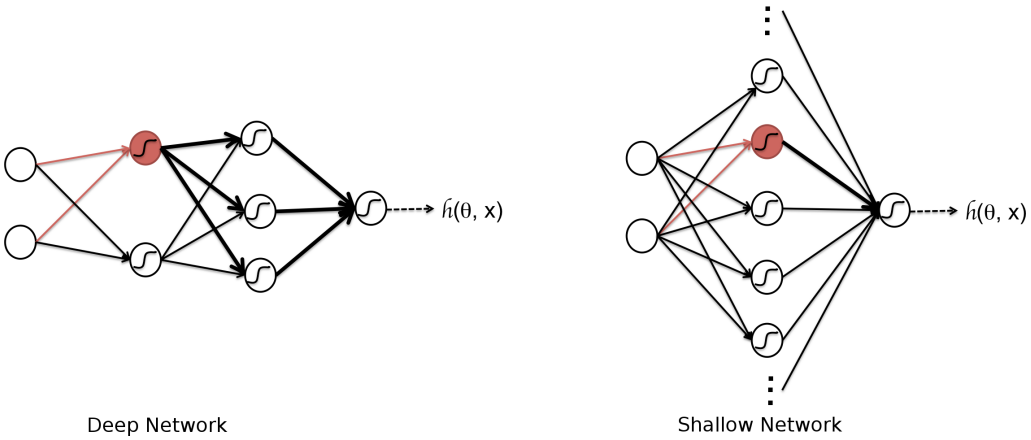

Figure 2.6: Deep network vs. shallow network [131].

In machine vision, most deep network architectures are composed of multiple layers followed by a classical classifier such as Multilayer Perceptron (MLP classifier), where each layer is composed of linear two-dimensional filters, non-linearity functions and pooling of data (also known as sub-sampling) [129, 135]. Most recent machine vision research has focused on the task of training such deep networks using large available datasets in the form of image frames. These deep networks need to learn good feature representations for complex visual applications such as object recognition and tracking [136]. These feature representations usually involve learning the linear shared weight values (also known as shared filters) from labelled (supervised learning) or unlabelled (unsupervised learning) input data.

Deep convolutional neural networks have obtained good outcome in a broad range of computer vision problems, including image classification [137–140], object detection [141] and semantic segmentation [142–145]. Couprie et al. presented a multi-class segmentation algorithm for indoor scenes based on supervised learning and RGB-D input images [142]. They applied multi-scale convolutional neural networks (CNN) to learn features directly from the images and the depth information (D channel). Their proposed architecture achieved an accuracy of 64.5% based on an NYU-v2 depth image dataset. Lenz et al. [145] later proposed an adapted version of this architecture for a robot vision application using RGB-D images and found that using a deep network had several benefits: a) it avoided hand-engineered features, but learned them directly instead, b) it outperformed even well-designed features from previous studies.

Since providing labelled data (supervised learning) to the network is expensive and often comes with human errors [136, 146], unsupervised learning can help the network to learn features purely from unlabelled input data [149, 150]. These methods can learn multiple layers of deep networks through training several layers of features, one layer at a time [147, 148]. Recent approaches based on unsupervised

clustering techniques were promising because they used simple learning methods such as K-means clustering [148]. Culurciell and Bates [136] adapted this method to promote it for general-purpose real time robotic vision system.

While CNNs have also been applied to segmentation and object recognition problems, most of the previous work reported on non-medical problems, along with many proposed architectures, is not well suited to medical imaging systems. Based on our knowledge, to date, DNNs have not been applied in the field of melanoma segmentation and classification. However, there have been reports on other medical applications. Havaei et al. [149] proposed a fully automatic brain tumour segmentation approach based on DNNs using MR images. Their specific architecture uses both local features and more global contextual features simultaneously, since the tumours can be anywhere in the brain with any kind of shape, size and contrast. They also deployed a cascade classifier in which the output of the CNN is used as the input for another CNN. Petersen et al. [150] used an unsupervised DNN for breast tissue segmentation and mammographic risk scoring and reported that the learned percentage mammographic density (PMD) scores were well correlated with manual scores and were more related to future cancer risk than manual PMD scores.

2.7 Summary

This chapter has provided an overview of current clinical methods used for melanoma detection. In addition, it also highlighted the significance of image processing in the evolving domain of computerised diagnosis of melanoma applications. Basically, there are four stages in a CAD system for melanoma detection: pre-processing, lesion segmentation, feature extraction and classification. Recent works that applied these methods were reviewed in this chapter. Furthermore, we reviewed recent works that used deep neural networks based on general-purpose machine vision applications. The next chapter presents a comprehensive study to select a proper platform for the implementation of image processing algorithms to create a hand-held medical imaging tool.

Chapter 3

Embedded System for Medical Imaging

3.1 Introduction

In recent years, real-time vision systems have been used in a wide range of applications and sophisticated medical imaging systems. Most computer-vision applications have been developed based on a Graphics Processing Unit (GPU). However, recent developments in the field of powerful, low cost and energy-efficient embedded systems have led to the implementation of image/video applications in Digital Signal Processors (DSPs) and Field Programmable Gate Arrays (FPGAs). Each technique has its advantages and tradeoffs based on the nature of the algorithms, performance requirements, power consumption, cost, productivity, flexibility and design cycle time. With the development of advanced algorithms, especially in the medical imaging realm where the majority are computationally intensive, more flexibility and performance are required to achieve adequate performance in embedded systems at an affordable cost and with acceptable power consumption.

Among the various types of programmable and reconfigurable platforms that can handle image and video processing tasks, FPGAs and DSPs are the most popular devices for embedded systems and System-on-Chips (SoCs) due to their lower power consumption and portability compared to other platforms such as GPUs. The main limitation of DSPs, however, is their limited resources in terms of memory bandwidth and arithmetic logic units (ALU). Therefore, they cannot adequately perform some parallel processing techniques such as 3D medical imaging. In contrast, FPGAs can be considered a promising technology with good performance and flexibility via their massive hardware-based parallel signal processing capabilities that enable computation of sophisticated algorithms such as real-time medical imaging [151]. Typically,

due to the complexity of the hardware specifications, implementation of sophisticated algorithms and systems becomes more complicated. A serious weakness with FPGAs is that implementing a DSP algorithm using a register transfer level (RTL) in hardware description language (HDL) is very time consuming [152, 153]. For instance, to implement an image processing algorithm on FPGA or DSP an engineer writes the code in C/MATLAB and verifies it with a simulator. Then, the hardware engineer has to convert the code to a verified synthesizable HDL code for mapping on an FPGA or DSP device.

This chapter comprises two parts: the first deals with hardware and software implementation of image processing algorithms using the state-of-the-art embedded system technology. The second investigates an efficient imaging system in the context of medical imaging. One of the recent products from XILINX, ZYNQ-7000, is a possible solution to the challenges of hardware and software implementation of a vision system on a single System-on-Chip (SoC) device. It may also decrease the unit cost and increase accuracy as well as performance, thereby optimizing the processing task. The ZYNQ-7000 platform was found to be suitable for designing the proposed hand-held medical imaging system for early diagnosis of skin cancer.

3.2 Embedded Platforms for Implementation of Image Processing Applications

Processing of complex applications in medical imaging are computationally expensive, power consuming and may require a high memory bandwidth [154]. In this section, some alternative embedded hardware targets for implementation of computationally expensive image processing algorithms are discussed to determine the advantages and tradeoffs of different types of platforms in the realm of embedded systems.

Typically, embedded vision platforms can be categorized into the following groups:

- Software-based on DSPs.
- Customized hardware module in high-performance FPGAs.
- Customized hardware module plus single embedded soft-core microprocessor in FPGAs (HW/SW co-design).
- Combination of a DSP and FPGA (Hybrid).
- Combination of a GPU and a general purpose processor GPP.

FPGAs and DSPs are the most popular platforms for embedded systems and SoCs due to their lower power consumption compared with other platforms such as GPUs [155]. GPPs and DSPs suffer from limited memory bandwidth and few arithmetic logic units (ALU), so that some parallel techniques such as 3D medical imaging algorithms cannot be fully performed; in contrast, FPGAs provide high performance and flexibility for sophisticated algorithms [156].

Digital signal processors from Texas Instruments (TI) have been widely used for the implementation of a wide range of application signals and image processing. However, there are some key issues for implementation on single embedded cores such TMS320DSP6416 and TM320DSPC6713. These issues can be power consumption, heat dissipation, number of instructions that can run in parallel, and other bottlenecks [157]. To overcome these problems, multi-core technologies are generated for multimedia applications. Typically, TI's multi-core platforms are a combination of technologies such as GPPs, DSPs or SoCs and they can be divided into homogeneous and heterogeneous architectures [157]:

- Homogeneous architectures consist of multiple DSPs with identical architecture. For example TMS320C647x consists of six C64x processors which can work together in parallel.

- Heterogeneous architecture involves a combination of a DSP and a GPP (i.e. ARM processor), a GPU(s) or Micro Controller Unit(s) (MCUs).

There have been numerous published studies on the topic of implementation of image processing and its applications based on the OMAP3530 architecture from Texas Instruments. These studies show that OMAP has been a popular platform for image processing applications. In [158], OMAP was used for implementation of wave form techniques. The performance of this platform was measured based on four different system design methods for the use of the ARM processor and the corresponding DSP processor. According to this article an embedded system on OMAP DSP processors can be implemented as follows:

1. Only on Cortex-A8 (ARM processor)
2. Cortex-A8 + NEON implementation
3. Only on DSP
4. Dual-core (Cortex-A8 and DSP)

It was found that the second method (ARM cortex-A8 + NEON engine) gave the best performance where the NEON engine was used as a co-processor to support floating point numbers. However, the negative aspect is that DSP was of no use in this method. The final method (combination of ARM and DSP) was faster than the third method (DSP only). The key issue with this platform is that floating-point numbers are not supported by the fixed-point C64x DSP and much time is consumed in software emulation of floating points [159]. Although OMAP3530 is considered a promising platform for implementation of vision systems, with the ability to run a real-time application, in most studies to date the implemented applications cannot be considered as sophisticated and computationally intensive algorithms.

Another powerful multi-core DSP platform that has been used is TI-C6472 [160]. The chip consists of six high-performance C64x core + DSP at an overall speed of 4.2 GHz with a performance similar to a typical GPU. The performance of the system was compared with a simple CPU; the multi-core operated ten times faster. In addition, TMS320C6455 has been used for image processing with a maximum frequency of 1 GHz, which is slower than a typical GPU. For example, an algorithm proposed for performing computed tomography images in the field of medical imaging on a C6455 DSP processor executed in 336.0s and 8.9s on a DSP and GPU, respectively.

3.3 FPGAs

FPGAs are becoming much more powerful platforms via which to improve processing capabilities and this has led to a renewed interest in the implementation of embedded vision applications. Several studies have shown that FPGAs can achieve 100 times higher performance compared with traditional DSP processors in a number of signal-processing applications [161]. In such systems, not only is hardware logic used, but also the embedded soft CPU-Core can be involved in the computation to improve productivity and system performance. A considerable amount of recent research has involved computationally intensive applications such as medical imaging and real time image processing based on XILINX FPGAs, especially Virtex5 and Virtex-6 [162–167].

One of the most significant issues with FPGAs is that system design, debugging and verification are more complex, time consuming and error-prone than other platforms (DSPs and GPUs) [168]. Therefore, FPGA implementation requires hardware design experience using HDL codes (Verilog,VHDL). Ahmed et al. [169] reported that the Dynamic Partial Re-configuration (DPR) technique can be used as a powerful solution for implementation of computationally intensive applications e.g. 3D medical image processing. They proposed an efficient architecture for 3D HAAR Wavelet Transform (HWT) using DPR on virtex-5 XILINX FPGA with standard quality and reconstruction of medical images such MRIs and CTs. Using DPR, several large systems can be mapped into a single FPGA.

3.3.1 Hybrid Architectures using FPGAs

Many published studies describe vision systems based on hybrid architectures of DSPs and FPGAs. Typically, within these architectures, a multi-board (DSP-FPGA) is parallelized to accelerate the high-demand computational tasks for image and video processing. In this kind of system, FPGAs are involved with accelerating the speed of processing of complex computational tasks. In [160], TMS320C6455 (DSP) was used for channel coding algorithms in order to achieve real-time processing and Virtex-5 was used to support recognition of I/Os. TI's DaVinci DSP platform has been also used widely as a coprocessor with an FPGA. Yan et al. [169] developed a multiple object tracker for indoor environments using a DSP-FPGA based system in which ALTERA Cyclone2 is involved with a CMOS camera and a TMS320DSM64 processor (DaVinci) is used for video processing. Another DSP-FPGA-based technique evaluated for medical imaging is also presented [170]. The proposed system consisted of a XILINX (Virtex-4) and DaVinci (TMS320DM6446) processor, which proved promising in terms of cost and real-time solutions. A dig-

ital scan solution (SDC) platform on TMS320c64x (DSP) was used as the heart of the system, the FPGA was used for the speckle-reduced imaging (SRI) module and the ARM processor of the DaVinci platform was used to focus on the diagnostic mode. Although the complexity of the algorithms was not high, the initial implementation was not satisfactory in real-time performance and several optimizations were needed. Fang et al. [171] designed a video-text extractor based on a DaVinci DM644 platform with the architecture distributed on a dual-core (ARM and DSP). Several threads were performed on the ARM side to capture, display and control devices. The main algorithm was implemented on the DSP side. Although the authors proposed a design flow for communication between cores, several optimizations were applied to enhance the processing speed performance. The key problem with these kinds of systems is that the designer evaluates the multi-board based on two different systems and each technique has its own challenges and design requirements.

Obviously, each technology has its pros and cons in terms of power consumption, cost, productivity, flexibility and design cycle time.

- In terms of power consumption and portability, DSPs and FPGAs are more suitable than GPUs.
- The development cost of DSPs is reasonable, and more straightforward when parallel processing is not essential.
- With regard to flexibility, FPGAs are more suitable, because of their parallel and reconfigurable architecture, than GPPs or DSPs due their limited memory bandwidth and ALUs.
- Although hardware implementation on FPGAs is more complex and tedious compared with DSPs and GPUs, new implementation methods such as model-based design can help to accelerate the design process and increase the productivity of FPGAs.

3.4 Recent Hardware Implementation Methodologies and Related Description Languages

There has been considerable research in the area of hardware implementation of image processing algorithms using FPGAs. Typically, due to the complexity of the hardware specification, implementation of these systems becomes more complicated. In general, DSP designers use different high-level languages such as C/C++, while FPGA designers deploy low-level Hardware Description Languages (HDL) such as

Verilog or VHDL. The following shows the typical procedure for implementation of a simple DSP algorithm onto FPGAs [172]:

- The DSP engineer has to first write the code in C/MATLAB and then verify it with simulation in the MATLAB environment.
- An experienced hardware engineer has to convert the code to a synthesizable HDL manually (using Verilog or VHDL) to create a hardware accelerator. The synthesized code is mapped onto an FPGA device for verification of the synthesized code by creating test benches.

New methodologies such as model-based design and High Level Synthesis (HLS) tools have now become available [173–175]. Model-based approaches have been widely used for implementation of DSP algorithms. Moreover, HLS languages and tools such as Impulse-C , Handel-C , Catapult-C and AutoESL are software-based tools created with the aim of solving the problem of HW/SW co-design and the limitation of using floating-point functions [176]. Figure 3.1 shows a number of design tools for implementing DSP algorithms on FPGAs.

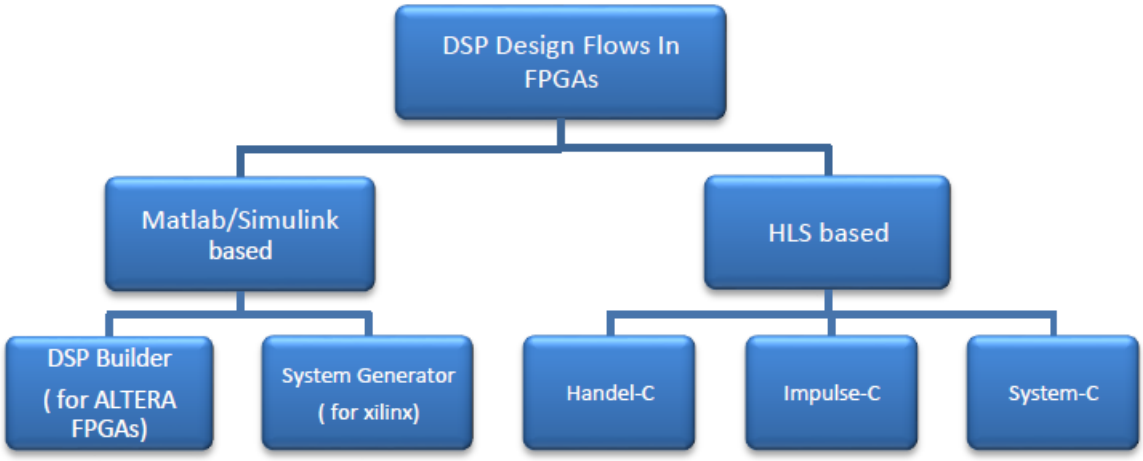

Figure 3.1: Design methods for implementation of DSP algorithms on FPGAs.

3.4.1 System Generator

The XILINX System Generator is regarded as a useful development tool for the implementation of signal processing algorithms [170]. This tool is a model-based software provided by XILINX Inc, which can be integrated with the Simulink of MATLAB and which helps HDL developers who are not expert in FPGA programming (Verilog/HDL codes). In [177], a standard resolution geospatial imagery system was developed on Virtex-4 XILINX FPGA and the performance of the system

is reported to be 11 times faster than a normal CPU on a PC. In another study [178], the System Generator was used to implement real-time parallel 2D (Magnetic resonance imaging) MRI image filtering based on Virtex-6 FPGA. However, the results and output resolution are not encouraging. In another major study, research on the feasibility of using System Generator for medical image processing proposed an efficient architecture for image filtering and tumor characterization, implemented on Spartan 3-E XILINX FPGA with promising results [179]. The VHDL codes were automatically generated via the System Generator from the Simulink of MATLAB to implement MRI brain images for tumour characterization. However, the results showed that further work is required to enable real-time image processing for the proposed architecture. Sami Hasan [180], presented a nine parallel 2-D MRI filtering algorithm in a single FPGA-based architecture using the XILINX System Generator and demonstrated fast filtering throughput performance, with minimum total power consumption (0.86 Watt) at a maximum sampling frequency (230 MHz).

3.4.2 High-Level Synthesize Language

With current developments in FPGA chip capabilities, it is possible to implement more sophisticated algorithms on FPGAs. However, algorithm implementation using register transfer level (RTL) for hardware description is time-consuming and error-prone. Although research on HLS methodologies has been undertaken since 1990, they have only recently become an attractive solution [181]. Generating HDL code using high level language may significantly increase design productivity and reduce development time, and pure HDL programming mistakes can be excluded [182–184]. Unlike the traditional design flow methodology, HLS can improve design quality and accelerate design and verification tasks by applying optimal synthesis directives to transform C/C++ code specifications to RTL implementation, which can be synthesized into FPGA devices [185]. The HLS workflow is significantly different from traditional design workflow. Xu et al. [152] developed a method for implementing computed tomography images that work well using Impulse-C. The ease of use and high performance of HLS (Impulse-C) compared to VHDL produced orders of magnitude of speed-up in a software implementation of a back projection application. Li et al. [166] developed a system design for 3D optical coherence tomography on Virtex-5 XILINX. The hardware implementation efforts were decreased using HLS; however, in comparison with GPUs, results indicated that a GPU can be better optimized and 15 times faster than an FPGA [153].

Handel-C is another C-like language HLS tool in which:

- The C-based algorithm can be translated into HDL

- Instruction codes can be executed in parallel (depends on code structure)
- Each instruction executes in one clock cycle
- Few interfaces/connections for hardware peripheral or VHDL/Verilog HDL module provided [156].

An architecture for multi-resolution analysis and efficient algorithm execution has been implemented on an RC1000 Celoxica development board using Handel-C [186]. A ray-casting algorithm for 3D volume rendering was proposed targeting Virtex-5 using Agility's Handel-C [156]. Volume rendering is a technique for displaying a 3D object on a 2D screen and ray-casting is an efficient memory cache technique which is used for the implementation of four rendering pipelines in a single FPGA. However, developing high quality volume rendering for images is extremely difficult, since the need to provide real-time feedback to the user involves processing large amounts of data at a visually acceptable frame rate, which imposes significant constraints on the memory and visualization system. In another study [187], an efficient architecture for online volume rendering for medical imaging was developed on a CELOXICA RC340 board (Virtex-4) using Handel-C. Appiah et al. [189] also performed real-time segmentation of moving objects in a video stream on an RC340 via Handel-C [188]. The methodology consisted of two algorithms for multi-modal background modeling and connected components analysis. Furthermore, the functional verification of this work was compared with MATLAB using the same algorithm and the same results. The results of these studies showed that a single FPGA can effectively be used for parallel and real-time image and video processing.

3.5 ZYNQ-7000 Extensible Processing Platform

In our study, we selected ZYNQ-7000 as a suitable processing platform for our hand-held application. The ZYNQ Extensible Processing Platform (EPP) can be configured to run computationally intensive tasks and an operating system such as Linux or Android on its ARM processor. The ZYNQ-7000 family is based on the XILINX programmable SoC architectures, built on a state-of-the-art, high performance, low-power, 28 nm technology which is a combination of ASIC and FPGA technologies. It consists of a dual-core ARM Cortex-A9 MPCore-based processing system (PS) and XILINX programmable logic (PL) all in a single SoC device. The ZYNQ SoC is a cost-effective platform as well as a high performance solution for designing a wide range of embedded applications such as portable medical systems. In this study, we use ZYNQ because of its flexibility, scalability, power and performance of ASIC technology. This section describes an overview of the ZYNQ-7000

architecture and proposed methods for design and implementation of the embedded vision system.

As shown in Figure 3.2, the ZYNQ-7000 EPP architecture contains the following main functional blocks:

- Processing System (PS)
- Programmable Logic (PL)

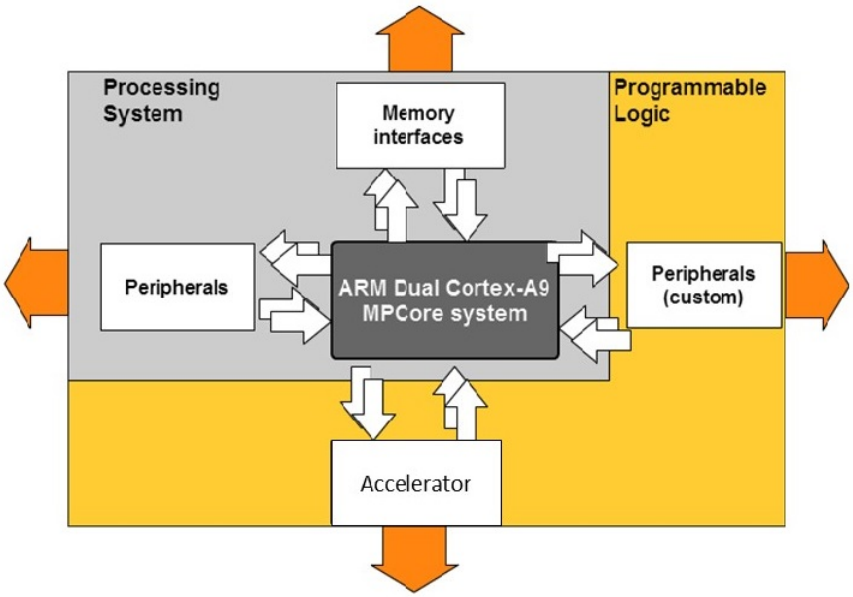

Figure 3.2: Block diagram of the ZYNQ-7000 platform [189].

3.5.1 The Processing System (PS)

The ZYNQ-7000 family takes advantage of a complete ARM-based processing system, which is a dual-ARM cortex in an Application Processor Unit (APU) integrated with the NEON media processor. Moreover, the PS of the ZYNQ supports hardware for memory interfaces and communications peripherals. This is a key point of the system architecture because the PS is always the master and operates independently, meaning that the PS can operate with or without configuring the Programmable Logic (PL). The most important features the PS supports are:

- Dynamic RAM interface (SD-RAM), supporting either DDR3 and DDR2 standards.
- Static RAM interfaces (SRAM devices such as NOR and QSPI flash memories).
- Communication interfaces such UART, SPI, I2C, USB, Gigabit Ethernet.

- General Purpose I/O up to four 32-bit.

3.5.2 The Programmable Logic (PL)

Currently, the ZYNQ SoC family is divided into four types: ZC7010, 20,30 and 40. Although the PS is identical in all types, the FPGAs (PL) are different. Artix-7 and Kintex-7 are the integrated FPGAs in the SoC. In this study, we selected the ZC702 series of ZYNQ, which is currently available and supported by XILINX Inc. The main features of the PL are [189]:

- Configurable logic blocks (CLB) which contain 6-input lookup tables (LUTs)
- Memory capability within the LUT and register and shift register functionalities
- Digital signal processing-DSP48E1 Slice contains 25×18 two's complement Multiplier/accumulator high-resolution (48 bit) signal processor
- Power saving 25-bit pre-adder to optimize symmetrical filter applications
- Many advanced features such as:
  - Optional pipelining,
  - Optional ALU
  - Dedicated buses for cascading and a 36 KB block RAM consisting of a vast amount of configurable I/Os as well as high-performance Select I/O technology.

3.5.3 Communication between the PS and PL

The close and comprehensive integration between the processing system (PS) and the programmable logic (PL) provides the flexibility of ASIC technology and the performance of FPGA technology on a single SoC. Depending on applications and their performance requirements, the PS and PL can communicate with each other using:

- Advanced extensible Interface (AXI) for master and slave interfacing for direct access to external memories (DDR3 or DDR2) and on-chip memory.
- Direct Memory Access (DMA) and interrupts (up to16 interrupts from the PL to the PS via four DMA channels).

- Up to four clocks and resets to the PL from the PS.
- Extended peripherals in the PL which increases the number of PS peripherals.

3.6 ZYNQ SoC Configuration

3.6.1 Hardware Configuration Steps

1. Creating a project using the PlanAhead tool which supports the ZVIC-board and ZYNQ SoC (the ZC702 ZVIC development board was selected for this research). This tool helps us to create an initial system automatically in a short time.

2. Adding or creating an embedded source using the XPS (XILINX Studio Platform) tool to declare PL and PS components (IPs). The XPS, as a part of the PlanAhead software, is used as a GUI interface to connect all essential components within the SoC. Figure 3.3 shows an overview of the XPS. The next section briefly describes the software tools for programming and integrating the PS/PL sides of the SoC.

3. After setting up the hardware using PlanAhead and XPS, the created hardware specification files, called the Base Support Package (BSP), can be exported to the SDK tool to create a software program and run it on the ARM processor. The BSP contains all components' drivers as well as their C-header files which provide a memory map of the system and other system peripheral parameters.

4. In the next step, one can choose C or C++ language to write the actual software program running on the ARM processor. The main program can be used either in bare-metal mode (without the operating system) or on the operating system mode (currently XILINX fully supports Linux OS on ARM PS).

5. In the next step, one can choose C or C++ language to write the actual software program running on the ARM processor. The main program can be utilized as either on bare-metal mode (without operating system) or on the operating system mode (currently XILINX fully supports Linux OS for running on ARM PS).

6. Once the software is successfully compiled and verified (an ELF file is the output file for this stage), the PS and PL are programmed respectively.

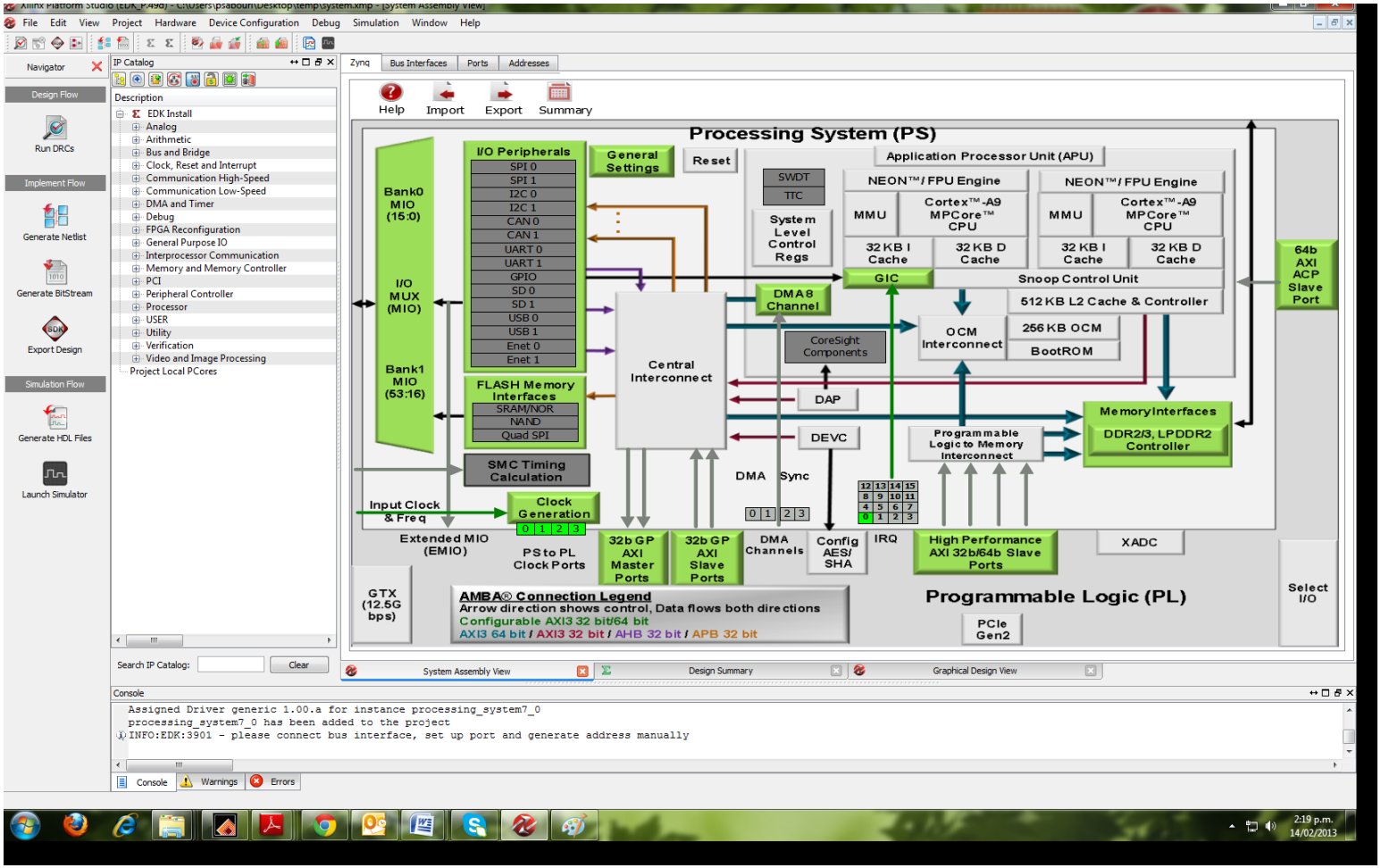

Figure 3.3: XPS software tool for hardware configuration.

3.6.2 Hardware and Software Partitioning on ZYNQ-7000

As discussed before, the processing side of the ZYNQ itself is a complete computing platform; however, the FPGA area, which is integrated to the PS, can be used as a powerful accelerator in order to increase the performance of the processing system. In the context of the ZYNQ, we propose a method in which the bottleneck in the system will migrate to the PL side to accelerate the speed of the processor. The migration is achieved by the high performance AXI4 interconnection port which tightly integrates the PS and PL. In this method, software can be developed for the processing system. If acceleration is needed (for computationally intensive applications such as image processing), the FPGA area is configured as one (or more) IP accelerator(s) of the system. Figure 3.4 shows our proposed design flow for the configuration of an efficient embedded vision system. The proposed design flow is divided into the following steps:

- Software development: Firstly, the software code is developed based on the ARM processor via the GCC compiler in the Software Development Kit (SDK) tool.
- Software profiling: We developed a program for a simple FIR filter and then realized that part of the system (for loops) was the bottleneck of the system; this part can be implemented on the PL side as an IP.
- Software and hardware partitioning: Once the bottleneck of the system is detected, it must be decided which functions of the system can be implemented on the hardware for acceleration. For example, the loops of the FIR filter can be implemented on the PL side as an IP. Another key aspect of the system partitioning is that it is possible to select suitable communication infrastructure such as DMA or memory mapping.
- Finally, after SW/HW partitioning, some changes in the main SW are required to call and run the HW accelerator IPs.

3.7 VIVADO HLS Tool

The VIVADO HLS tool is proposed to replace manual design flow with an automatic process. VIVADO HLS uses the main software to generate its related HW accelerator; however, several directions and restructuring must be applied directly and manually in order for the hardware conversion to improve the design quality,

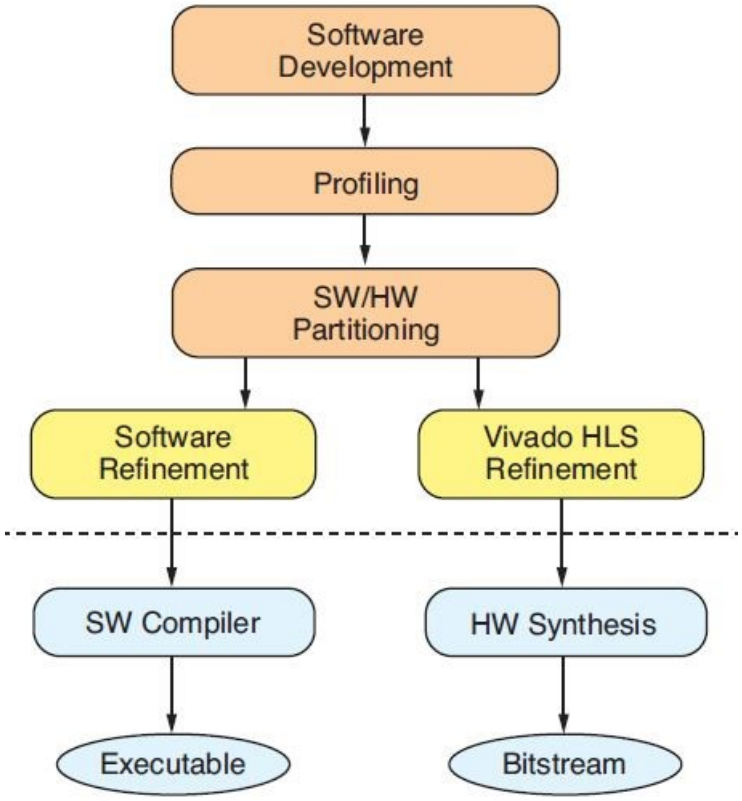

Figure 3.4: System design flow [189].

efficiency and performance requirements (here hardware conversion means the way that HLS is able to produce efficient and functionally-equivalent Verilog or VHDL code). In this research, we used the VIVADO HLS tool for HW implementation of image processing IPs for the following reasons:

- Only VIVADO HLS supports ZYNQ-7000 SoC and our ZVIK development board while other tools such as Impulse-C do not.
- There are several pre-defined IPs in the XILINX IP catalogue which can be employed to develop our system more rapidly than traditional design flows and other HLS tools. Different interfaces and DSP building blocks are some of these predefined IPs. The C header files and drivers needed for software programming and controlling can be created automatically.
- Using VIVADO HLS we are able to create test benches in C or C++ in executable software. This feature is one of the best options for implementation and verification of the image processing algorithms so that we can test the developed code rapidly before synthesizing and downloading it to the FPGA. It should be emphasized that this opportunity is not available with the traditional HDL (Verilog or VHDL) design flows. This is an important point that simplifies the design procedure significantly.

- Compared to a DSP C flow (comparison of Spartan3-A versus TI's DaVinci Processor), the VIVADO HLS solution is:
  - suitable for Full-HD performance (40 times higher than TI's DaVinci Processor);
  - more affordable in cost (28 ×higher performance);
  - requires fewer code modifications.

Figure 3.5 shows the proposed method for hardware implementation using VIVADO HLS.

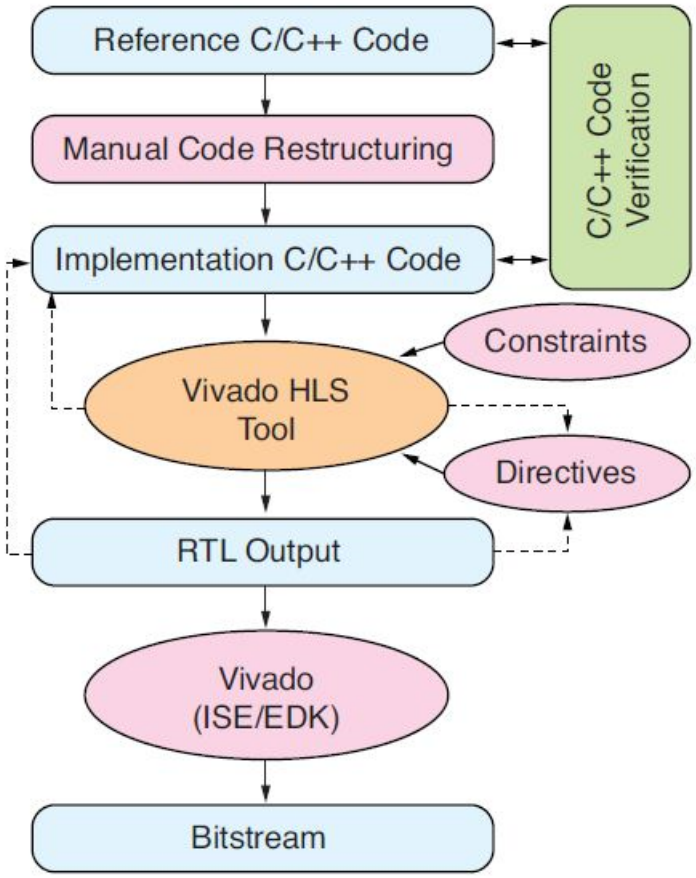

Figure 3.5: HLS design flow for programmable logic [189].

In the first step we needed to use C/C++ reference design code as a model. OpenCV is a powerful and efficient open source tool for machine vision and image processing. In this research, we employed some C/C++ reference design from OpenCV libraries to implement the design in FPGA with some changes in the original codes. The modification means reprogramming parts of the code to illustrate the hardware specification, architecture and DSP macros. The functional verification of

the implemented code uses traditional C/C++ compilers (GCC compiler) and using C/C++ level testbenches developed for the verification of the reference code.

For efficient implementation of the code with RTL, several constraints, compiler directives were inserted into the code as follows:

- Function Optimization
- Loop optimization (unrolling or pipelining, etc)
- Array and memory optimization (resources, map, partition, reshape, stream, RAM and buffers)
- Logic structure optimization
- Interface management

The HLS tool takes all these inputs (the implementation C/C++ code, constraints and directives) to generate an optimized RTL output and reports the throughput and performance of the generated architecture. If the generated architecture does not meet the required throughput, we can alter the C/C++ code or the directives. The HLS tool is able to provide a report of final achievable clock frequency and number of FPGA resources used only after running logic synthesis and place-and-route. If the design does not meet timing performance requirements or the FPGA resources are not satisfactory, further modification is needed for the implementation C/C++ code or the compiler directives. One of the key points of HLS tool is that it is an iterative design flow; the implemented code can be evaluated in different types of restructuring until the required performance is achieved. Furthermore, the C verification code (testbench) can be reused to verify changes to the implementation code. When the architecture achieves the required throughput and performance, then we can use the RTL output as the input to the XILINX ISE/EDK tools for the next level, which is integration of the system design. The output package can be used either as a PCORE (IP) in the IP catalogue of XILINX studio platform (XPS) or as a DSP BlockSet for the system generator tool in SIMULINK of MATLAB. This can help to ease access to the hardware implementation.

3.7.1 XILINX ZVIK Tool

A portable and efficient melanoma CAD system is a computationally intensive application and requires a sophisticated platform to run. In this project a XILINX ZVIK development board (ZYNQ-7000 Video and Imaging Kit) was used for the implementation and evaluation of some proposed algorithms in this study. The ZVIC

consists of a development board based on a ZYNQ-7000 SoC as the heart of the system and a Full HD (1980 × 1080 resolution) image sensor.

3.8 Summary

This section presented the alternatives for development of an advanced embedded vision system for medical imaging. High speed image and video processing is becoming increasingly important in medical imaging. Advances in embedded systems and their applications in the medical imaging field are growing fast. However, the limitation of system development on a single platform such as a DSP or FPGA is a major concern in designing complex systems. Moreover, each platform has its advantages and trade-offs based on the nature of the algorithm, performance requirements, power consumption, cost, productivity, flexibility and design cycle time. One of the recent products from Xilinx, ZYNQ-7000, can be considered a promising way to overcome these challenges. The ZYNQ-7000 consists of a dual-core ARM processor which is surrounded by 7-series Xilinx FPGA based on 28 nm technology. The close integration between processing system and programmable logic combines the flexibility of ASIC technology and the performance of FPGA technology on a single SoC. The state-of-the-art ZYNQ-7000 SoC may be a suitable solution for designing hand-held medical imaging systems for skin cancer detection.

Chapter 4

Border Detection

4.1 Introduction

Border detection (lesion segmentation) is one of the crucial components of a melanoma detection system. Development of and effective and accurate lesion segmentation algorithm is very important to separate the lesion (mole) from the healthy part of the skin. The result of this step could impact the rest of processing (feature extraction and classification). However, implementation of an accurate lesion segmentation algorithm is challenging due to various conditions such as human skin colour variations, hairy skins, light illumination, uncontrolled image acquisition such as light illumination and etc. A number of border detection algorithms for segmentation of PSLs, based either on dermoscopy or clinical images have been developed, as discussed in Chapter 2.5.2. In this chapter, three different approaches for border detection of skin lesions are presented: a) using edge detection; b) using colour features; and c) using Convolutional Neural Networks. In the first section, we evaluate several edge detection methods. In addition, a framework for the development and implementation of a border detection technique as applied to a melanoma CAD system on an embedded system is discussed. Then, we propose a colour-feature-based method for border detection in order to improve the accuracy of the border detection. Finally, a novel lesion segmentation method using a Convolutional Neural Network, which addresses illumination correction and hair removal in the processing step is discussed.

4.2 Border Detection Using Edge Detection

This section presents a basic border detection system developed and implemented on a ZYNQ-7000 SoC, using the VIVADO High Level Synthesis (HLS) tool. We take advantage of accelerating an embedded system design on a single SoC, which offers the required features for real-time processing of skin cancer images. Several edge detection approaches (more information about these techniques can be found in [113]) have been investigated and implemented on ZYNQ-7000 for border detection of skin lesions, which can be used in the early diagnosis of melanoma. The results show better performance than other reported methods. Performance evaluation of this approach has shown a good processing time of 60 (frame per second) fps for real-time applications.

4.2.1 Methodology

Figure 4.1 presents the flowchart of the algorithm used for border detection. First, the RGB-colour image is converted to a Hue-Saturation-Value (HSV) colour space. We analysed two colour spaces such as HSV, and RGB in order to find the optimal colour channel (Table 4.1 provides more information about this analysis). The Value channel (V) of the HSV colour domain was the optimal channel for this application. A median filter is applied in order to enhance the accuracy of lesion segmentation. This is helpful to smooth existing noise and unwanted artefacts within the image. The pre-processing step is done using morphological filters such as erosion and dilation over the image to remove hairs and other artefacts such as ruler markers. Then, edge detection is applied to detect the outline of the skin lesion following histogram thresholding. However, it was observed that the images used in our experiment did not include many hair artefacts. Edge detection algorithms are used in image analysis with the aim of detecting boundaries between objects and the background in grey level images. Although there are many approaches to edge detection and object recognition in medical imaging, the calculation of the gradient level value for each pixel using a matrix of neighbouring masks and comparison of this value with a given threshold is a common approach. If the calculated value is greater than the threshold, the pixel is grey as an edge.

Edge detection is the a set of mathematical operations that is widely used in image processing with the aim of detecting points in an image where the brightness changes. Although there are many approaches for edge detection in image processing and machine vision realm, the calculation of the gradient level value for each pixel using a matrix of neighbouring masks and comparing this value with a given threshold, is a common approach. If the calculated value is greater than the

threshold, the pixel is grey as an edge.

4.2.2 Extending Edge Filters

In this study, Sobel, Kirsch, Prewitt, LoG and Canny edge detectors were chosen for border detection of skin cancer images. It was found that 3×3 filters, which are normally used in edge detection methods, are extremely localised. For better performance, the extended edge operators (5×5 filters) are used to cover more surrounding pixels [190]. The process involves convolving two 5×5 kernels with a matching 5×5 portion of a two-dimensional image. The purpose of convolving the kernels (edge operators) with the digital image is to compute an approximation of the derivative; one for horizontal, and one for vertical. The resulting derivative gives an approximation of the gradient of the image at that point. This in turn indicates an edge, where the gradients change. The abruptness of this change is measured against a threshold. If the resulting convolution is greater than the threshold then it is deemed to be an edge. The actual kernel values for edge detection operations are set out in the following. It can be seen that one kernel is simply rotated by 90 degrees. The Sobel operator deploys two kernels which are convolved with input image, which can be used to calculate vertical and horizontal changes. These 3×3 kernels can be obtained by the equation (4.1).

$$G_x = \begin{bmatrix} -1 & 0 & 1 \\ -2 & 0 & 2 \\ -1 & 0 & 1 \end{bmatrix}, G_y = \begin{bmatrix} 1 & 2 & 1 \\ 0 & 0 & 0 \\ -1 & -2 & -1 \end{bmatrix} \tag{4.1}$$

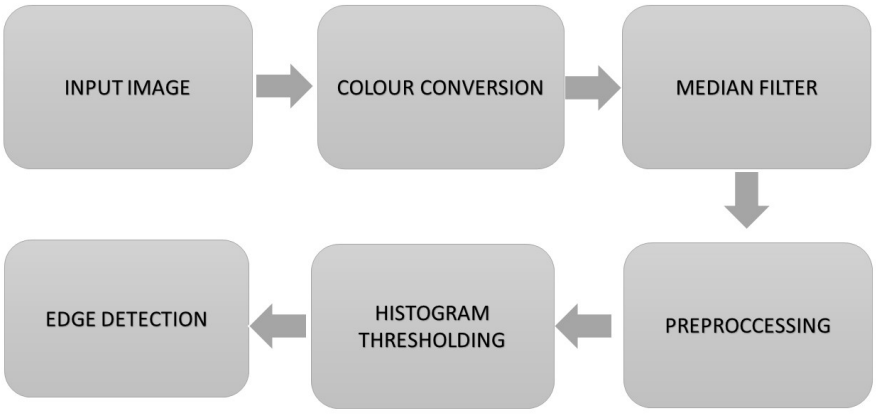

Figure 4.1: Flowchart of the border detection algorithm.

Above G_x and G_y Kernels can be extended to 5×5 masks as shown in equation (4.2) [190].

$$G_x = \begin{bmatrix} 2 & 2 & 4 & 2 & 2 \\ 1 & 1 & 2 & 1 & 1 \\ 0 & 0 & 0 & 0 & 0 \\ -1 & -1 & -2 & -1 & -1 \\ -2 & -2 & -4 & -2 & -2 \end{bmatrix}, G_y = \begin{bmatrix} 2 & 1 & 0 & -1 & -2 \\ 2 & 1 & 0 & -1 & -2 \\ 4 & 2 & 0 & -2 & -4 \\ 2 & 1 & 0 & -1 & -2 \\ 2 & 1 & 0 & -1 & -2 \end{bmatrix} \tag{4.2}$$

The Kirsch operator is the another technique that can be used for edge detection. The vertical and horizontal masks of this operator can be obtained using two 5×5 masks (G_x and G_y) which are provided in equation (4.3) [190].

$$G_x = \begin{bmatrix} 9 & 9 & 9 & 9 & 9 \\ 9 & 5 & 5 & 5 & 9 \\ -7 & -3 & 0 & -3 & -7 \\ -7 & -3 & -3 & -3 & -7 \\ -7 & -7 & -7 & -7 & -7 \end{bmatrix}, G_y = \begin{bmatrix} 9 & 9 & -7 & -7 & -7 \\ 9 & 5 & -3 & -3 & -7 \\ 9 & 5 & 0 & -3 & -7 \\ 9 & 5 & -3 & -3 & -7 \\ 9 & 9 & -7 & -7 & -7 \end{bmatrix} \tag{4.3}$$

The Canny edge detector is another approach to find the edges in images using a Gaussian filter to reduce noise when the raw image is convolved with this filter [191]. Equation (4.4) provides the masks for 5×5 Canny edge detection [192].

$$G_x = \begin{bmatrix} -1 & -1 & 0 & 1 & 1 \\ -2 & -1 & 0 & 1 & 2 \\ -2 & -2 & 0 & 2 & 2 \\ -2 & -1 & 0 & 1 & 2 \\ -1 & -1 & 0 & 1 & 1 \end{bmatrix}, G_y = \begin{bmatrix} -1 & -2 & -2 & -2 & -1 \\ -1 & -1 & -2 & -1 & -1 \\ 0 & 0 & 0 & 0 & 0 \\ 1 & 1 & 2 & 1 & 1 \\ 1 & 2 & 2 & 2 & 1 \end{bmatrix} \tag{4.4}$$

The second-order gradient Laplacian of Gaussian (LoG) edge detector can be used by convolving the LoG filter with the image [193]. Equation (4.5) provides the related 5×5 mask for an LoG filter [194].

$$G_x = \begin{bmatrix} 0 & 0 & -1 & 0 & 0 \\ 0 & -1 & -2 & -1 & 0 \\ -1 & -2 & 16 & -2 & -1 \\ 0 & -1 & -2 & -1 & 0 \\ 0 & 0 & -1 & 0 & 0 \end{bmatrix} \tag{4.5}$$

And finally, vertical and horizontal kernels of a 5×5 Prewitt edge detection operator are provided in equation (4.6) [190].

$$G_x = \begin{bmatrix} 2 & 2 & 2 & 2 & 2 \\ 1 & 1 & 1 & 1 & 1 \\ 0 & 0 & 0 & 0 & 0 \\ -1 & -1 & -1 & -1 & -1 \\ -2 & -2 & -2 & -2 & -2 \end{bmatrix}, G_y = \begin{bmatrix} 2 & 1 & 0 & -1 & -2 \\ 2 & 1 & 0 & -1 & -2 \\ 2 & 1 & 0 & -1 & -2 \\ 2 & 1 & 0 & -1 & -2 \\ 2 & 1 & 0 & -1 & -2 \end{bmatrix}, \tag{4.6}$$

4.2.3 Hardware-Software Implementation On The Proposed System

As discussed in Chapter 3, we propose using the ZYNQ-7000 SoC to create our portable solution for melanoma detection. One of the main advantages of this platform is that its FPGA side is totally reconfigurable. Therefore, the suggested implementation can be modified or changed if required. In this thesis, we investigated the edge detection method using high-resolution images to show the feasibility, power and real-time speed of this platform for implementation of border detection as a computationally expensive task of image processing. It should be noted that implementation of the other methods that used/proposed in this thesis (such as deep learning and classification) on Embedded systems is part of the future work the area. Figure 4.2 shows the block diagram of the proposed system that was implemented on the ZYNQ-7000.

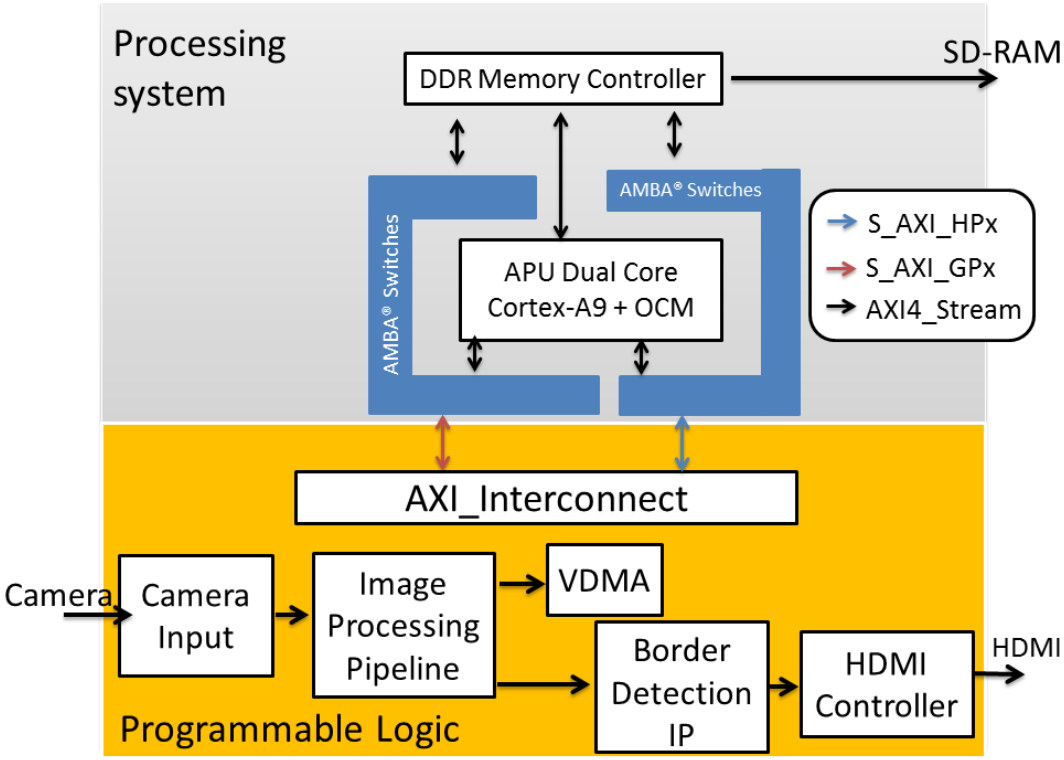

Figure 4.2: The block diagram of the proposed system including border detection IP implemented on ZYNQ-7000.

An image processing pipeline consists of several predefined XILINX video Intellectual Property (IP) cores such as defective pixel removal, de-mosaic, colour correction matrices. An IP in FPGA or ASIC contexts is a reusable building blocks or chip layout design that can be used in different system on chip designs. In order to generate the border detection IP, we first used OpenCV functions to evaluate the proposed algorithms and then VIVADO HLS software was used to convert C to synthesizable FPGA codes automatically. Additional IPs such as feature extraction and image classification can be developed and added to the system for the skin cancer detection application.

Unlike the traditional FPGA design flows, HLS can improve design quality, accelerate the design and verification tasks by applying optimal synthesis directives to transform C/C++/SystemC code specifications to register transfer level (RTL) implementation [151, 161]. Although C code is used for implementation of the algorithm, several directives such as DataFlow, memory/interface, and for loop optimizations [184] are applied to obtain the required performance and area utilization in the programmable logic. Functional verification of the edge detection IP is done using C++ test benches to significantly reduce the development time during the functional verification stage.

The proposed method was implemented and tested on the processing system

of a ZYNQ-7000 (ARM processor) using the original OpenCV functions. Due to the low speed performance of the processor, the same algorithm was implemented on the FPGA side of ZYNQ using VIVADO HLS and XILINX Video Library. It should be noted that the current version of the VIVADO HLS tool takes advantage of a limited number of synthesizable OpenCV functions which are used to develop the border detection IP. Figure 4.4 illustrates the border detection result applied to clinical images. The output results tested on a ZC702 evaluation board achieved the same imaging results as an ARM processor, with a higher speed of 60 fps.

Although C code is used for implementation of the algorithm, several directives such as DataFlow, memory/interface, and loop optimisations are applied to achieve the performance requirement and area utilisation in the PL. Functional verification of the edge detection IP is done using C++ test benches. In this project, I used BMP skin images as an input and verified the functionality of the code in one environment directly. This feature significantly reduced the development time during the functional verification stage. In addition, Figure 4.3 shows the IP generated using the VIVADO HLS, which performs edge-detection in real-time (60 fps).

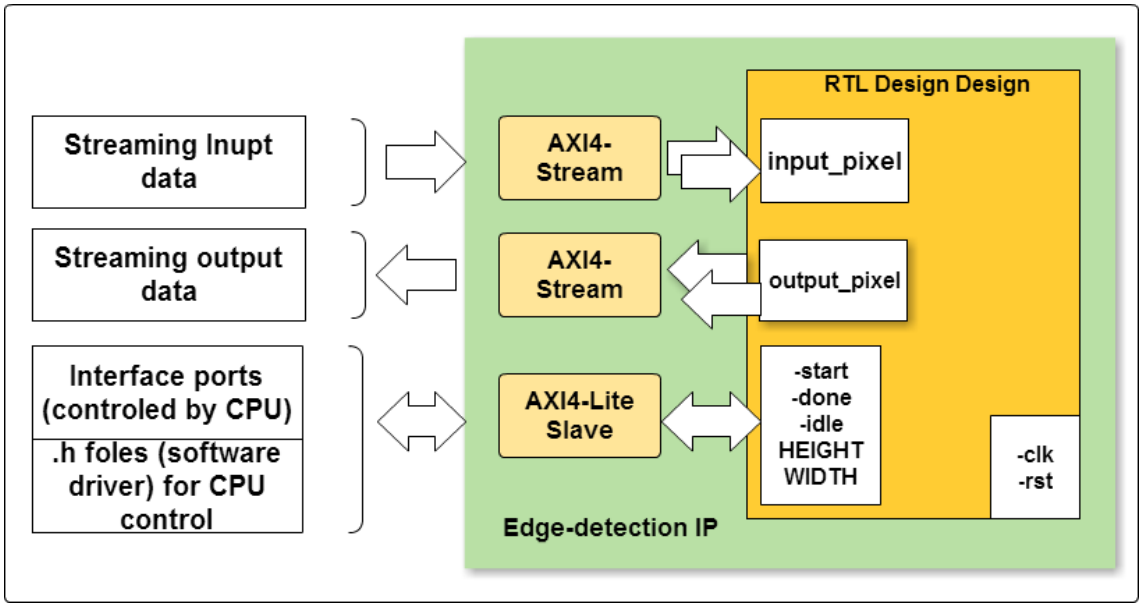

Figure 4.3: Block diagram of implemented border detection IP using VIVADO HLS.

4.2.4 Experimental Result

Figure 4.4, shows the result of applying the lesion border detection IP that match the detected border on the original input image.

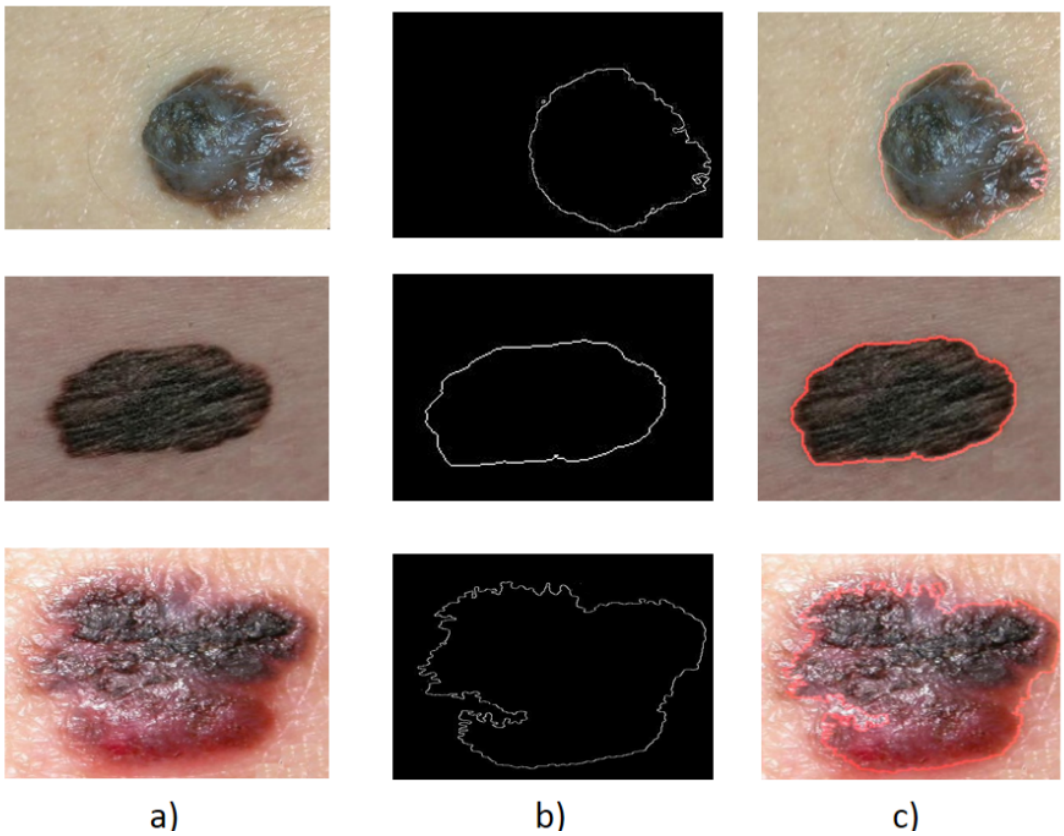

Figure 4.4: Border detection results. a) Original clinical images, b) Result of border detection using VIVADO HLS, c) Matching the detected border on the original image.

Furthermore, the results for Sobel, Kirsch, LoG and Canny edge detection implementations are compared. Table 4.1 shows the accuracy of edge detection measurement using the Jaccard index as presented in equation (4.7). The Jaccard similarity coefficient score, also known as the Jaccard index, is a metric that is used for comparing similarity and diversity in samples of data. This coefficient can be used to calculate accuracy by measuring the similarity between the segmented image (obtained by applying the algorithm) and the ground truth image. In this study, the ground truth images are obtained manually by excluding the lesion area from the normal skin. The Jaccard index can be expressed as the size of the intersection divided by the size of the union of the sample set from the following equation:

$$J(A,B) = \frac{|A \cap B|}{|A \cup B|} = \frac{|A \cap B||}{|A| + |B| - |A \cap B|} \tag{4.7}$$

where $0 \leq J(A,B) \leq 1$. In equation (4.7), $|A \cap B|$ is the intersection and $|A \cup B|$ is the union of two sets of A and B.

This measurement is obtained by applying an edge detection operation on each channel of the HSV, RGB colour components. The testing accuracy is obtained

using 52 most challenging images that we had in the dataset (not all images). The results show that the extended 5×5 Canny edge detection (applied on V channel) achieved an accuracy of 65.32% and performed better than other methods. Note that we normalised the result values to be between 0 and 100.

In addition, we implemented this algorithm on the ZYNQ-7000 board using HLS VIVADO tool. In order to analyse the power of processing of this platform, we tested the edge detection algorithm using a real-time video stream with high quality resolution (1980 x 1820 pixels) with the following options:

1. Implementation of the generated IP on FPGA side.
2. Implementation of the C++ source code on programming side (ARM processor).

The generated IP was able to process the input image in high-resolution quality with real-time speed on FPGA side. The average of processing time on FPGA side was 90 frame per second (fps) using a video file with 1900 pixel wide and 1200 pixel height. However, the ARM processor (Software side) performed the same algorithm with the same input with the average speed of 20 fps (implementation was vectorised (SIMD)).

4.3 Border Detection Using Colour Features

In section 4.2, we discussed use of edge detection for finding the borders of skin lesions. However, we realised that the accuracy of this method was not promising. In this section, we propose a semi-automated algorithm to increase the accuracy of lesion segmentation. This method investigates the power of the colour features of a clinical image and then uses clustering classification to assign labels to each pixel of the image. This method enables the user to select a small subset of the lesion and

Table 4.1: Accuracy of edge detection algorithms for border detection.

Edge Detector	H	S	V	R	G	B
5×5 LoG	22.44%	16.92%	51.30%	31.95%	29.92%	30.14%
5×5 Kirtch	19.31%	17.92%	52.45%	34.19%	32.15%	33.01%
5×5 Sobel	17.15%	18.97%	58.39%	56.86%	53.32%	55.98%
3×3 Sobel	16.52%	16.02%	55.65%	50.15%	47.36%	49.32%
3×3 Canny	15.31%	17.19%	61.51%	53.15%	49.53%	52.11%
5×5 Prewitt	19.83%	18.31%	62.97%	54.34%	53.13%	55.91%
5×5 Canny	24.23%	21.18%	**65.32%**	58.65%	54.39%	59.46%

specify the foreground lesion area. The proposed method consists of the following steps:

1. Pre-processing: the pre-processing step is performed to enhance and correct undesirable features remaining after image acquisition. The presence of artefacts such as hairs, ruler marks, shadows and variable illumination in clinical and dermoscopy images may affect lesion segmentation and result in an inaccurate diagnosis. Previous algorithms for pre-processing images for lesion detection can be generally categorised into artefact removal, shade removal and illumination (colour) correction. There are popular algorithms for hair removal such as Dullrazor [70]. Our image dataset includes a limited number hairy images and we used Dullrazor hair removal algorithm for removing hairs from our images. In addition, in the present study, we simply adopted the approach proposed in [87] for shading effect enhancement as our image dataset included shade effects. The conventional RGB was converted to the HSV domain and then Equation (4.8) was applied to the Value (V) channel in order to improve the highlight effects present in the images. Equation (4.8) is used for shading attenuation:

$$New\_V(x,y) = \frac{V(x,y)}{M(x,y)} \tag{4.8}$$

   where $V(x,y)$ is the Value channel of HSV image, $M(x,y)$ is the image obtained by morphological erosion of $V(x,y)$ (a disk = 20 is used for the structuring element of morphological operation) and (x,y) represents the pixel point. Figure 4.5 shows the result of illumination correction. Following the pre-processing step, the input RGB image is converted to Lab colour domain.

2. Select a small subset (rectangular) by manually clicking as the region of interest (ROI) inside the lesion (binary mask = ROI).

3. Assign the normal skin area (background) by complementing the ROI.

4. Extract the mean value of colour intensities (based on Lab colour image) from both the ROI (lesion) and background pixels.

5. Apply clustering classification using the K nearest neighbour (kNN) (K=3) algorithm using the extracted mean value of colour intensities and assign image pixels to lesion and background classes.

6. Applying morphological operations (dilation and erosion) for smoothing and removing unwanted artefacts to obtain a clean mask.

7. Remove objects that touch the frame border of the image. The main idea behind applying this operation is that generally a lesion is positioned in the

middle of a clinical image; remaining objects such as ruler markers or shading effects are generally located near the frame boundary of the image.

8. Multiply the original image to the created mask to obtain the segmented lesion.

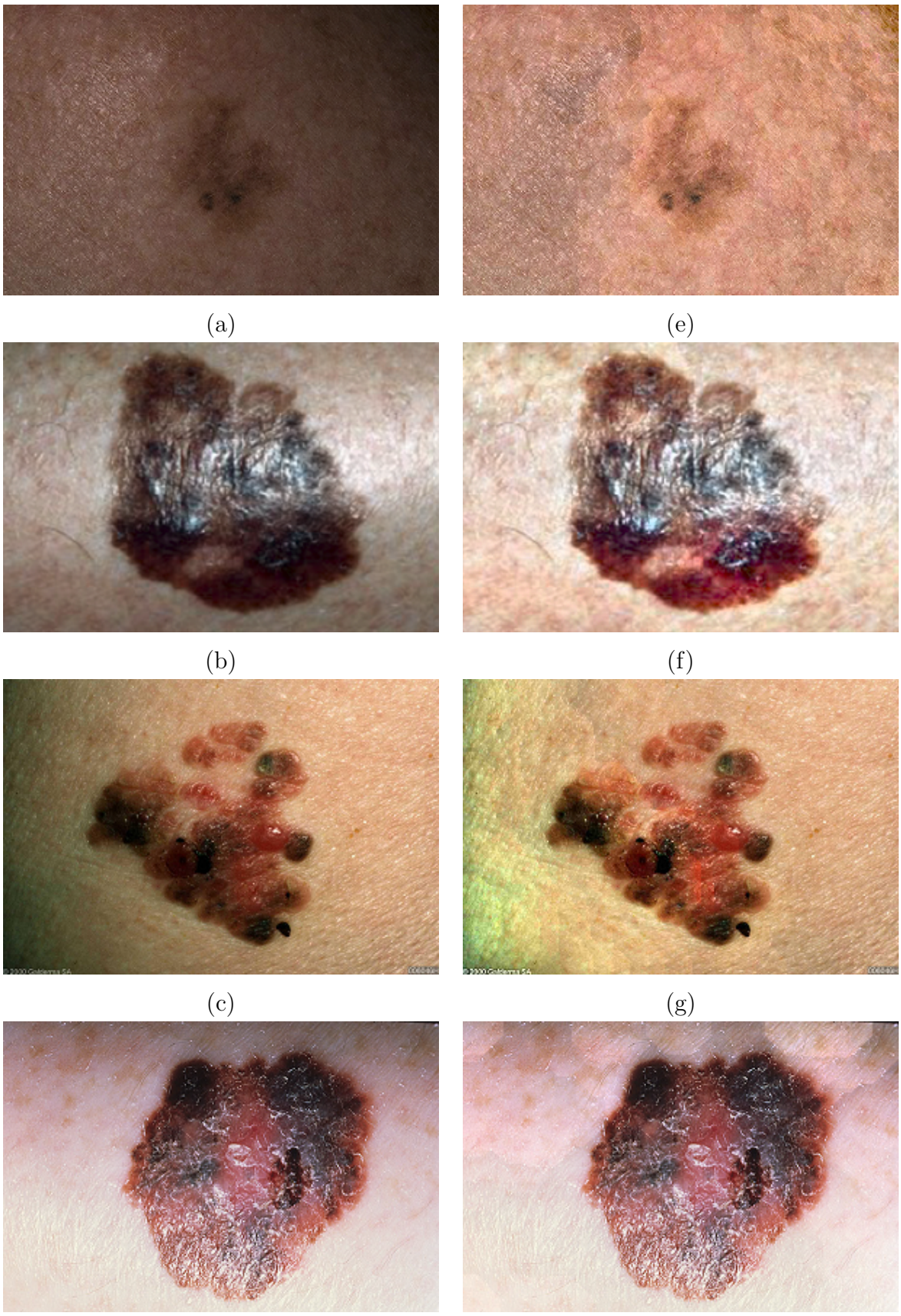

Figure 4.5: Example of images including shading and illumination issues; (a-d):original image and (e-h) corrected images.

4.3.1 Experimental Results

Figure 4.6 shows the results of the pre-processing and border segmentation phases. It indicates that using the proposed method the border of the lesion is well detected (Figure 4.6 (d)) compared with the threshold based (edge detection) lesion segmentation discussed in Section [4.2] (Figure 4.6 (c)).

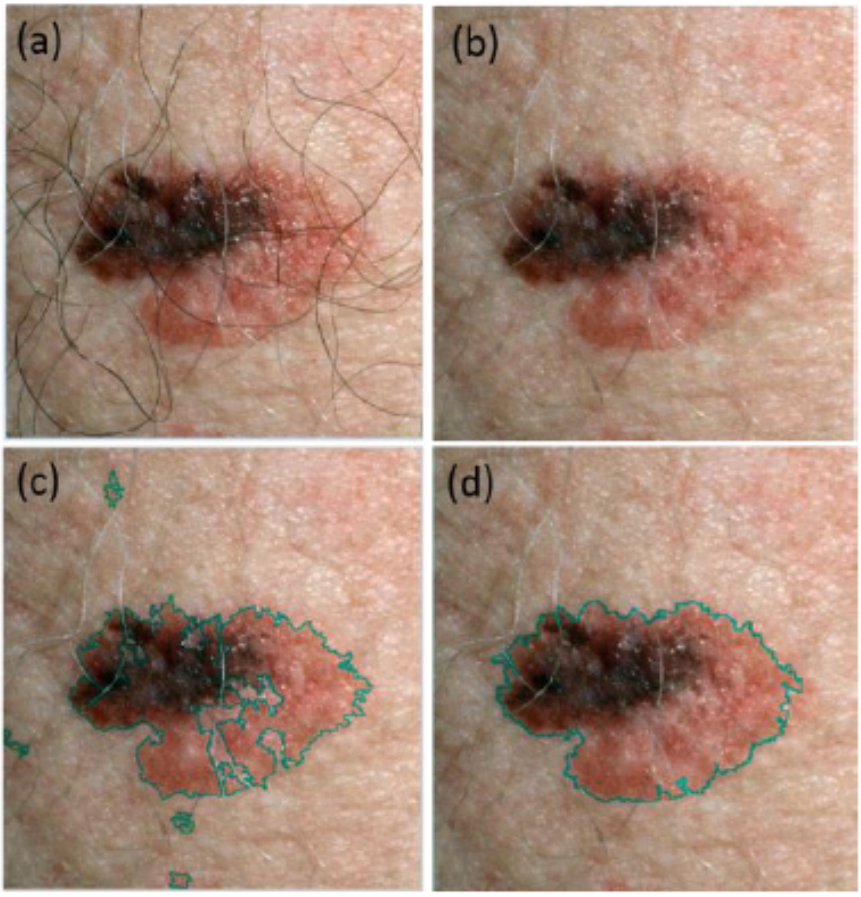

Figure 4.6: Result of proposed border detection method using colour features; a) original image, b) applying preprocessing (hair removal and shade correction), c) result of edge detection method proposed in Section 4.2, d) result of the proposed method.

A dataset of clinical images containing 150 images; 70 melanomas and 80 benign nevi was used for evaluating the accuracy of the lesion border detection. Ground truth images were determined manually for each image. The Tanimoto coefficient (Equation (4.9)) of similarity [195] was used to evaluate the accuracy of proposed method using the following equation:

$$TC_{(A,B)} = \frac{C}{A + B - C} \times 100 \tag{4.9}$$

where A is the total number of pixels in the ground truth image, B is the total

number of pixels in the segmented image and C is the total number of pixels that are common in both A and B. For each image, the TC index between the ground truth and the proposed method, were computed for all images. The mean TC's value of the proposed algorithms are compared with two other methods presented in [79, 108] using same testing image dataset and listed in Table 4.2. However, it should be note that the algorithms presented in [79, 108] are based on histogram thresholding. The difference in these approaches is mainly the method proposed for illumination correction.

Table 4.2: Comparison of the accuracy of the proposed system with two other methods.

Method	**Accuracy**
Our Method	89.32%
Cavalcanti [108]	71.87%
Glaister [79]	82.35%

In addition, the visual results of using the proposed border segmentation are illustrated in Figure 4.7. It can be seen that using this method the lesion's border is well detected in spite of the fact that other objects such as artifacts may exist. For example, in Figure 4.7-(a), it can be seen that there are ruler markers as well as a logo; however, the border is detected without the need to remove these objects. This is the main advantage of this method compared with edge-based border detection. However, the main issue with the proposed method is that it is a semi-automated application.

In addition, we investigate the accuracy of this method via Jaccard index and the same testing image dataset used for edge-based border detection. The proposed method achieved the accuracy of 80.23% and the experimental result showed that the suggested method can be used as a proper lesion detection tool in a practical CAD system for melanoma detection.

4.4 Lesion Border Detection Using Deep Learning and Convolutional Neural Network

The accuracy of the algorithm proposed in previous section was relatively high; but there are two main issues with this algorithm:

1. When applied to photographs including illumination reflectance from the skin

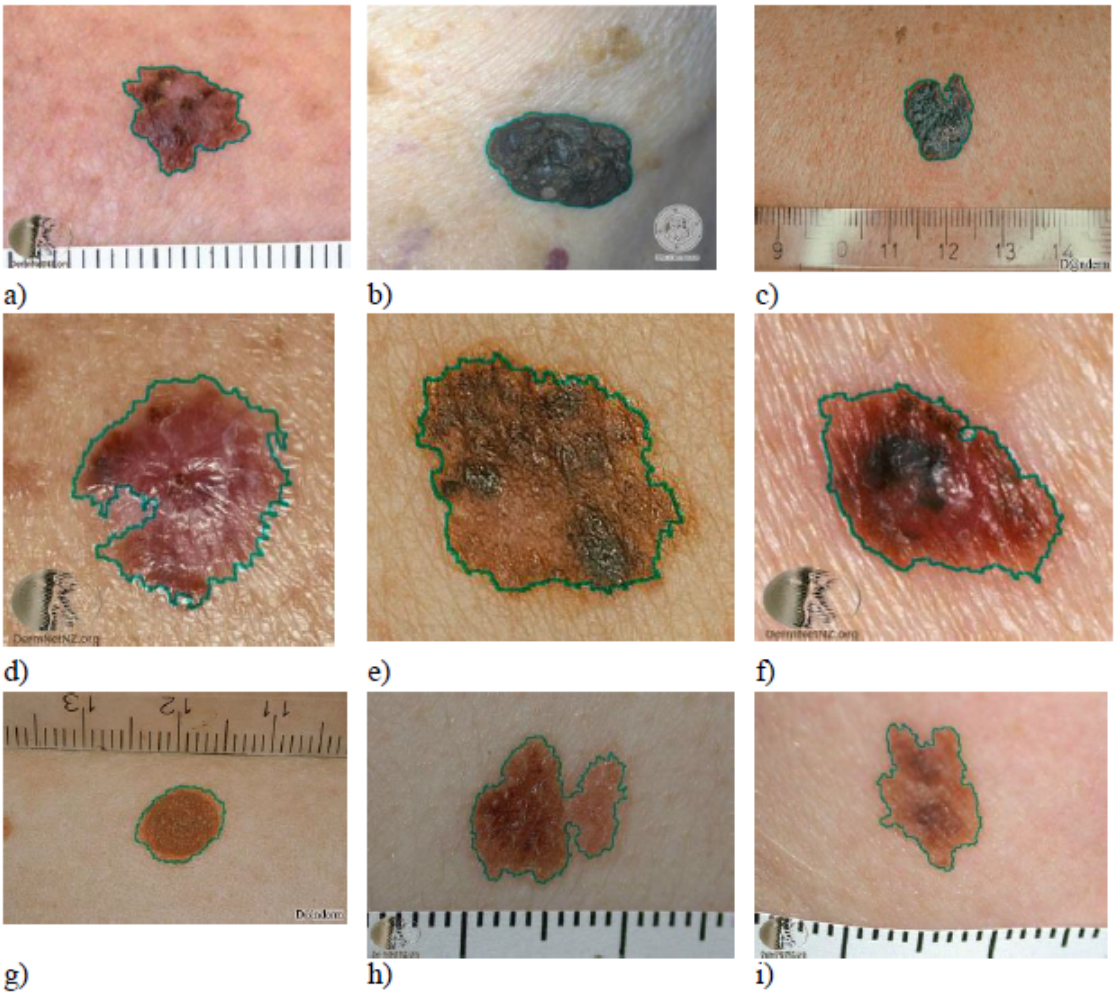

Figure 4.7: Result of applying the proposed method: Lesion border detection results by applying the proposed method, (a) and (c-f): malignant melanoma; (b): Seborrheic Keratosis; (g-i): benign nevus.

surface, any part of the healthy skin that is darker will be segmented as part of the lesion, resulting in an inaccurate segmentation.

2. The proposed method is a semi-automatic approach, meaning that the user needs to select a region of interest (a part of the lesion area).

Therefore, reflected illumination from the skin surface can affect the border detection result. The existing general illumination correction algorithms are not useful when applied to skin lesion images. In this work, we proposed a novel automatic method that uses Convolutional Neural Networks (CNN) for lesion border detection in clinical images. To the best of our knowledge, this method has not been applied to border detection in clinical images so far. The main advantage of the proposed method is that no pre-processing algorithm (such as hair removal or illumination correction) is required, unlike previous border detection methods.

4.4.1 Convolutional Neural Networks (CNN)

CNNs are a category of feed-forward artificial neural networks [196, 197]. In this approach, each neuron responds to an overlapping region in the visual field of view. CNNs are a variation of Multilayer Perceptrons (MLPs) and were inspired by the biological process of the human brain. These methods are used in the context of machine learning as well as machine vision, requiring a minimal amount of pre-processing e.g. object recognition [198].

CNNs are trainable architectures that consist of multilayers of small neuron groups that investigate small pieces of the input image, named receptive fields. The results of these small pieces are grouped in a way that they cover a good representation of the original image. The input image and output of each layer are collections of arrays called feature maps. In our method, the input is a colour (RGB) image and the feature maps are two-dimensional arrays including a colour channel of the RGB input. The feature map (in output) contains a feature which is extracted from entire pixels in the input image. CNNs may consist of multiple layers at each stage followed by a classifier. A key aspect of CNNs is the use of shared weight in convolutional layers. In other words, the equal weighted filter is applied for each pixel of feature maps in the layer, this decreases the required memory size and increase the speed of processing [199, 200]. In addition, the network learns the filters or features. Therefore, CNNs are less dependent on prior knowledge and sophisticated hand-crafted features. Using learned features instead of hand-engineered features for object classification is one the main benefits of CNNs. The four CNN layers are described as follows:

4.4.1.1 Spatial Convolutional Layer

One of the main features of CNNs is that the convolutional parameters in every filter in a CNN are trained towards the back-propagation process, while traditional convolutional kernels such as Sobel, Canny, LoG, Roberts and Prewitt contain particular coefficients. In the convolutional layer, an arbitrary number of filters are applied to the input image. For instance, in our design, the first layer includes sixteen 15×15 filters. Each filter is convolved with the input image; therefore, the result of each operation is a 2D image called the feature map. This procedure can be applied for the next layer of the CNN as well. However, if the prior layer is convolutional, each feature map is used as the input of the layer. These shared weights across the image are used to detect features without considering their location. Convolving these filters enables each filter to recognise different and distinctive features.

4.4.1.2 Rectified Linear Unit Layer (ReLU)

ReLU layer is one the state-of-the-art algorithms used in neural networks as an alternative to traditional sigmoid function [201]. This non-saturating function increases the non-linearity of the network in a way that the receptive fields in each layers remain unaffected. One advantage of using ReLU function is that the network trains significantly faster compared to sigmoid function.

4.4.1.3 Sub-sampling (pooling) Layer

The sub-sampling layer down-samples the input (size reduction). Several methods have been widely used to sub-sample 2D arrays, including max pooling, average pooling and stochastic pooling. In this work, we used max pooling in our CNN design. Max pooling divides the input image into several non-overlapping rectangular partitions and returns the maximum value of each sub-divided region. The main advantages of using max-pooling are dimensional reduction, and the fact that it enables the networks to become translation invariant for object recognition.

4.4.1.4 Fully-Connected Layer

The final layer in a CNN is the fully-connected layer, which connects all single neurons from the previous layers. This layer behaves similarly to a traditional classifier such as an MLP classifier. The 2D outputs from the previous layer are reshaped to one-dimensional before applying the classification process.

4.4.2 Experimental Result

4.4.2.1 Training and Testing Dataset

In order to train the network, we created a large dataset from our initial image dataset (described in previous section), with two main classes labelled as lesion and background. The background class includes normal skin (with hairs and ruler marker artefacts) and the lesion class contains lesion images. The training dataset contains 480 lesion and 1200 background images. The testing image set is same as the dataset used in previous section.

Given that lesions in a clinical image dataset are multi-scale, the main issue in using a CNN for lesion segmentation was that the window sizes of convolutional layers are fixed; therefore, the first layer may not see the entire lesion in the kernel window when sliding filters on the input image. In order to overcome this issue, we divided each image into 50×50 image patches and labelled each tile (patch) as lesion or background. No other pre-processing method, such as hair or ruler-marker removal, or colour/illumination correction was done during training.

4.4.2.2 Experimental Setup

In this experiment, our model is detailed as follows.

The first layer consists of:

- Spatial convolution layer: input is a 2D image (3 channels of dimension 50×50 of RGB input); it outputs 16 feature maps of dimension 36×36 (filter size is 15×15);
- Spatial Max-pooling layer which down-samples the 16 feature maps to a dimension of 18×18;
- ReLU non-linearity function.

The second layer consists of:

- Convolutional layer: input is 16 feature maps. It outputs 64 feature maps with a size of 5×5 (filter size is 14×14);
- Threshold;
- ReLU non-linearity layer.

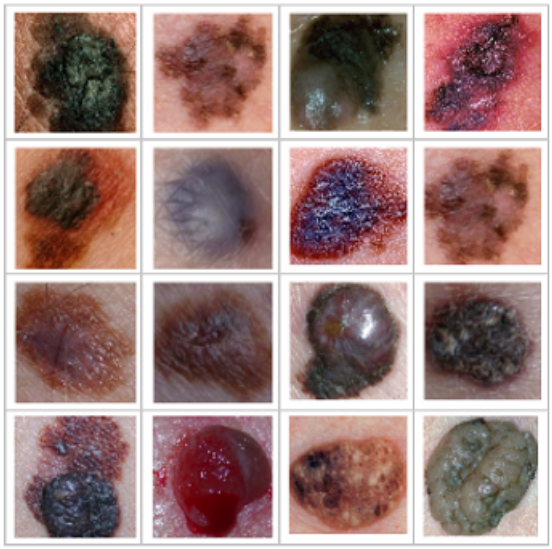

a) lesion samples

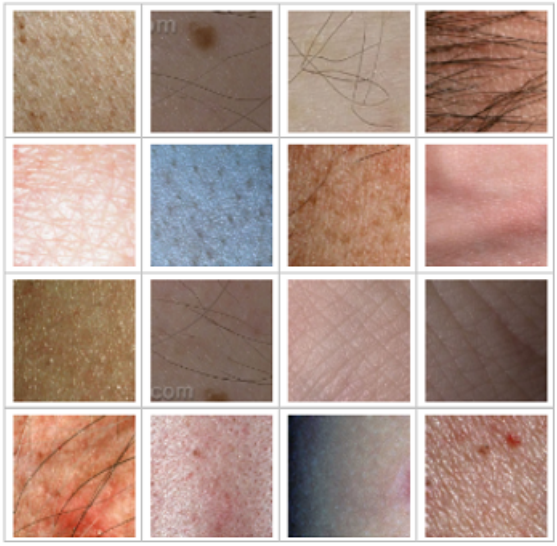

b) skin samples

Figure 4.8: Sample of training image dataset.

The final layer consists of:

- Convolutional layer: input: 64 feature maps, output is 128 feature maps with dimension size of 1×1 (filter size is 5×5);
- ReLU non-linearity function.

Table 4.3 summarise the detail of the architecture of the trained network.

Table 4.3: Architecture of the CNN network used for training in our experiment

CNN layer	1	2	3
# channels	16	64	128
Filter Size	15×15	14×14	5×5
input size	50×50	18×18	5×5

The output of the third layer including 128 channels of 1×1 array is connected to a MLP classifier. The MLP classifier contains 64 hidden layers and its output is a binary number (0 as the lesion and 1 as the background). In order to apply the proposed method to a large image (e.g. 460×380), the algorithm scans each 50×50 block of the input image and assigns a label to each block. The output of the algorithm is a binary mask labelling the segmented lesion with a smaller size than the original input image. Therefore, in order to lay the labelled segmented mask over the original images, it should be resized.

4.4.2.3 Results

Figures 4.9, 4.10 and 4.11 show the results of applying the trained network. Results show that the lesion is well detected in each image (see the second columns in Figures 4.9, 4.10 and 4.11). However, it can be seen that the initial segmented area is larger than the size of the lesion and the lesion borders are not detected accurately. The main reason is due to selecting a larger size of filter for training the CNN. However, if we change the size of filters to a smaller size, we need to increase the number of layers of the CNN which produces a tiny mask at the output. This issue causes to generate a larger segmented lesion area after resizing with a low resolution. In order to overcome this issue, it was necessary to smooth the border of the lesion by applying a post-processing algorithm. We investigated different methods in order to determine the border more precisely, including:

1. Kmeans clustering for lesion segmentation.

2. Considering an active contour to detect the edges of the lesion using the initial mask obtained from the network.

3. Segmentation based on thresholding methods: Otsu's thresholding.

4. Interactive segmentation using the method proposed in [94].

5. Applying morphological operation: dilation filter by a disk (r=15) on the initial mask.

Based on our experiments, the best result was achieved by applying morphological operations (closing operation). We also tried to test the most challenging images mentioned in [79] for segmentation. The proposed method achieved an accuracy of 86.67% using the same image dataset used in Sections 4.2 and 4.3. Figures 4.9 , 4.10 and 4.11 show the visual results obtained by applying the proposed CNN method based on the most challenging clinical images without using any pre-processing method.

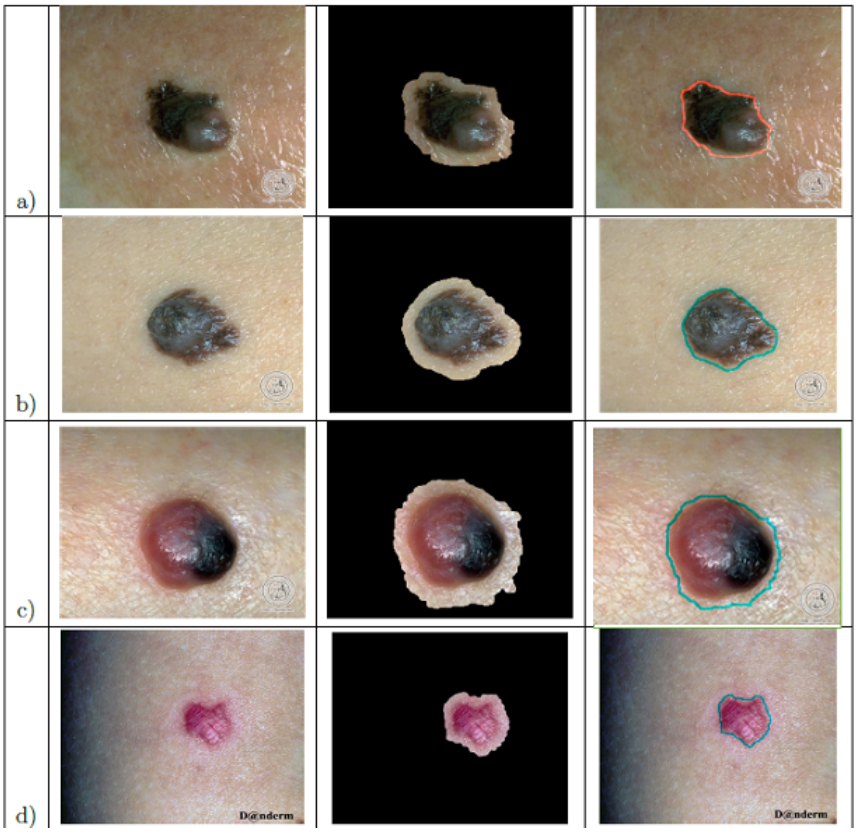

Figure 4.9: Result of the proposed method: (a), (d), (c) and (d) rows: the 1st column is the original images; the 2nd column is the initial result of CNN and the 3rd column is the output of CNN after post-processing.

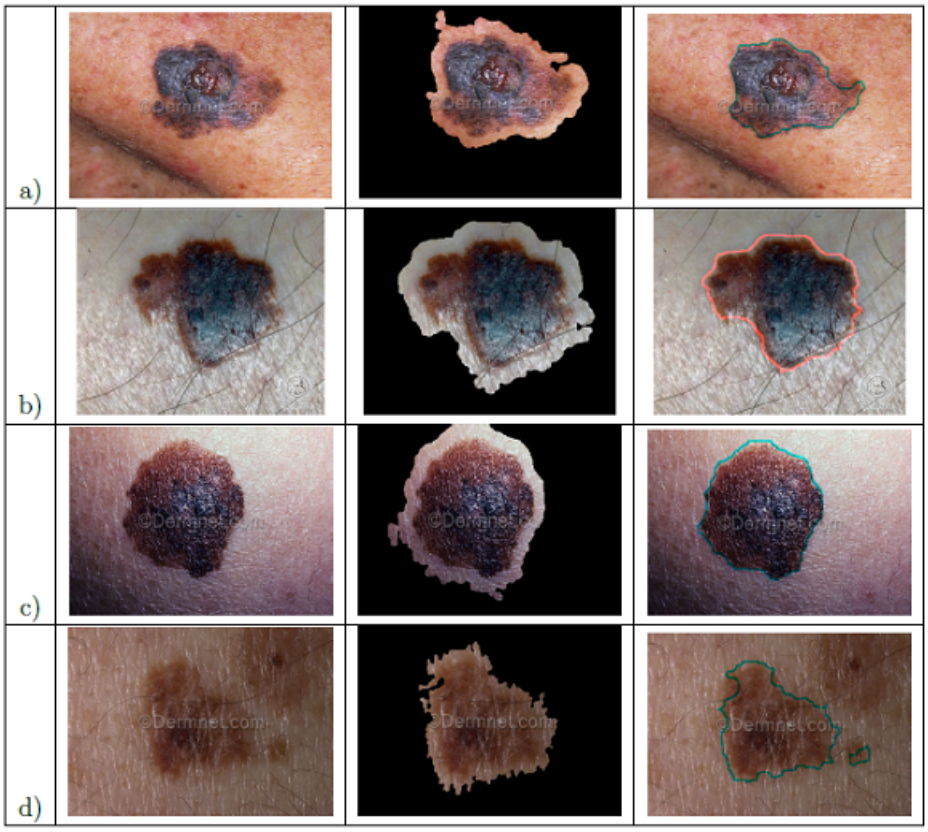

Figure 4.10: Result of the proposed method: (a), (d), (c) and (d) rows: the 1st column is the original images; the 2nd column is the initial result of CNN and the 3rd column is the output of CNN after post-processing

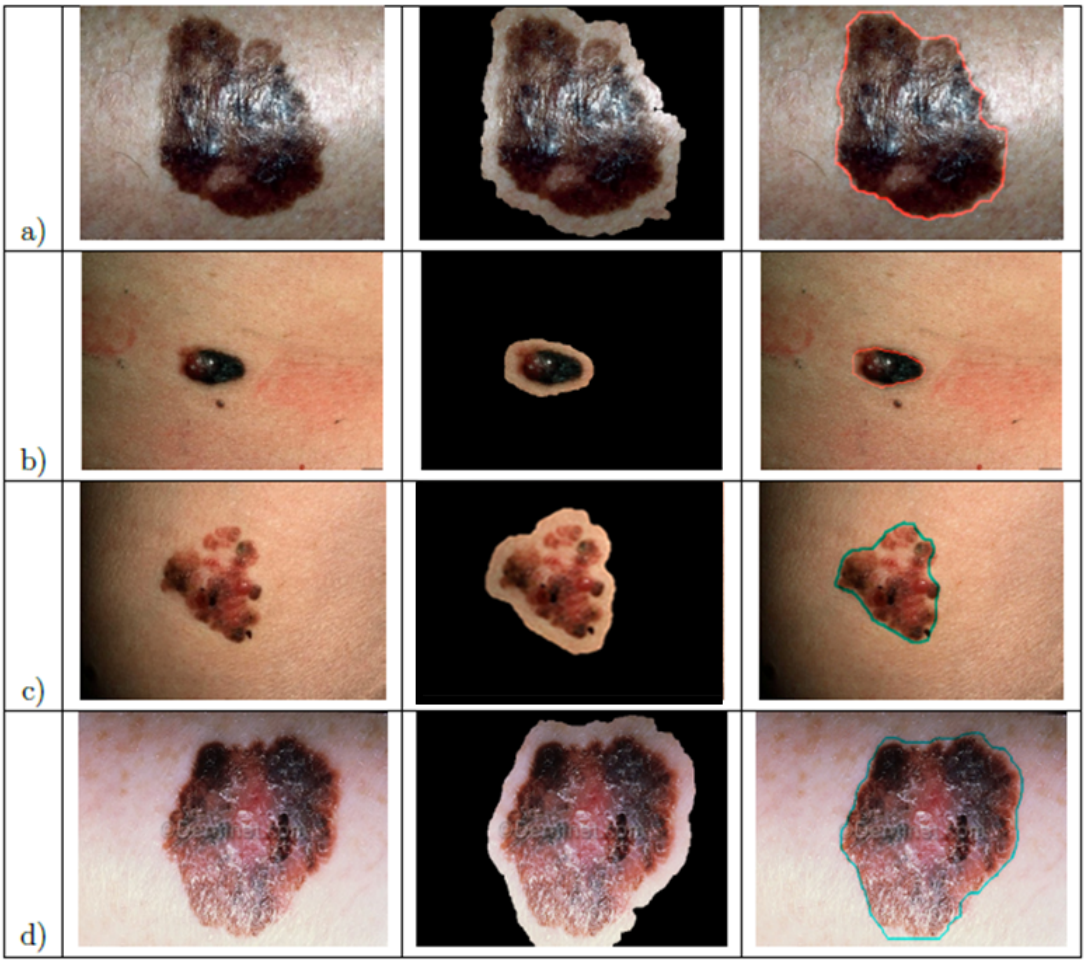

Figure 4.11: Result of the proposed method: (a), (d), (c) and (d) rows: the 1st column is the original images; the 2nd column is the initial result of CNN and the 3rd column is the output of CNN after post-processing.

4.4.3 Summary

The effect of applying morphological filters and edge detection algorithms to skin lesion images in order to detect the borders of PSLs is discussed with reference to the use of a ZYNQ-7000 single SoC. The results show that the extended 5×5 Canny edge detection implemented on the proposed embedded platform performed better than other reported methods. It can segment the lesion, which is an important step before image analysis and feature extraction for melanoma detection. Moreover, using C-to-FPGA technology and VIVADO HLS software, we can increase the productivity and performance of the system compared with current FPGA programming approaches. However, there is a trade-off between strong edge detection and noise, as is apparent when comparing the Sobel and Prewitt operators. It was found that pre-processing of the image may, in some circumstances, result in less noise in the output. Synthesizing the IP used in this application allows a real-time result. This is achieved by the fact that the edge detection IP is working in parallel for RGB images. The throughput is achieved by running processes in parallel rather than all-out speed. Employing other optimisation techniques for image analysis can enhance performance. The advances in high-definition media in recent years, the development of high-speed embedded systems and the growth of applications in health-care systems provide the opportunity to revolutionise skin cancer diagnosis. In this work, using state-of-the-art FPGA technology as an example, we implemented the fundamental image processing algorithms on an SoC and demonstrated rapid processing power that supports such a transition.

In this chapter, a semi-automatic border detection method was also proposed and the accuracy of the algorithm was compared with two other methods. The proposed method achieved an accuracy of 80.23% (Jaccard index) and the experimental result showed that the suggested method can be used as a proper lesion detection tool in a practical CAD system for melanoma detection. However, the main drawback within this method is that it is user-dependent and performs semi-automatically.

Finally in this chapter, a CNN-based method was proposed for as our preferred border detection algorithm. The experimental results of this study show that lesion borders can be detected for lesion segmentation of challenging clinical images without applying a pre-processing step such as hair removal and/or illumination correction. The suggested method can be used as a proper lesion detection tool in a practical CAD system for melanoma detection. It achieved an accuracy of 86.67% (using Jaccard index). The following chapter discusses the methods used for feature extraction and the feature selection algorithms we used in this study.

The following chapter discusses the methods we use for feature extraction and feature selection algorithms we used for this study.

Chapter 5

Feature Extraction and Feature Selection

5.1 Introduction

Development of an accurate and efficient CAD system is necessary for a practical diagnostic process. A CAD system for melanoma diagnosis consists of several stages; image acquisition, lesion border segmentation, feature extraction, feature selection, and classification. Lesion border detection was discussed in the previous chapter.

This chapter presents the algorithms that we used for feature extraction, and feature selection. First, it presents the goal of the feature extraction algorithms that are used for the melanoma detection system. For feature extraction, the proposed attributes are based on shape, colour and texture features. In addition, the methodology for feature selection is discussed.

5.2 Feature Extraction

The aim of feature extraction is to estimate particular attributes and differentiate one object pattern from another in the photographs. It is crucial to identify the most robust and effective features to be extracted from skin lesions that will be used for diagnosis of the melanoma by a classifier. In our case, feature extraction involves measuring particular properties of the pixels of the segmented lesion. Several feature extraction methods were found in the literature that applied to clinical images; these approaches can be categorized into three groups: shape-based (geometrical features), colour-based, and texture based.

5.2.1 Shape Analysis

Geometrical features of the skin lesions can provide important information in the diagnosis of melanoma. The main procedure for extracting shape features is the analysis of segmented masks, obtained from the border detection step. It is necessary here to clarify exactly what is meant by shape features. Shape feature extraction is a process in which a number of parameters from the binary mask of the segmented lesion are calculated. The parameters measured for shape analysis included area, perimeter, eccentricity, compactness, thinness, dispersion, circularity, kurtosis, skewness, major and minor axis length.

Distance: Distance is a real-valued function of two image points, satisfying the following properties:

$$d\Big\{(p_1, p_2)\Big\} \geq 0 \tag{5.1}$$

$$d\Big\{(p_1, p_2)\Big\} = d\Big\{(p_2, p_1)\Big\} \tag{5.2}$$

$$d\Big\{(p_1, p_2)\Big\} + d\Big\{(p_2, p_3)\Big\} \geq d\Big\{(p_1, p_3)\Big\} \tag{5.3}$$

where $p_i = (x_i, y_i)$ is the image pixel points. By calculating the distance parameter, we can define various parameters for shape features. The "Euclidean distance" is one of the most common functions that is used in image analysis [202] by given:

$$d_E = \Big[(p_1 - p_2)^2\Big]^{\frac{1}{2}} \tag{5.4}$$

Area: The area of each segmented lesion within an image can simply obtained by counting the total number of pixels in the segmented lesion.

Perimeter: The perimeter of each object is equal to the total number of pixels around the border of the segmented lesion starting at an random initial point and returning to the initial point.

Circularity: To measure and quantify the asymmetry of the lesion, a circularity index can be calculated. This value can be obtained using the area (A) and perimeter

(P) of the skin lesion as:

$$\text{Circ} = \frac{4\pi A}{P^2} \tag{5.5}$$

Major and Minor Axis Length: The major and minor axes are obtained by measuring the distance of area between the two halves of the segmented lesion, taking the major symmetry axis (Equation (5.6)) and the minor axis of symmetry (by rotating the major axis by 90°), where θ is the orientation of the major symmetry axis [114].

$$\tan 2\theta = \frac{2\sum_{i=1}^{n} x_i y_i}{\sum_{i=1}^{n} x_i^2 - \sum_{i=1}^{n} y_i^2} \tag{5.6}$$

Following calculation of the major and minor axes, the binary mask is folded along these two lines and the distance between the two halves of the lesion are measured using XOR operation [114]. The asymmetry feature can be obtained by:

$$\text{Asymmetry Index} = \frac{A_D}{A} \times 100 \tag{5.7}$$

where A_D is the distance between the two halves [114].

Longest Diameter (LD): The length of the distance between two farthest border points which passes across the lesion centroid (C), is the longest diameter [114]. This parameter can be obtained by:

$$(x_C, y_C) = \left(\frac{\sum_{i=1}^{n} x_i}{n}, \frac{\sum_{i=1}^{n} y_i}{n}\right) \tag{5.8}$$

where n is the total number of pixels inside the segmented lesion, and (x_i, y_i) are the coordinates of the i_{th} pixel [114].

Shortest Diameter (SD): The distance between two closest border points which passes across the lesion centroid [114].

Irregularity Index A (IrA):

$$IrA = \frac{P}{A} \tag{5.9}$$

Irregularity Index B (IrB):

$$IrA = \frac{P}{LD} \tag{5.10}$$

Irregularity Index C (IrC):

$$I_{RC} = LD - SD \tag{5.11}$$

5.2.2 Colour-based Features

Colour analysis is one of the most important methods for analysing medical images. In the skin image analysis field, typically the original RGB image is transformed to different colour domains (e.g. HSV, CIELAB, YUV) in order to measure corresponding colour information from colour channels. Other image formats may be superior for a specific application [128].

Colour moments can be used as colour features in image processing. Colour moments estimate the representation of colour distribution in an image and specify a measurement for colour similarity between images. They are scaling and rotation invariant and encode both shape and colour information for feature extraction. In image processing, colour moments are measured per channel (e.g. nine moments for an HSV image). Computation of colour moments of an image can be interpreted in a similar manner on the basis of probability distributions (e.g. normal distribution).

Mean: The first colour feature is the average colour in an image, and it can be measured by:

$$E_i = \sum_{j=1}^{N} \frac{1}{N} P_{ij} \tag{5.12}$$

where N is the total number of pixels of the image and P_{ij} is the intensity value of the j_{th} pixel at the i_{th} channel of the image.

Standard Deviation: The standard deviation is the second colour feature and can be obtained by taking the square root of the variance of the colour histogram [203].

$$\sigma_i = \sqrt{\frac{1}{N} \sum_{j=1}^{N} (P_{ij} - E_i)^2} \tag{5.13}$$

where E_i is the mean value (the first colour feature) of the i_{th} colour channel plane.

Skewness: The third colour feature is the skewness and determines the asymmetrical distribution the colour histogram for each colour channel.Thus, it provides

information about the shape of the colour distribution [203]. Skewness can be obtained by the following equation:

$$s_i = \sqrt[3]{\frac{1}{N}\sum_{j=1}^{N}(P_{ij} - E_i)^3} \tag{5.14}$$

Kurtosis: Kurtosis is the fourth colour features, and it also provides information about the shape of the colour distribution. However, Kurtosis determined that "how flat or tall the distribution is in comparison to normal distribution" [203].

$$k_i = \sqrt[4]{\frac{1}{N}\sum_{j=1}^{N}(P_{ij} - E_i)^4} \tag{5.15}$$

Energy: This descriptor is considered based on gray-level distribution. The maximum value is where the image contains a constant value and is defined as follows:

$$Energy = \sum_{i=0}^{r-1}\sum_{j=0}^{c-1}\left\{P(ij)^2\right\} \tag{5.16}$$

where r and c denote the number of rows and columns respectively.

Colour Distribution Entropy (CDE): This colour feature is proposed to measure colour spatial details in an image [204]. It is defined based on a Normalised Spatial Distribution Histogram (NSDH) and entropy measurement [205, 206]. A_i is considered as the set of pixels with colour bin i of a channel of an image and $|A_i|$ is the number of elements in A_i. C_i and r_i are the centroid and the radius of colour bin i, respectively. Therefore, N concentric circles can be drawn when $\frac{jr_i}{N}$ is the radius for each $1 \leq j \leq N$. Besides, $|A_{ij}|$ is the count of the pixels of colour bin i inside circle j. Thus, the annular colour histogram can be written as ($|A_{i1}|$,$|A_{i2}|$,$\cdots$, $|A_{iN}|$) [206] (Figure 5.1).

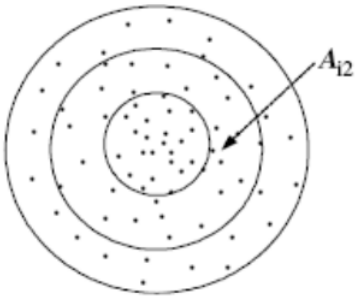

Figure 5.1: Annular Colour Histogram[206]

Considering the Annular Colour Histogram, the NSDH is computed as P_i and P_{ij}:

$$P_i = (P_{i1}, P_{i2}, \cdots, P_{iN}) \tag{5.17}$$

$$P_{ij} = \frac{|A_{ij}|}{A_i} \tag{5.18}$$

thus the CDE of the colour bin i is equal to:

$$\text{CDE} = -\sum_{j=1}^{N} P_{ij} \log_2 P_{ij} \tag{5.19}$$

5.2.3 Texture-based Features

Texture analysis is a technique for extraction and analysis of shape and spatial structure of images such as smoothness, coarseness, roughness and regular patterns. In this study, texture features were extracted from the grey level co-occurrence matrix (GLCM). The GLCM (also referred to as the second-order histogram,) is a statistical approach that uses measuring of co-occurrence probabilities based on spatial relations of gray level pixels in different angular directions. The GLCM is calculated from the segmented lesions and created by averaging different orientations matrices (angles of 0, 45, 90 and 135 degree). The distance is the pixels between the pairs of pixels that are used for the second-order statistics, and the angle refers to the angle between the pixel pairs.

Mathematically, the co-occurrence matrix is obtained by:

$$C_{\Delta x \Delta y}(i,j) = \sum_{p=i}^{m} \sum_{q=j}^{n} \begin{cases} 1, \text{ if } I(p,q) = i \text{ and } I(p+\Delta x, q+\Delta y) = j \\ 0, \text{ otherwise} \end{cases} \tag{5.20}$$

where C is the co-occurrence matrix for a $m \times n$ image, i and j are the image intensity of image I, p and q are the pixel points. In addition, the offset of the image is denoted by Δx and Δy which is depended on the direction of θ and the distance where the matrix is computed d [123].

Numerous features have been proposed via the above-mentioned method, but in this work, five of the most powerful features are used: energy, inertia, correlation, inverse difference and entropy [207]. We extracted these features based on segmented RGB images. We used the average of these features for the four angles, where C_{ij} is considered as the element of the co-occurrence matrix and is normalised by the number of pixel pairs in the matrix. The features are as follows:

Energy: is related to homogeneity (smoothness) and is obtained by calculating the distribution among the grey levels.

$$Energy = \sum_i \sum_j C_{ij}^2 \tag{5.21}$$

Inertia: is a parameter to calculate the contrast.

$$Inertia = \sum_i \sum_j (i-j)^2 C_{ij} \tag{5.22}$$

Correlation: is a parameter to find the similarity between pixels at the defined distance.

$$\text{Correlation} = \frac{1}{\sigma_x \sigma_y} \sum_i \sum_j (i-\mu_x)(j-\mu_y) C_{ij} \tag{5.23}$$

where:

$$\mu_x = \sum_i i \sum_j C_{ij} \tag{5.24}$$

and:

$$\mu_y = \sum_j j \sum_i C_{ij} \tag{5.25}$$

and:

$$\sigma_x^2 = \sum_i (i-\mu_x)^2 \sum_j C_{ij} \tag{5.26}$$

and:

$$\sigma_y^2 = \sum_j (j-\mu_y)^2 \sum_i C_{ij} \tag{5.27}$$

Inverse Difference: Inverse difference moment is the measure of local homogeneity of the texture and is defined as:

$$\text{Inverse Difference} = \sum_i \sum_j \frac{C_{ij}}{1 + (i-j)^2} \tag{5.28}$$

Entropy: this factor provides a measurement for the content of the texture.

$$\text{Entropy} = -\sum_i \sum_j C_{ij} \log_2 C_{ij} \tag{5.29}$$

5.3 Feature Selection

Feature selection is an approach for distinguishing the optimal feature set in a dataset to be used by a classifier. This approach is placed between feature extraction and classification. Feature selection reduces the number of features that are less dominant while preserving the most discriminating feature subset from the initial dataset created in the feature extraction step.

Typically, a feature selection algorithm is composed of four key components: the subset generator, subset evaluator, stopping criterion and a result validation process (Figure 5.2). The subset generator produces subsets according to a certain search method. Each generated subset is then evaluated through the subset evaluator by applying certain criteria. The performance of each subset is compared with the previous best subset. This procedure is repeated until the best subset is obtained, then it is stopped using the given stopping criterion. In the result validation step, a new testing dataset is tested to validate the feature selection algorithm.

Feature subset selection (FSS) determines a reduced subset of features from the original feature dataset. Feature ranking (FR), also known as feature weighting (FW) evaluates features separately and assigns weights to each feature based on the degree of relevance. The key aspects of using feature selection are:

- Increasing the accuracy of the classification system,
- Dimensionality reduction, thus less computational cost,
- Reducing the training time,
- Avoiding over-fitting issues which may occur in the classification process.

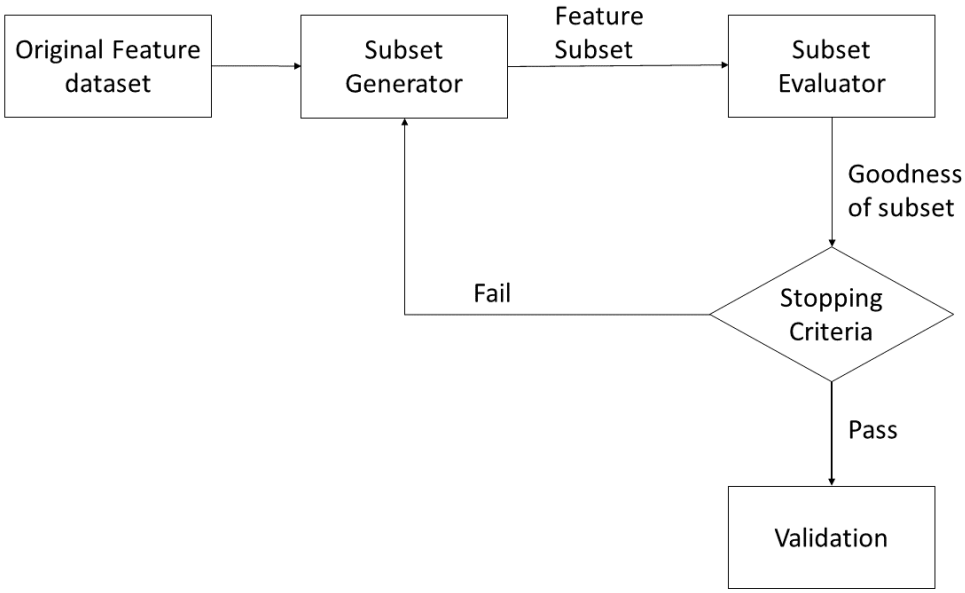

Figure 5.2: Four key steps of a basic feature selection algorithm.

Feature selection methods are mainly divided into three different categories [208] as follows:

1. Filter-based method: this method uses all features of the data as the input to analyze the features and select the optimal feature subset(s) without considering any classification/learning algorithm.

2. Wrapper-based method: in this method, a learning/classification algorithm is employed to search for features which improve the classification accuracy. This method is more computationally expensive than the filter-based method.

3. Hybrid model: is a combination of the two above methods.

In this work, we used a correlation-based feature-selection (CFS) method to find the optimal features. This method is a multivariate filter algorithm that evaluates and ranks based on a correlation-based heuristic evaluation function [209]. This algorithm evaluates the value of subsets of features to produce an optimal subset based on the degree of redundancy between features. The generated subset should include the features that have highest correlation with the class (label) and lowest correlation with each other [209]. The CFS algorithm measures two main factors called Merit and CFS Criterion to be used in an optimisation problem. The Merit of a feature subset S containing k features is obtained by [210]:

$$\text{Merit}_{S_k} = \frac{k\overline{r_{cf}}}{\sqrt{k + k(k-1)\overline{r_{ff}}}}, \tag{5.30}$$

where k is the number of components, $\overline{r_{cf}}$ is the mean value of all feature-class correlation and $\overline{r_{ff}}$ is the mean value of all feature-feature correlation. The CFS criterion is defined by [210, 211]:

$$\text{CFS} = \max_{S_k} \left[\frac{r_{cf_1} + r_{cf_2} + \cdots + r_{cf_k}}{\sqrt{k + 2(r_{f_1 f_2} + r_{f_i f_j} + \cdots + r_{f_k f_1})}} \right] \tag{5.31}$$

where the r_{cf_i} and $r_{f_i f_j}$ are referred to correlation. The combination of equation (5.30) and (5.31), which is a linear programming problem can be solved by using the three optimisation algorithms described in [212].

We used Weka environment tool [213] for applying feature selection in this work. The feature selection techniques used/described in this work such as CFS, filter-based, wrapper-based and embedded-based are available in this tool. The experimental result of applying feature selection algorithm is presented in Section 6.2.3.

5.4 Summary:

In this Chapter, we discussed general feature extraction methods that we used for extracting melanoma detection. In addition, the purpose of using feature selection and the method we use for feature selection are discussed. In the following Chapter, we will present our proposed methods for image classification.

Chapter 6

Classification

6.1 Introduction

Following the feature extraction and feature selection step, classification is applied for the diagnosis of melanoma or benign nevi. Chapter 5 discussed feature extraction and the selection algorithms used in this research. This chapter presents the classification methods for melanoma detection, using the extracted and selected features.

In Section 6.2.2, we compare the performance of five different classifiers in terms of different sets of features (colour and texture attributes). In addition, a strategy for improving accuracy is proposed.

Section 6.2.3 describes an experiment based on more comprehensive extracted features (combination of shape, colour and texture features). After applying the feature selection algorithm, the performance of nine different classifiers is assessed in terms of their sensitivity, specificity and overall accuracy. A cascade architecture including a rejection option is proposed for further improvement of the diagnostic capacities and the reliability of the system.

Finally, we investigate the use of Deep Neural Networks based on CNN-based architecture in order to investigate the feasibility of melanoma detection, using features that learned directly from input images with/without applying lesion segmentation; instead of applying traditional feature extraction algorithms.

6.2 Classification Based on Feature Extraction

Supervised learning algorithms can be applied for melanoma detection. In the data mining and machine vision contexts, supervised classification involves distinguishing a function from labelled training data [214]. In supervised classifiers, each sample of data should consist of both a vector of features and a label (e.g. melanoma = 1 and benign =0). A number of supervised classifiers that can be used for melanoma detection are as follows:

- **Support Vector Machine SVM:** Support vector machines (SVMs) have been commonly used as one of the most powerful classification algorithms in the machine learning context. Up to now, a large number of experimental studies have analysed the accuracy and precision of SVM classifiers for a wide range of biomedical applications and computer-based diagnosis systems, e.g. oral cancer using optical images, polyp detection in computed tomography (CT) colonography, micro-classification diagnosis from mammograms, and specifically in melanoma detection from dermoscopy and clinical images [76, 77, 114, 123, 125–127]. We have also used this classifier in our study. SVMs are generally classified as supervised learning models; they perform classification using a clear gap (functional margin) that is constructed from a set of N-dimensional hyper-planes to classify the given data instances into known classes [215]. An optimal classification can be obtained by the largest margin with the largest possible distance to the nearest training-sample point of any class; in practice the larger the margin, "the lower the generalization error of the classifier" [216]. Linear SVM was introduced by Vapnik in 1963. However, Vapnik et.al later proposed kernel-based functions to perform nonlinear classification, thereby fitting the optimal margin in a transformed feature space [217]. The most widely used kernels are Linear, Polynomial, Gaussian or Radial Basis Function (RBF) and Sigmoid. In this study, we used RBF kernels for training the SVM.

- **K-Nearest Neighbours (KNN):**

  the KNN algorithm is a non-parametric approach that has been deployed for classification and regression [218, 219]. This classifier predicts new cases based on the similarity measure. Therefore, the input data is classified to the k closest training samples. In other word, KNN assigns a class label by applying a majority vote from its neighbours [220]. KNN algorithms are categorized into instance-based learning, or lazy learning models and are "among the simplest of all machine learning algorithms" [221]. In order to improve accuracy, assigning weights to the contributions of the neighbours is a key point. There-

fore, the nearer neighbour can contribute more to the average than the farther neighbours.

- **Naive Bayes:** Naive Bayes NB classifiers (also known as simple Bayes and independent Bayes) are a branch of simple probabilistic classifiers in which Bayes' theorem is applied using a naive independence assumption on feature space. Naive Bayes classifiers have been studied widely since the 1950s. With appropriate pre-processing, they are reported to be competitive in this domain with more advanced methods including SVMs [222, 223]. In a learning problem, Naive Bayes classifiers are highly expandable, so that an equal number of linear parameters is needed corresponding to the number of features variables.

- **J48:**is an implemented version of the C4.5 algorithm in the Weka data mining tool. C4.5 is a classification algorithm that creates a decision tree based on a set of labelled input data [224].

- **Ensemble Classifiers:** Ensemble classifier is a combination of individual classifiers that are cooperatively trained on data set in a supervised learning problem [225]. The main ensemble predictors are Bagging, AdaBoost (boosting), Rotation Forest, Random Forest and Dagging.

  - **Bagging:** is a multi-classifier method in which random sets of features e.g. bootstrap aggregation, random decision forest or random number of instances can used for this classifier.
  - **Dagging:** is an ensemble classifier similar to bagging, which deployed split subsets of the training data for the selected base learning algorithm [213].
  - **Adaptive boosting:** (AdaBoost) can produce a sequence of classifiers. It can improve the performance of a weak classifier by dedicating a higher weight to the classifier at each iteration to make examples currently misclassified more important. Then it combines the produced classifiers by weighted classifiers to improve the accuracy. However, one disadvantage of Adaboost is that it is sensitive to noise and outliers [226].
  - **Rotation forest**: is another ensemble classification technique with the aim of improving diversity. Principal component analysis (PCA) is applied to each randomly disjoint feature subset of the input data that has been rotated [213]. This method can outperform several other ensemble methods on some benchmark classification datasets [227, 228].
  - **Random Forest:** is an ensemble classifier which grows a number of decision trees. To classify an unknown image, each individual tree independently classifies the given feature vector and the forest chooses the

classification result with the most votes, over all the trees in the forest [114]. Thus, the output of Random Forest is the class label which is the statistical mode of the class output from individual trees. Random Forest is a robust classifier in applications with noisy data, datasets containing missing values, and high-dimensional feature vectors with highly correlated features. These classifiers run efficiently on large datasets and can operate with thousands of input variables [114].

6.2.1 Dataset

We used 220 clinical images (110 melanoma and 110 benign) in the training dataset and 180 (90 melanoma and 90 benign) clinical images in the testing dataset. The image dataset was collected from on-line web resources [17–21]. Each image was cropped so that the lesion was located in the centre of the image and then each sample was resized to 512 $\times$ 512 pixels. The dataset of non-melanoma images included atypical (Compound, Junctional, Dermal, and Combined), Dysplastic, Seborrheic Keratosis, Blue Nevus, Congenital, Spitz, Halo and Neurofibromatosis. In bioinformatics applications, over-fitting is one of the fundamental issues in supervised learning classification. This phenomenon occurs when a training set is used as a fixed and small set of data rather than learning from a large amount of data; therefore, the accuracy would be too optimistic [229]. In order to overcome this issue, ten-fold cross validation was applied for training and testing of all classifiers used in our experiments.

6.2.2 Proposed Method 1:

In this section, accuracy performance of five classification algorithms were assessed based on using different feature sets. KNN ($k = 10$), Multi Layer Perceptron (MLP), Naive Bayes (NB), Random Forest (RF) and Support Vector Machine (SVM) using LibSVM ($c = 14$, Radial Base Function, $\gamma = 0.08$) were used and the accuracy of each classifier was compared. In this experiment, the following feature sets were used in order to find the best feature set among colour and texture features:

1. Combination of RGB colour and texture features (25 features),
2. Combination of HSV colour and texture features (25 features),
3. Combination of Lab colour and texture features (25 features),
4. RGB colour features (15 features),

5. HSV colour features (15 features),

6. Lab colour features (15 features),

7. Texture features (10 features).

The Receiver Operating Characteristic (ROC) curve is a tool that widely used for performance analysis of classification methods. ROC curve is a graphical plot that shows the trade-off between sensitivity and specificity. The curve is created by plotting true positive fraction (TPF), also known as sensitivity, against the false positive fraction (FPF) or 1− specificity for different thresholds [230]. The area under the ROC curve (AUC) is a commonly used factor that summarises the overall performance of a classifier between two groups (disease or non-disease) [231]. The measured AUC value is always between 0 and 1, so that a perfect classifier would give AUC of 1 and a completely random predication would give AUC of 0.5. Therefore, the greater AUC value (closer to 1) represents a better accuracy of a classification algorithms [230, 231].

AUC can be estimated using parametrically or non-parametrically methods. In a parametric method, the assumption is that the statistical distribution of the test results in both population (disease or non-disease) is known. Binormal distribution is a popular approach in this context and can be applied when test results follow normal distribution. This method generates the smooth ROC curve [232].

In non-parametric method, the resulting ROC curve is called empirical curve and obtained without any distributional assumption. The nonparametric estimate of the area under the empirical ROC curve is given by summation of the areas of the trapezoids formed by connecting the points on the ROC curve [232]. Several non-parametric methods for calculating the area under empirical ROC curve and their differences described in [233–235].

In addition to ROC analysis, measuring other performance factors such as sensitivity, specificity and accuracy are important to test the ability of a classifier for diagnosing a disease e.g. melanoma. For example, sensitivity determines how accurate the test could be at estimating a disease. Specificity determines that how correctly a classifier is to identify the patient without disease.

After performing the classification, performance of each classifier was calculated by measuring the sensitivity (Equation 6.1), the specificity (Equation 6.2), overall accuracy (Equation 6.3) and the AUC of the ROC based on ten-fold cross validation.

$$\text{Sensitivity} = \frac{\text{True Positives}}{\text{True Positives} + \text{False Negatives}} \tag{6.1}$$

$$\text{Specificity} = \frac{\text{True Negatives}}{\text{Fulse Positives + True Negatives}} \tag{6.2}$$

$$\text{Accuracy} = \frac{\text{True Positives + True Negatives}}{\text{All Instances}} \tag{6.3}$$

In this thesis, the open source software suite Weka for data mining and machine learning [213] is used for performance analysis of the classification methods. Weka uses the non-parametric Mann-Whitney statistic method to measure the AUC of ROC curve [233] and the AUC is measured at the %95 confidence interval. In statistics, confidence interval includes a range of values that implies as a proposer estimation of an unknown population parameter [236]. The range calculated from a particular dataset does not need to be obtained from the true value of the parameter [237]. In the classification literature, confidence intervals are commonly given at the %95 confidence interval [237].

Table 6.1 and Table 6.2 illustrate the performance comparison of five classifiers based on different feature sets. Table 6.1 presents the results based on colour features and Table 6.2 presents the results based on only Texture as well as combination of texture and colour features at the %95 confidence interval. In overall, the AUC of Random Forest (RF) was 85.6% and MLP classifier achieved AUC of 85.5% based on combination of RGB and texture features. Besides, using HSV colour features, RF achieved the ROC area of 85.4%. Moreover, the accuracy of these classifiers were 78.5%, 79.7% and 76.9% respectively. However, distinguishing between these classifiers is not proper as the differences are not statistical significant with %95 confidence interval.

Table 6.1: Accuracy comparison of KNN, MLP, NB, RF AND SVM based on colour features.

[1]

	RGB				HSV				Lab			
Classifier	SE	SP	ACC	AUC	SE	SP	ACC	AUC	SE	SP	ACC	AUC
KNN	75.1	70.3	72.8	81.7	77.7	72	75	81.0	82.4	52.6	68.2	69.4
MLP	74.1	78.3	76.0	83.2	74.6	73.7	74.1	81.7	80.8	46.3	64.4	66.2
NB	76.7	71.4	74.1	78.6	78.2	76.0	77.1	81	81.3	49.1	66.0	67.9
RF	77.2	74.9	76.8	84.8	76.2	77.7	76.9	85.4	75.1	54.3	65.2	69.5
SVM	80.8	74.9	77.9	77.8	80.8	74.9	77.98	77.8	87.6	48.6	69.0	68.1

Table 6.2: Accuracy comparison of KNN, MLP, NB, RF AND SVM.

	RGB + Texture				HSV + Texture				Lab + Texture				Texture			
Classifier	SE	SP	ACC	AUC	SE	SP	ACC	AUC	SE	SP	ACC	AUC	SE	SP	ACC	AUC
KNN	71.5	75.4	73.3	82.7	79.8	74.9	77.44	84.7	77.7	66.3	72.2	78.2	63.7	78.9	70.9	79.1
MLP	79.8	78.3	79.0	85.5	80.5	72.3	77.2	81.4	70.5	68	69.3	77.3	63.2	81.7	72.0	78
NB	72	76	73.9	79.8	43.3	85.1	63.3	75.9	78.2	62.3	70.6	76.8	66.3	75.4	70.6	75.5
RF	78.2	78.9	78.5	**85.6**	77.7	81.1	79.3	83.5	73.1	77.1	75	83.1	69.4	77.7	73.3	80.4
SVM	77.7	76	76.9	84.2	80.8	74.9	77.9	77.8	81.9	51.4	67.3	66.6	74.6	74.9	74.7	74.7

[1]SE is Sensitivity, SP is Specificity, ACC is Accuracy and AUC is the Area Under an ROC Curve

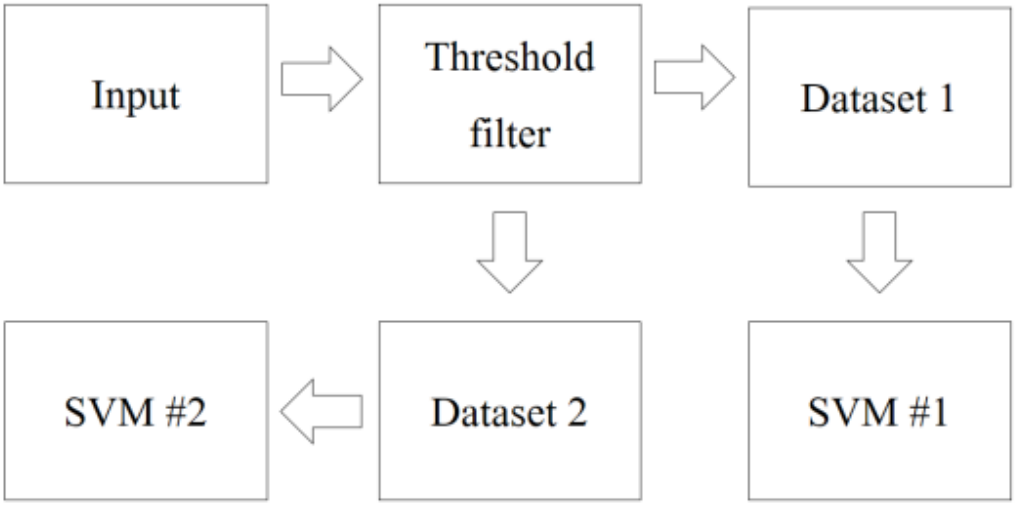

Figure 6.1: Classification using proposed cascade classifier.

To further improve the performance of classification and diagnosis, we propose a cascade classifier (Figure 6.1) as follows:

1. The input training images were divided into dataset1 and dataset2 using a threshold filter. The filter controls the threshold value of two colour features: entropy-S and entropy-V. Therefore, dataset1 had more non-melanoma images (86 benign and 15 melanoma images) and dataset2 contained more melanoma images (109 benign and 169 melanoma images).

2. An SVM classifier (SVM #1) using normalised HSV colour features (-1, 1) was applied to dataset1 to classify images into melanoma and non-melanoma. (HSV features were ranked the most effective features for SVM #1).

3. A second SVM classifier (SVM #2) using a combination of colour (RGB features) and texture features is applied to dataset2. At this stage, a correlation-based feature selection method (CFS) was used in order to find the most effective features and nine features were selected (2 RGB, 2 texture and 5 HSV features).

Using the proposed cascade classifier, we achieved sensitivity of 76.7% and specificity of 84.6%, accuracy of 80.43% with ROC area of 88.4% using ten-fold cross validation. Figure 6.3 includes the ROC curve for this classifier.

6.2.3 Proposed Method 2:

Although a number of supervised learning algorithms have been applied to melanoma diagnosis problems [8], there has been limited study of classification reliability and interpretation of the classifiers' outcome. Much of the current literature on image classification including clinical and dermoscopic images pays particular attention to producing an accurate classifier with minimum probable errors. In critical circumstances such as medical diagnosis (e.g. cancer detection or lesion segmentation) it is important to assess the reliability of classification.

One key issue to overcome this concern is to set up a rejection option, which allows the withholding of uncertain classifications via an additional decision expressing doubt [227]. For instance, if the patient needs to be checked for malignant melanoma via a smart phone (not by a doctor), it is useful to be able to reject a benign lesion image in the first instance. When there is not sufficient confidence and the cost of misclassification is high, the rejected instance can be referred on for specialist opinion and more detailed examination. The effectiveness of a reliable system can be exemplified when faulty lesion border detection occurs in the pre-processing stage. A mis-segmented instance can represent an extra portion of normal background skin due to the persistence of hair artefacts, light reflection on the lesion or combinations of various other interferences.

In this section, nine classification algorithms including SVM, KNN, Random Forest (RF), Decision Tree, Naive Bayes, J48, RBF Net, Fuzzy Rule, and MLP classifiers were assessed for their performance using the extracted features. In this experiment, we tested a combination of all extracted features. The following features were extracted from the dataset:

1. Shape (geometrical) features based on the binary mask obtained from the lesion segmentation task: area, perimeter, circularity, major and minor axis length, longest and shorter diameter, Irregularity index (IrA,IrB and IrC) (10 geometrical features in total).

2. Colour features obtained based on RGB, HSV and Lab colour channels of the segmented lesion. Colour feature extraction was performed on RGB, HSV and Lab colour spaces by measuring the average, standard deviation, Skewness, Kurtosis, and entropy of each colour channel (15 RGB, 15 HSV and 15 Lab colour features, therefore 45 RGB features in total).

3. Texture features were extracted from the GLCM. Then the following features were extracted: energy, entropy, correlation, inverse different moments, and inertia (10 texture features).

Following the feature extraction, the extracted features are selected based on the CFS feature selection algorithm (described in Section 5.3). The output of the feature selection step was a feature subset containing 51 features from the original feature dataset (8 shaper features, 13 RGB features, 11 features, 9 Lab features and 10 texture features). Table 6.3 provides a list of the selected features.

Table 6.3: List of selected features using CFS method.

Shape features	RGB features	HSV features	Lab features	Texture features
area	average-R	average-H	average-L	entropy average
perimeter	average-G	average-S	average-a	energy average
circularity	average-B	average-V	average-b	inertia average
major	std-R	std-H	std-L	inertia range
minor	std-G	std-S	std-a	entropy range
longest	std-B	std-V	skew-L	correlation average
IrA	skew-R	kurtosis-V	skew-b	correlation range
IrB	skew-G	skew- H	entropy-L	inv-diff moment-1
-	skew-B	skew-V	entropy-b	inv-diff moment-3
-	entropy-R	entropy-V	-	inv-diff moment-4
-	entropy-G	entropy-S	-	-
-	kurtosis-B	-	-	-
-	kurtosis-G	-	-	-

After performing feature selection, classification is performed. In this experiment, we compared the accuracy of nine classifiers in terms of their accuracy. The accuracy of each classifier was assessed using the testing dataset as described in Section 6.2.1 by applying ten-fold cross-validation. Table 6.4 shows the results obtained from the test analysis. It compares nine classifiers in terms of average sensitivity, specificity, overall accuracy and AUC of ROC curve based on 51 selected attributes.

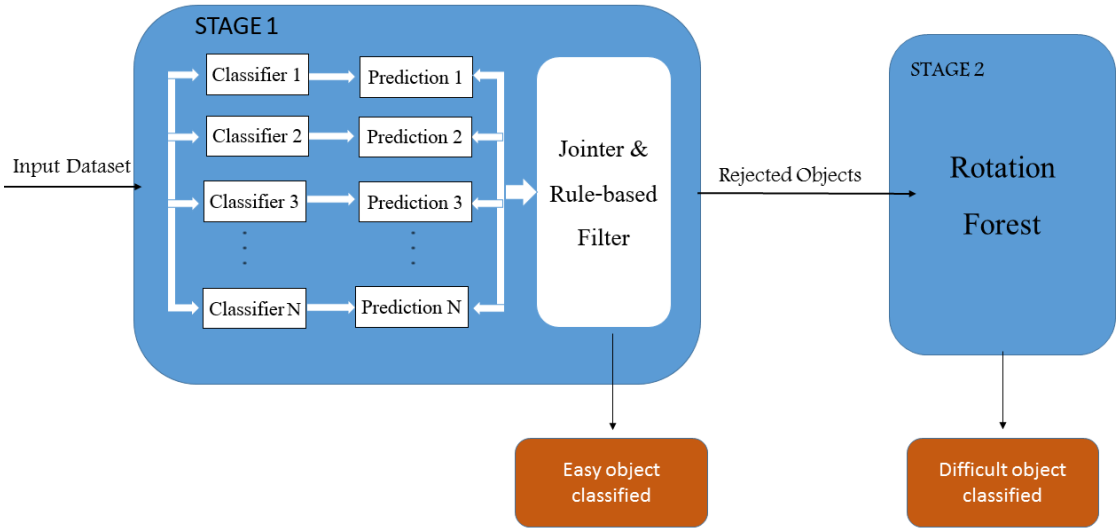

Figure 6.2: Block diagram of the second proposed cascade classifier.

Table 6.4: Testing accuracy of nine different classifiers based on combination of all features (64 features).

Classifier	**Sensitivity**	**Specificity**	**Accuracy**	**ROC Area**
MLP	76.2	72	74.18	81.5
SVM	79.8	72	76.08	85.7
KNN	80.8	77.7	79.34	80.4
RF	79.3	75.4	77.44	87.5
Decision Tree	75.1	72	73.64	78.6
NAIVE	77.7	74.3	76.08	80.3
J48	78.8	77.1	77.98	79.2
RBF_Net	69.9	80.6	75	82.8
Fuzzy_rule	74.1	75.4	74.72	79.9

Table 6.4 shows that ROC area of RF is the highest (AUC = 87.5%, ACC= 77.44%), followed by SVM (AUC = 85.7% and ACC = 76.08%). Figure 6.3 shows the ROC curve plotted for SVM, MLP and RF.

Another cascade classifier is proposed in order to improve the classification accuracy. Figure 6.2 shows the block diagram of the proposed system in which the classifier uses two stages of classification. The first stage consists of nine single classifiers including MLP, SVM, KNN, Random Forest, Decision Tree, Naive Bayes, J48, RBF Network and Fuzzy Rule. The result of each predictor is compared with the others, and majority voting as an appropriate aggregator is used to reject or accept the classified objects for further analysis. Accepted objects are those images that

are aggregated by the committee if the majority of prediction is obtained from all classifiers (five out of nine). Images with insufficient reliability, classified as rejected ones, are used in stage 2 of the classifier. The purpose of the second stage is to make better predictions on a smaller set, including the rejected instances, with the aim of improving the accuracy and reliability of the system. Training dataset for the second classifier included 95 images. Using Random Forest classifier for the second stage, the proposed cascade classifier achieved the accuracy of 83.3%, sensitivity of 85.1%, specificity of 80% and AUC of 90%.

Figure 6.3 shows the ROC curves obtained for SVM, MLP and Random Forest as well as the proposed cascade classifiers. It can be clearly observed that the second cascade classifier (Cascade2) is the best performing one over much of the regime with the higher area under the curve. However, Random Forest (RF) outperforms Cascade2 for every small FPR on the graph. Therefore, depending on where on the curve is the best place to picking the operating point, the accuracy of the Cascade2 might be better than RF or vice versa.

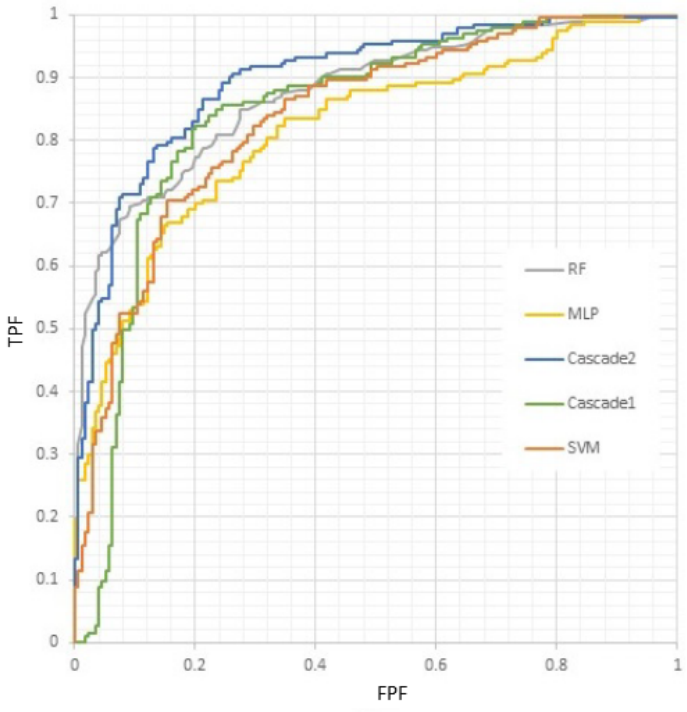

Figure 6.3: Five ROC curves for the proposed cascade classifiers (Cascade1 and Cascade2), SVM, MLP and Random Forest (RF). Cascade2 classifier with the higher area under ROC curve has a better performance over much of the regime than other classifiers.

6.2.3.1 System Implementation

In this section, the design process of the proposed cascade classifier using the KNIME tool is presented. KNIME is an open source data integration, processing, analysis and exploration platform for applying classification algorithms [238, 239]. KNIME allows the integration and use of the Weka data mining library (version 3.7) [213] where all classifiers used in this study are available. The first stage of the proposed cascade classifier was implemented using nine classifier algorithms. Each classifier reads an equal dataset input from a file-reader node. SVM, KNN, random forest, Decision Tree Learner, Naive Bayes, J48, RBF_Net and Fuzzy rule classifier nodes were selected from the Weka library (3.7) and MLP Learner was chosen from Data Mining library of KNIME. In addition, each learner and predictor was placed between an X-partitioner and an X-aggregator to apply a tenfold cross-validation procedure. Following the validation of the models, each learner node was connected to a model writer, so that a model reader could be used for applying the testing dataset. The output of predictors was then joined via eight cross joiners.

The result was a table containing 11 columns. The first column indicates the instant ID (e.g. image name), the second column is the corresponding class label, and the remaining columns are the prediction results of each classifier. A filter was used for accepting and rejecting objects. The designed filter simply consisted of two row rule-based filters with the same configuration. While the accepting filter can include those matched images with a rule e.g. when all predictions are equal, the rejecting filter can exclude rejected objects for further analysis. However, the output of the rejecting filter contains only the prediction columns and therefore no feature dataset. A joiner node was used to add the corresponding feature columns from the initial file reader. Finally, the output of the joiner was connected to the second stage prediction model (i.e. rotation forest). A corresponding classifier node for rotation forest from Weka (3.7) was selected for implementation of the classifier in stage 2.

6.3 Classification Based on Deep Learning

In this section, we propose the use of deep neural networks (DNN) for melanoma detection. DNNs can be trained using labelled image datasets. Basically, these networks learn effective visual features from images in order to distinguish whether particular objects exist in an image or not [136]. These visual features usually involve learning the weighted filters that are obtained by applying labelled (supervised learning) or unlabelled input (unsupervised learning) [240]. In this study, we investigated these two methods with respect to melanoma detection.

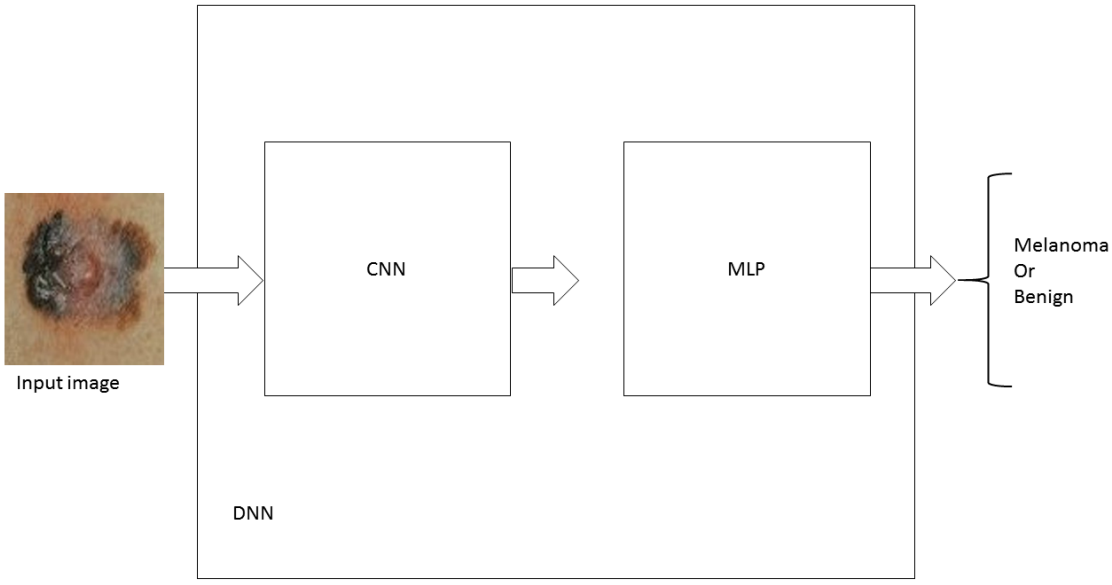

Figure 6.4: Block diagram of the DNN architecture for melanoma detection.

6.3.1 CNN Architecture

The proposed architecture is a (DNN) that consists of a two-layer CNN and a classical MLP classifier. Figure 6.4 shows a basic block diagram of the proposed CNN architecture. The input of the system is a $3 \times 64 \times 64$ array which forms a RGB image. To design the CNN, we investigated two methods: supervised and unsupervised learning.

6.3.2 Supervised Architecture

Figure 6.5 shows the block diagram of the proposed CNN architecture. The proposed model for this experiment is as follows.

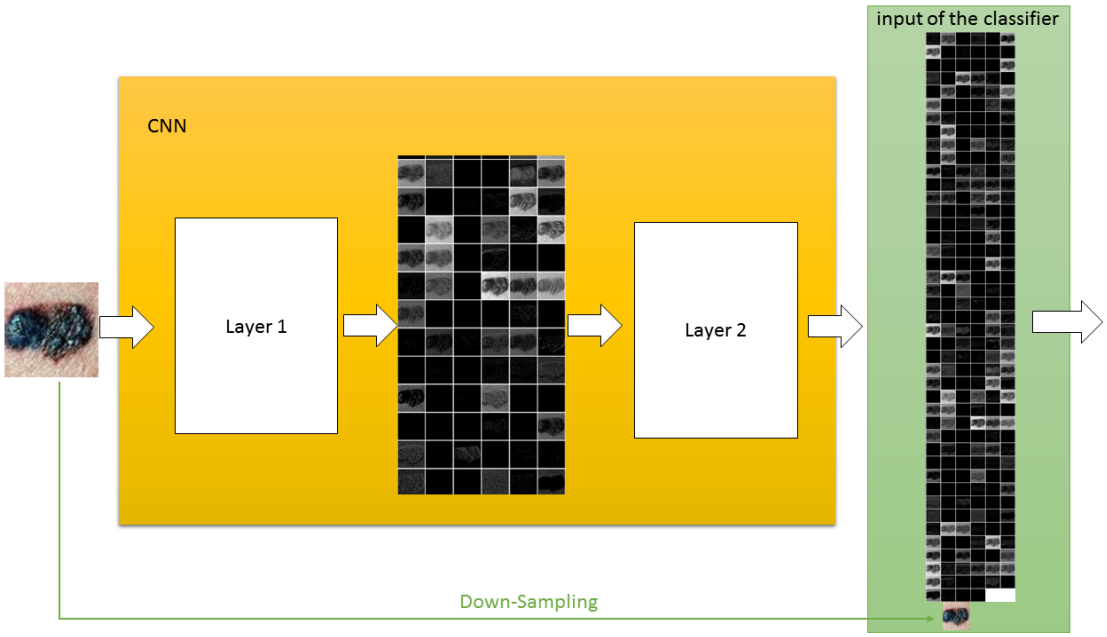

Figure 6.5: The basic block diagram of the proposed CNN architecture.

The first layer consists of:

1. Spatial-Convolutional layer: it applies a two dimensional convolution over a 3D input array (3 channels of 64×64 RGB image); the kernel (filter) size is 5×5 (width and height); it outputs 128 feature maps (y_{1_i}) with a size of $(64 - 5 + 1) \times (64 - 5 + 1) = 60 \times 60$.

2. Spatial-Max-pooling layer: $y_{p_1} = max_{n \times n}(y_{1_i})$ with $n = 2$; this down-samples the 128 generated feature maps to 128 feature maps with the size of 30×30;

3. ReLU non-linearity layer.

The second layer consists of:

1. Spatial-Convolutional layer: it applies a two dimensional convolution over the input planes which are the outputs of the previous layer ($128 \times 30 \times 30$) 2D feature maps); the kernel size is 5×5 (width and height); it produces 256 feature maps (y_{i_2}) with a size of $(30 - 5 + 1) \times (30 - 5 + 1) = 26 \times 26$;

2. Spatial-Max-Pooling layer: $y_{p_2} = max_{n \times n}(y_{i_2})$ with $n = 2$; this down-samples the 256 generated feature maps to 256 feature maps with the size of 13×13;

3. Threshold layer: $y_i = max(y_{p_2}, T)$, where the threshold $T = 0$.

Down-sampling is applied to the input image by 4×4, then the output of the down-sampled image ($3 \times 16 \times 16$) is concatenated to the output of the CNN.

In order to connect the outputs generated by the CNN and down-sampled images to the MLP classifier, first, the 2D feature maps ($256 \times 13 \times 13$) should be resized to 1D ($256 \times 13 \times 13$) arrays. In addition, the down-sampled image should be resized to a $3 \times 16 \times 16$ 1D array. Therefore, the input of the MLP classifier is $(256 \times 13 \times 13) + (3 \times 16 \times 16) = 43564$. 256 layers are considered for the hidden layers. The aggregation layer, which outputs two scores, one for each class is applied in the last layer for each feature maps. These scores are then transformed into posterior probabilities through a soft-max layer. The output of the MLP is a binary number (0= melanoma, 1= benign). The sequential layers of the MLP classifier details are as follows.

1. Linear (43564 $\rightarrow$256)
2. Add (ReLU)
3. Linear (256 $\rightarrow$2)
4. Add (Soft-Max layer)

Figure 6.6 shows a sample of the filters of layer one.

Figure 6.6: Filters of the layer 1 using supervised learning method.

6.3.3 Unsupervised Architecture

In unsupervised deep networks, back-propagation techniques are used to learn the weighted filters. However, the issue with back-projection techniques is that they train based on unlabeled data; therefore, they are unable to calculate an error signal and more computationally expensive [240]. In a recent work presented in Culurciello et al. in [136] proposed a clustering learning method based on robotic vision applications for learning the shared filters. In this study, we adapted this method to obtain the filters of the CNN for investigating an unsupervised architecture for melanoma detection application. The proposed architecture is the same as that used in the supervised learning method(described in Section 6.3.1) for building the DNNs. However, in order to obtained the weighted filters the following calculations are applied:

- k-means (clustering leaning) algorithm is applied to learn 128 filters of the first layer. Then, the filters in the first layer (obtained from supervised learning) are replaced with these learnt filters.
- k-means clustering algorithm is applied to learn 256 filters of the second layer and then the filters in the second layer are replaced with these learnt filters.

Figure 6.7 shows the obtained filters of layer one using the unsupervised learning approach.

Figure 6.7: Filters of layer one obtained by unsupervised learning method.

6.3.4 Experimental Result

The image dataset used in this experiment is same as the dataset described in Section 6.2.1. However, the size of each sample in the dataset is resized from 512×512 to 64×64 pixels due to memory restrictions and high computational operations. Figure 6.8 shows some samples of the image dataset. It can be seen that no segmentation or preprocessing is applied to this dataset. In order to investigate the power of the proposed method, we also assessed the dataset containing segmented images (see Figure 6.9) as used in the previous chapter, meaning that we compared two image datasets with the same training and testing data in two versions: a) using segmented, b) using normal images (no segmentation applied).

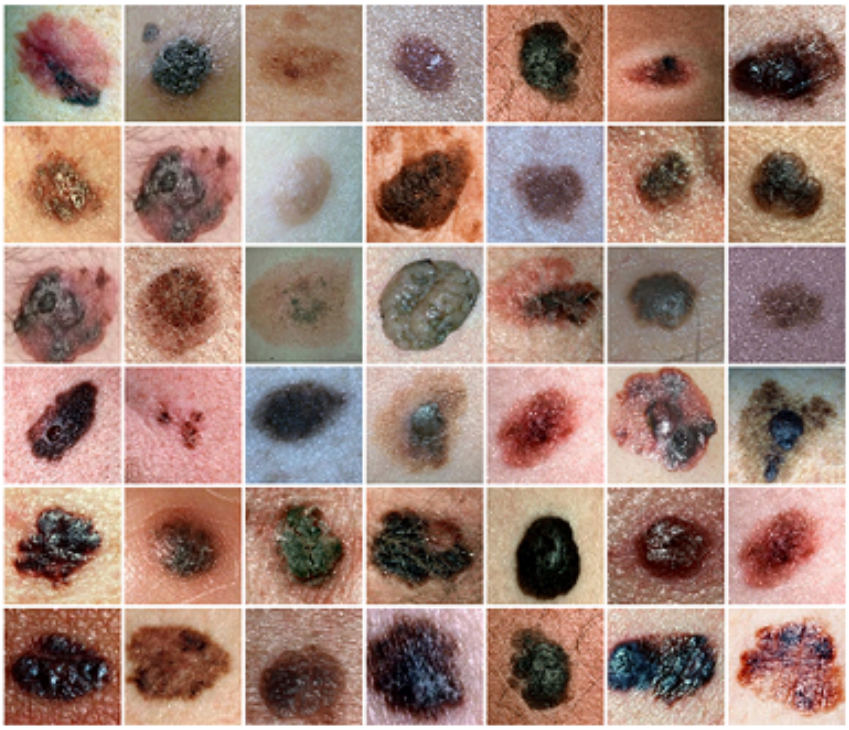

Figure 6.8: Example of images used for training and testing

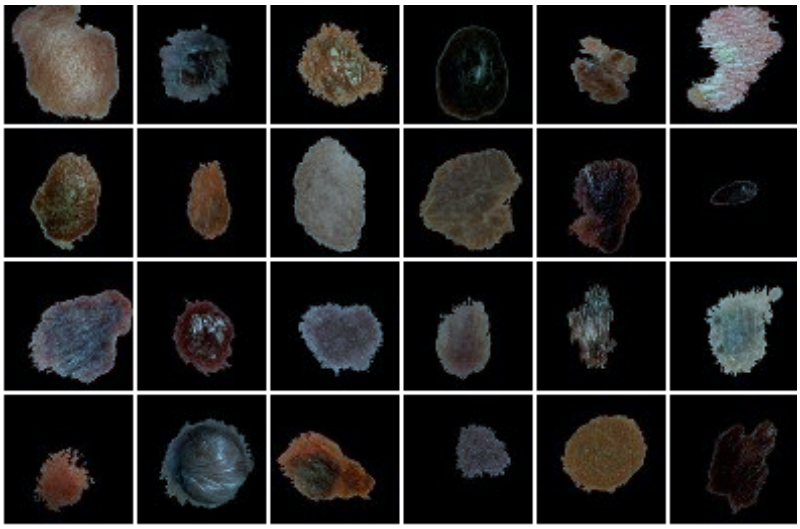

Figure 6.9: Example of image dataset containing segmented images.

Figure 6.10 shows the accuracy of the DNN based on the supervised learning method using segmented images. It shows that after 80 iterations, training is completed (100%); however, the average accuracy on the testing dataset is low(∼54%). Training procedure can be stopped when the accuracy of training is 100%.

In Figure 6.11, it can be seen that using no segmented images, testing accuracy is slightly improved (∼63%). In addition, after 120 iterations the training accuracy is around 100% which shows that the training time is significantly increased.

Using the unsupervised learning method, Figure 6.12 illustrates that average testing accuracy is around 58% using segmented images. However, training accuracy is significantly reduced from 80 iterations to 40 iterations using the unsupervised learning method. Finally, Figure 6.13 presents the accuracy testing and training of the proposed system using an unsupervised learning method without segmented images. It shows that using this method, the average testing accuracy is 78%. In addition, the training accuracy reached 100% after 10 iterations.

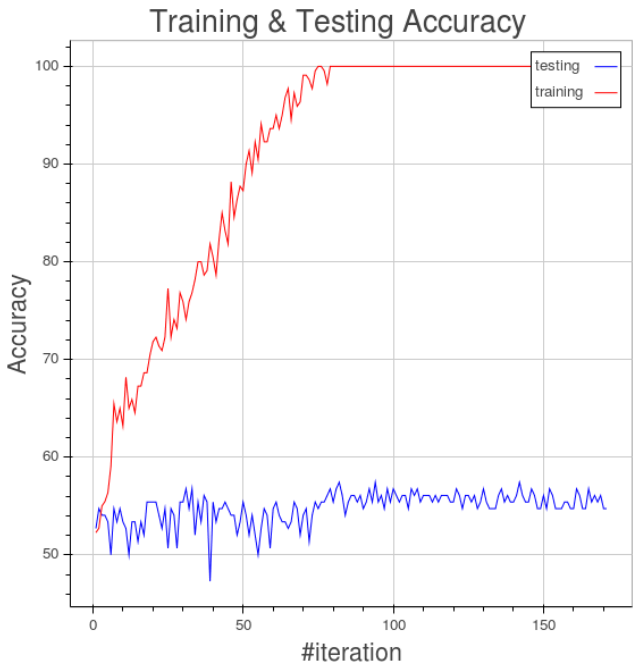

Figure 6.10: Accuracy of proposed DNNs based on supervised learning using segmented image.

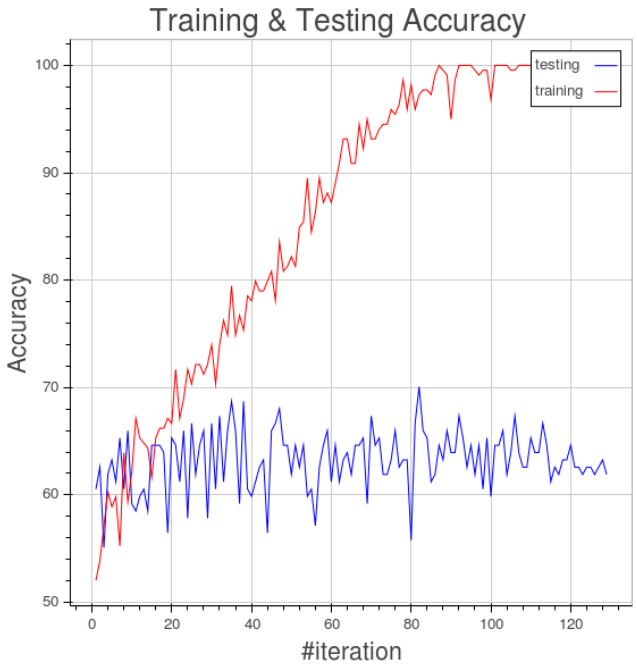

Figure 6.11: Accuracy of proposed DNN based on supervised learning without using a segmented image dataset.

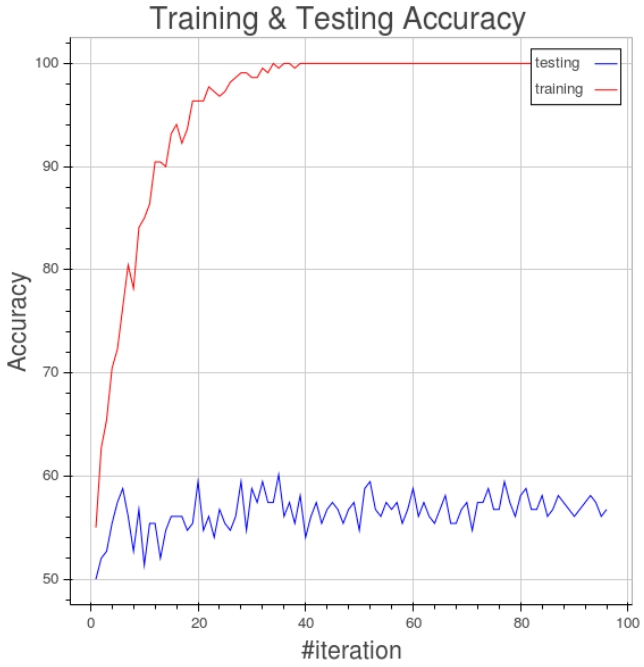

Figure 6.12: Accuracy of proposed DNN based on unsupervised learning and using a segmented image dataset.

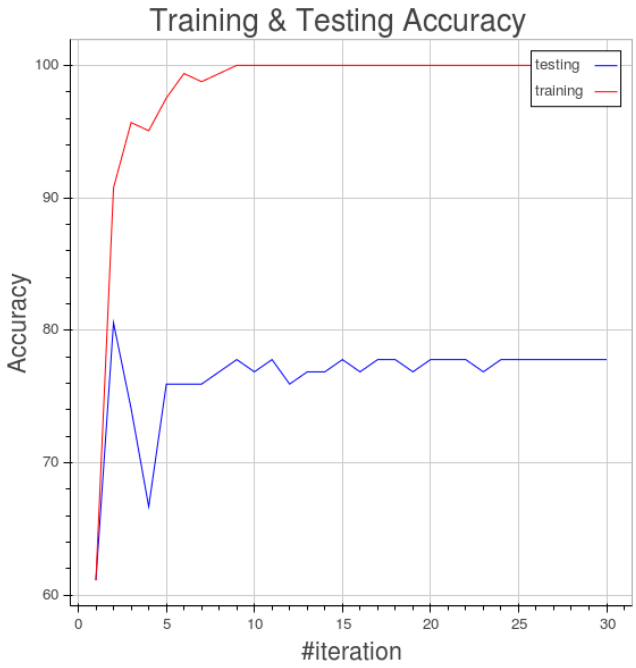

Figure 6.13: Accuracy of proposed DNN based on unsupervised learning without using a segmented image dataset.

6.4 Summary

Nine different classifiers were selected for evaluation of their diagnostic accuracy based on the shape, colour and texture features of clinical images. Experimental results showed that Random forest, Fuzzy rule and SVM classifiers outperformed the others; however, the overall performance of the classifiers was still insufficient for accurate discrimination.

We proposed two two-cascade classifiers to improve the accuracy. The second classifier proposed in this section is a multi-stage classification system including a rejection option, consisting of nine classifiers at stage one in order to reject ambiguous diagnoses. We deployed a Rotation forest classifier at the stage two and the proposed system achieved a sensitivity of 85.1%, specificity of 80%, accuracy of 83.3% with area under ROC curve of 90%. A possible area for future research would be to investigate an option to withhold a classifier decision and transfer ambiguous outcomes for further specialist assessment. In addition, we proposed a DNN model for melanoma detection. We investigated supervised and unsupervised learning methods with segmented and non-segmented images. We found that using unsupervised learning and images without segmentation, we could achieve better results in melanoma detection. Using the proposed method, the average testing accuracy was 78% and training time reduced significantly. The next chapter presents concluding remarks and suggests directions for future work.

Chapter 7

Conclusion

7.1 Introduction

In particular, this thesis focused on computer-aided diagnosis of melanoma using state-of-the-art image processing algorithms. The first two chapters provide an introduction and outline the motivation and background and provide a literature review. In Chapter 3, we investigated the implementation of image processing algorithms in embedded systems to create a basic hand-held application. Findings from the experimental results helped in the selection of appropriate embedded vision platforms for a given application. Chapter 4 proposed the extended version of edge detection methods and a framework for the implementation of the CAD system on a ZYNQ-7000 SoC. In addition, two other approaches for border detection of skin lesions were proposed. The most interesting finding was that CNN could detect lesions without requiring a pre-processing step. We tested our method based on the most challenging images in the literature. In Chapter 5, we presented the feature extraction methods used in this thesis. In Chapter 6, we discussed two novel classification algorithms to improve the accuracy and reliability of the system. In addition, we presented a DNN system for melanoma detection. Supervised and unsupervised learning methods were investigated based on segmented and non-segmented images. The rest of this chapter is structured as follows: Section 7.2 concludes our contributions and Section 7.3 suggests future research directions.

7.2 Conclusions

The contribution of this work is as follows:

- The effect of applying morphological filters and edge detection algorithms on skin lesion images in order to detect the borders of PSLs is discussed, using ZYNQ-7000 single SoC. The results show that an extended 5×5 Canny edge detection implemented on the proposed embedded platform performs better than other reported edge-based methods. Consequently, it can segment the lesion, which is an important step before image analysis and feature extraction for melanoma detection. Moreover, using C-to-FPGA technology and VIVADO HLS software, we increased the productivity and performance of the system compared with current FPGA programming approaches. However, there is a trade-off between effective edge detection and noise; this is apparent when comparing the Sobel and Prewitt operators. It was found that preprocessing of the image may, in some circumstances, result in less noise on the output. Synthesizing the IP used in this application allows real-time processing and acceleration of implementation process. This is achieved by the fact that edge detection IP is working in parallel for RGB images. The high throughput is achieved by running processes in parallel rather than at all-out speed.

- A semi-automatic border detection method was proposed and the accuracy of the algorithm was compared with two other methods. The proposed method achieved an accuracy of 89.32% (TC index) and the experimental result showed that the suggested method could be used as a proper lesion detection tool in a practical CAD system for melanoma detection. However, the main limitation is that it is not a fully automated technique.

- A CNN-based method proposed for border detection was investigated. Experimental results from this study show that lesion borders can be detected for lesion segmentation of challenging clinical images without applying preprocessing steps such as hair removal and illumination correction. The suggested method can be used as a proper automatic lesion detection tool in a practical CAD system for melanoma detection which requires minimum use of preprocessing algorithms.

- We compared all three methods proposed for border detection of skin lesions. The result showed that using testing images, CNN-based methods achieved the highest accuracy of 86.67% (Jaccard index), followed by the presented colour-based approach with an accuracy of 80.23%. The extended edge-based method (canny edge) ranked lowest with an accuracy of 65.32%.

- Chapter 6 reports on the design and evaluation of classifiers in order to discriminate melanoma from non-melanoma lesions. Nine different classifiers were selected for evaluation of their diagnostic accuracy based on the shape, colour and texture features of clinical images. Experimental results showed that Random forest, Fuzzy rule and SVM classifiers outperformed the others; however, the overall performance of the classifier was still insufficient for accurate discrimination. Therefore, we proposed a multi-stage classification including a rejection option, consisting of nine classifiers at stage one in order to reject ambiguous diagnoses. We deployed a rotation forest classifier at stage two of the Cascade2 classifier to increase the accuracy. The proposed system achieved an accuracy of 83.3% with a sensitivity of 85.1%, specificity of 80% and AUC of 90% using ten-fold cross validation. The study suggested that in a practical CAD system, it would be beneficial to have a classifier with rejection options along with reliable decision making for supervised classification. A possible area for future research would be to investigate an option to withhold a classifier decision and transfer the ambiguity for further specialist judgement. However, a large image dataset is required for further investigation of this method.

- Finally, we proposed a multi-layer DNN based on a Convolutional neural network to investigate the power of this system for melanoma detection. We compared supervised and unsupervised (clustering) approaches for training the network with two options: a) using images generated from the segmentation step; and b) without considering the segmentation step. It was found that the proposed system is able to learn the features from the images directly, in contrast with traditional image classification processes (using hand-crafted features and feature selection approach). The system achieved an average accuracy of 78%. However, we need a more comprehensive image dataset for further analysis and improvement.

7.3 Future Work

Experimental results at this stage have shown good potential for the proposed scheme. There are many avenues for pursuing further work in this area. Some of these are as follows:

- Implementing the proposed DNN on the proposed platform to create an effective portable application.
- Employing other optimization techniques for the image analysis may enhance performance. The advances in high definition media in recent years, along with high-speed embedded systems and the growth of applications in health-care systems provide the opportunity to revolutionize skin cancer diagnosis. In this work, using state-of-the-art FPGA technology as an example, we implemented a lesion border detection on an SoC and demonstrated the rapid processing power that supports such transitions.
- Investigating the implementation of the whole system as a smart-phone application and comparing its performance with the proposed embedded system.
- Training the proposed CNN-based border detection method and improving its performance using more images.
- Improving the post-processing part of the proposed CNN-based border detection so that the algorithm can detect the lesion edges more efficiently.
- Investigation of DNNs for melanoma detection using a comprehensive image dataset containing huge number of images for further analysis and improvement.
- Investigation of the use of deep learning combined with current hand-crafted feature extraction methods for better diagnosis of melanoma.

Bibliography

[1] M. J. Sneyd, C. Cameron, and B. Cox, "Individual risk of cutaneous melanoma in New Zealand: developing a clinical prediction aid," *BMC cancer*, vol. 14, no. 1, p. 359, 2014.

[2] L. A. Goldsmith, F. B. Askin, A. E. Chang, C. Cohen, J. P. Dutcher, R. S. Gilgor, S. Green, E. L. Harris, S. Havas, J. K. Robinson *et al.*, "Diagnosis and treatment of early melanoma: NIH consensus development panel on early melanoma," *JAMA*, vol. 268, no. 10, pp. 1314–1319, 1992.

[3] S. Rose, G. Argenziano, and A. Marghoob, "Melanomas difficult to diagnose via dermoscopy." *Giornale italiano di dermatologia e venereologia: organo ufficiale, Societa italiana di dermatologia e sifilografia*, vol. 145, no. 1, pp. 111–126, 2010.

[4] R. McGee, M. Elwood, H. Adam, M. Sneyd, S. Williams, and M. Tilyard, "The recognition and management of melanoma and other skin lesions by general practitioners in new zealand." *The New Zealand Medical Journal*, vol. 107, no. 982, pp. 287–290, 1994.

[5] G. R. Day and R. H. Barbour, "Automated melanoma diagnosis: where are we at?" *Skin Research and Technology*, vol. 6, no. 1, pp. 1–5, 2000.

[6] K. Doi, "Computer-aided diagnosis in medical imaging: historical review, current status and future potential," *Computerized Medical Imaging and Graphics*, vol. 31, no. 4-5, pp. 198–211, 2007.

[7] A. Pelagotti, P. Ferrara, L. Pescitelli, C. Delfino, G. Gerlini, A. Piva, and L. Borgognoni, "Multispectral imaging for early diagnosis of melanoma." International Society for Optics and Photonics, SPIE Medical Imaging, 2013, pp. 86 684A–86 684A.

[8] K. Korotkov and R. Garcia, "Computerized analysis of pigmented skin lesions: a review," *Artificial intelligence in medicine*, vol. 56, no. 2, pp. 69–90, 2012.

[9] J. Frühauf, B. Leinweber, R. Fink-Puches, V. Ahlgrimm-Siess, E. Richtig, I. Wolf, A. Niederkorn, F. Quehenberger, and R. Hofmann-Wellenhof, "Patient acceptance and diagnostic utility of automated digital image analysis of pigmented skin lesions," *Journal of the European Academy of Dermatology and Venereology*, vol. 26, no. 3, pp. 368–372, 2012.

[10] A. Tyagi, K. Miller, and M. Cockburn, "e-health tools for targeting and improving melanoma screening: a review," *Journal of Skin Cancer*, vol. 2012, 2012.

[11] L. Alpay, P. van der Boog, and A. Dumaij, "An empowerment-based approach to developing innovative e-health tools for self-management," *Health informatics journal*, vol. 17, no. 4, pp. 247–255, 2011.

[12] H. Ng, M. Sim, C. M. Tan, and C. Wong, "Wireless technologies for telemedicine," *BT Technology Journal*, vol. 24, no. 2, pp. 130–137, 2006.

[13] W. V. Stoecker, R. H. Moss, R. J. Stanley, X. Chen, K. Gupta, B. Shrestha, and P. Jella, "Automatic detection of critical dermoscopy features for malignant melanoma diagnosis," march 2010, uS Patent 7,689,016.

[14] E. Agu, P. Pedersen, D. Strong, B. Tulu, Q. He, L. Wang, and Y. Li, "The smartphone as a medical device: Assessing enablers, benefits and challenges," in *IEEE International Workshop of Internet-of-Things Networking and Control (IoT-NC)*, 2013, pp. 48–52.

[15] T. Wadhawan, N. Situ, K. Lancaster, X. Yuan, and G. Zouridakis, "SkinScan©: a portable library for melanoma detection on handheld devices," in *IEEE International Symposium on Biomedical Imaging: From Nano to Macro*, 2011, pp. 133–136.

[16] X. Chadwick, L. J. Loescher, M. Janda, and H. P. Soyer, "Mobile medical applications for melanoma risk assessment: False assurance or valuable tool?" in *47th Hawaii IEEE International Conference on System Sciences (HICSS)*, 2014, pp. 2675–2684.

[17] "Dermnet NZ," Dec 2014. [Online]. Available: http://www.dermnetnz.org

[18] "Dermatology Information System (DermIS)," Dec 2013. [Online]. Available: http://www.dermis.net

[19] "Dermquest," Dec 2014. [Online]. Available: https://www.dermquest.com

[20] "Interactive dermatology atlas," Dec 2014. [Online]. Available: http://www.dermatlas.net/atlas/index.cfm

[21] "An atlas of clinical dermatology," Dec 2014. [Online]. Available: http://www.danderm.dk/atlas/

[22] J. McGrath, R. Eady, and F. Pope, "Anatomy and organization of human skin," *Rook's textbook of dermatology*, vol. 1, pp. 3–1, 2010.

[23] M. A. Warburton, "Physically-based facial modelling and animation with wrinkles: 6 month report," 2011.

[24] M. Van der Rest and R. Garrone, "Collagen family of proteins." *The FASEB Journal*, vol. 5, no. 13, pp. 2814–2823, 1991.

[25] J. E. Lai-Cheong and J. A. McGrath, "Structure and function of skin, hair and nails," *Medicine*, vol. 37, no. 5, pp. 223–226, 2009.

[26] R. Siegel, D. Naishadham, and A. Jemal, "Cancer statistics, 2013," *CA: a Cancer Journal for Clinicians*, vol. 63, no. 1, pp. 11–30, 2013.

[27] D. Holmes, "The cancer that rises with the Sun," *Nature*, vol. 515, no. 7527, pp. S110–S111, 2014.

[28] M. of Health, "Ministry of Health. 2012. Cancer: New registrations and deaths 2009. Wellington: Ministry of Health." 2012.

[29] W. H. Organization, *Global tuberculosis control: WHO report 2010*. World Health Organization, 2010.

[30] V. Nikolaou and A. Stratigos, "Emerging trends in the epidemiology of melanoma," *British Journal of Dermatology*, vol. 170, no. 1, pp. 11–19, 2014.

[31] M. Forsea, V. Del Marmol, E. De Vries, E. Bailey, and A. Geller, "Melanoma incidence and mortality in Europe: new estimates, persistent disparities," *British journal of dermatology*, vol. 167, no. 5, pp. 1124–1130, 2012.

[32] G. V. Long, "From dismal prognosis to rising star: melanoma leads the way with new generation cancer therapies," pp. 115–116, 2015.

[33] W.-Y. Chang, A. Huang, C.-Y. Yang, C.-H. Lee, Y.-C. Chen, T.-Y. Wu, and G.-S. Chen, "Computer-aided diagnosis of skin lesions using conventional digital photography: a reliability and feasibility study," *PloS One*, vol. 8, no. 11, p. e76212, 2013.

[34] L. T. Dengel, G. R. Petroni, J. Judge, D. Chen, S. T. Acton, A. T. Schroen, and C. L. Slingluff, "Total body photography for skin cancer screening," *International Journal of Dermatology*, 2014.

[35] R. F. Uren, R. Howman-Giles, D. Chung, and J. F. Thompson, "Guidelines for lymphoscintigraphy and F18 FDG PET scans in melanoma," *Journal of Surgical Oncology*, vol. 104, no. 4, pp. 405–419, 2011.

[36] G. Danciu, S. M. Banu, and M. Ivanovici, "Scale and rotation-invariant feature extraction for color images of iris melanoma," in *13th International Conference on Optimization of Electrical and Electronic Equipment (OPTIM)*, 2012, pp. 1436–1443.

[37] Y. Xing, Y. Bronstein, M. I. Ross, R. L. Askew, J. E. Lee, J. E. Gershenwald, R. Royal, and J. N. Cormier, "Contemporary diagnostic imaging modalities for the staging and surveillance of melanoma patients: a meta-analysis," *Journal of the National Cancer Institute*, vol. 103, no. 2, pp. 129–142, 2011.

[38] M.-L. Bafounta, A. Beauchet, P. Aegerter, and P. Saiag, "Is dermoscopy (epiluminescence microscopy) useful for the diagnosis of melanoma?: Results of a meta-analysis using techniques adapted to the evaluation of diagnostic tests," *Archives of Dermatology*, vol. 137, no. 10, pp. 1343–1350, 2001.

[39] G. Argenziano, H. P. Soyer, S. Chimenti, R. Talamini, R. Corona, F. Sera, M. Binder, L. Cerroni, G. De Rosa, G. Ferrara *et al.*, "Dermoscopy of pigmented skin lesions: results of a consensus meeting via the Internet," *Journal of the American Academy of Dermatology*, vol. 48, no. 5, pp. 679–693, 2003.

[40] A. C. Geller, S. M. Swetter, K. Brooks, M.-F. Demierre, and A. L. Yaroch, "Screening, early detection, and trends for melanoma: current status (2000-2006) and future directions," *Journal of the American Academy of Dermatology*, vol. 57, no. 4, pp. 555–572, 2007.

[41] R. P. Braun, H. S. Rabinovitz, M. Oliviero, A. W. Kopf, and J.-H. Saurat, "Dermoscopy of pigmented skin lesions," *Journal of the American Academy of Dermatology*, vol. 52, no. 1, pp. 109–121, 2005.

[42] M. S. Chin, B. B. Freniere, Y.-C. Lo, J. H. Saleeby, S. P. Baker, H. M. Strom, R. A. Ignotz, J. F. Lalikos, and T. J. Fitzgerald, "Hyperspectral imaging for early detection of oxygenation and perfusion changes in irradiated skin," *Journal of Biomedical Optics*, vol. 17, no. 2, pp. 0 260 101–0 260 105, 2012.

[43] D. L. Farkas, C. Du, G. W. Fisher, C. Lau, W. Niu, E. S. Wachman, and R. M. Levenson, "Non-invasive image acquisition and advanced processing in optical bioimaging," *Computerized Medical Imaging and Graphics*, vol. 22, no. 2, pp. 89–102, 1998.

[44] O. Carrasco, R. B. Gomez, A. Chainani, and W. E. Roper, "Hyperspectral imaging applied to medical diagnoses and food safety," in *AeroSense 2003*. International Society for Optics and Photonics, 2003, pp. 215–221.

[45] J. A. Richards, "Feature reduction," in *Remote Sensing Digital Image Analysis*. Springer, 2013, pp. 343–380.

[46] J. H. Klaessens, R. De Roode, R. M. Verdaasdonk, and H. J. Noordmans, "Hyperspectral imaging system for imaging O2Hb and HHb concentration changes in tissue for various clinical applications," in *SPIE BiOS*. International Society for Optics and Photonics, 2011, pp. 78 900R–78 900R.

[47] A. Basiri, M. Nabili, S. Mathews, A. Libin, S. Groah, H. J. Noordmans, and J. C. Ramella-Roman, "Use of a multi-spectral camera in the characterization of skin wounds," *Optics Express*, vol. 18, no. 4, pp. 3244–3257, 2010.

[48] R. Jolivot, P. Vabres, and F. Marzani, "Reconstruction of hyperspectral cutaneous data from an artificial neural network-based multispectral imaging system," *Computerized Medical Imaging and Graphics*, vol. 35, no. 2, pp. 85–88, 2011.

[49] R. Jolivota, H. Nugrohob, P. Vabresac, M. Fadzilb, and F. Marzania, "Validation of a 2D multispectral camera: application to dermatology/cosmetology on a population covering five skin phototypes," in *European Conference on Biomedical Optics*. Optical Society of America, 2011, p. 808729.

[50] I. Kuzmina, I. Diebele, D. Jakovels, J. Spigulis, L. Valeine, J. Kapostinsh, and A. Berzina, "Towards noncontact skin melanoma selection by multispectral imaging analysis," *Journal of Biomedical optics*, vol. 16, no. 6, pp. 060 502–060 502, 2011.

[51] M. Emre Celebi, Q. Wen, S. Hwang, H. Iyatomi, and G. Schaefer, "Lesion border detection in dermoscopy images using ensembles of thresholding methods," *Skin Research and Technology*, vol. 19, no. 1, pp. e252–e258, 2013.

[52] A. Pelagotti, A. D. Mastio, A. D. Rosa, and A. Piva, "Multispectral imaging of paintings," *IEEE Signal Processing Magazine*, vol. 25, no. 4, pp. 27–36, 2008.

[53] M. P. Çetingül and C. Herman, "Quantification of the thermal signature of a melanoma lesion," *International Journal of Thermal Sciences*, vol. 50, no. 4, pp. 421–431, 2011.

[54] J. Spigulis, D. Jakovels, and U. Rubins, "Multi-spectral skin imaging by a consumer photo-camera," in *BiOS*. International Society for Optics and Photonics, 2010, pp. 75 570M–75 570M.

[55] Z. Tannous, M. Al-Arashi, S. Shah, and A. N. Yaroslavsky, "Delineating melanoma using multimodal polarized light imaging," *Lasers in Surgery and Medicine*, vol. 41, no. 1, pp. 10–16, 2009.

[56] J. Malvehy, S. Puig, G. Argenziano, A. A. Marghoob, H. P. Soyer *et al.*, "Dermoscopy report: proposal for standardization: results of a consensus meeting of the international dermoscopy society," *Journal of the American Academy of Dermatology*, vol. 57, no. 1, pp. 84–95, 2007.

[57] R. J. Friedman, D. S. Rigel, and A. W. Kopf, "Early detection of malignant melanoma: The role of physician examination and self-examination of the skin," *CA: a cancer journal for clinicians*, vol. 35, no. 3, pp. 130–151, 1985.

[58] W. Stolz, A. Riemann, A. Cognetta, L. Pillet, W. Abmayr, D. Holzel, P. Bilek, F. Nachbar, and M. Landthaler, "ABCD rule of dermatoscopy-a new practical method for early recognition of malignant-melanoma," *European Journal of Dermatology*, vol. 4, no. 7, pp. 521–527, 1994.

[59] N. R. Abbasi, H. M. Shaw, D. S. Rigel, R. J. Friedman, W. H. McCarthy, I. Osman, A. W. Kopf, and D. Polsky, "Early diagnosis of cutaneous melanoma: revisiting the ABCD criteria," *Jama*, vol. 292, no. 22, pp. 2771–2776, 2004.

[60] T. W. McGovern and M. S. Litaker, "Clinical predictors of malignant pigmented lesions," *The Journal of Dermatologic Surgery and Oncology*, vol. 18, no. 1, pp. 22–26, 1992.

[61] M. Keefe, D. Dick, and R. Wakeel, "A study of the value of the seven-point checklist in distinguishing benign pigmented lesions from melanoma," *Clinical and experimental dermatology*, vol. 15, no. 3, pp. 167–171, 1990.

[62] R. MacKie and V. Doherty, "Seven-point checklist for melanoma," *Clinical and experimental dermatology*, vol. 16, no. 2, pp. 151–152, 1991.

[63] Q. Abbas, M. E. Celebi, I. Fondón García, and M. Rashid, "Lesion border detection in dermoscopy images using dynamic programming," *Skin Research and Technology*, vol. 17, no. 1, pp. 91–100, 2011.

[64] T. Lee, V. Ng, R. Gallagher, A. Coldman, and D. McLean, "Dullrazor®: A software approach to hair removal from images," *Computers in Biology and Medicine*, vol. 27, no. 6, pp. 533–543, 1997.

[65] K. Tabatabaie and A. Esteki, "Independent component analysis as an effective tool for automated diagnosis of melanoma," in *IEEE Cairo International Biomedical Engineering Conference (CIBEC)*, 2008, pp. 1–4.

[66] E. Zagrouba and W. Barhoumi, "A prelimary approach for the automated recognition of malignant melanoma," *Image Anal Stereol*, vol. 23, pp. 121–135, 2004.

[67] N. Karami and A. Esteki, "Automated diagnosis of melanoma based on non-linear complexity features," in *5th Kuala Lumpur International Conference on Biomedical Engineering 2011*. Springer, 2011, pp. 270–274.

[68] K. Kiani and A. R. Sharafat, "E-shaver: An improved dullrazor® for digitally removing dark and light-colored hairs in dermoscopic images," *Computers in biology and medicine*, vol. 41, no. 3, pp. 139–145, 2011.

[69] M. T. B. Toossi, H. R. Pourreza, H. Zare, M.-H. Sigari, P. Layegh, and A. Azimi, "An effective hair removal algorithm for dermoscopy images," *Skin Research and Technology*, vol. 19, no. 3, pp. 230–235, 2013.

[70] X. Chen, R. Moss, W. Stoecker, T. Lee, R. Staenler, B. Shrestha *et al.*, "Software improvements in hair detection using DullRazor," in *6th World Congress on Melanoma*, 2005.

[71] P. Schmid-Saugeona, J. Guillodb, and J.-P. Thirana, "Towards a computer-aided diagnosis system for pigmented skin lesions," *Computerized Medical Imaging and Graphics*, vol. 27, no. 1, pp. 65–78, 2003.

[72] H. Zhou, G. Schaefer, M. E. Celebi, F. Lin, and T. Liu, "Gradient vector flow with mean shift for skin lesion segmentation," *Computerized Medical Imaging and Graphics*, vol. 35, no. 2, pp. 121–127, 2011.

[73] F.-Y. Xie, S.-Y. Qin, Z.-G. Jiang, and R.-S. Meng, "PDE-based unsupervised repair of hair-occluded information in dermoscopy images of melanoma," *Computerized Medical Imaging and Graphics*, vol. 33, no. 4, pp. 275–282, 2009.

[74] B. Amaliah, C. Fatichah, and M. R. Widyanto, "ABCD feature extraction of image dermatoscopic based on morphology analysis for melanoma skin cancer diagnosis," *Jurnal Ilmu Komputer dan Informasi*, vol. 3, no. 2, pp. 82–90, 2012.

[75] A. Chiem, A. Al-Jumaily, and R. N. Khushaba, "A novel hybrid system for skin lesion detection," in *3rd IEEE International Conference on Intelligent Sensors, Sensor Networks and Information. (ISSNIP)*, 2007, pp. 567–572.

[76] Q. Abbas, M. Emre Celebi, I. F. Garcia, and W. Ahmad, "Melanoma recognition framework based on expert definition of ABCD for dermoscopic images," *Skin Research and Technology*, vol. 19, no. 1, pp. e93–e102, 2013.

[77] R. Amelard, J. Glaister, A. Wong, and D. A. Clausi, "Melanoma decision support using lighting-corrected intuitive feature models," in *Computer Vision Techniques for the Diagnosis of Skin Cancer*. Springer, 2014, pp. 193–219.

[78] S. Shan, W. Gao, and D. Zhao, "Face recognition based on face-specific subspace," *International Journal of Imaging Systems and Technology*, vol. 13, no. 1, pp. 23–32, 2003.

[79] J. Glaister, R. Amelard, A. Wong, D. Clausi *et al.*, "MSIM: Multistage illumination modeling of dermatological photographs for illumination-corrected skin lesion analysis," *IEEE Transactions on Biomedical Engineering*, vol. 60, no. 7, pp. 1873–1883, 2013.

[80] P. G. Cavalcanti, J. Scharcanski, and C. B. Lopes, "Shading attenuation in human skin color images," in *Advances in Visual Computing*. Springer, 2010, pp. 190–198.

[81] Z. Liu and J. Zerubia, "Skin image illumination modeling and chromophore identification for melanoma diagnosis," *Physics in Medicine and Biology*, vol. 60, no. 9, p. 3415, 2015.

[82] M. E. Celebi, H. Iyatomi, G. Schaefer, and W. V. Stoecker, "Lesion border detection in dermoscopy images," *Computerized medical imaging and graphics*, vol. 33, no. 2, pp. 148–153, 2009.

[83] J. F. Alcón, C. Ciuhu, W. Ten Kate, A. Heinrich, N. Uzunbajakava, G. Krekels, D. Siem, and G. De Haan, "Automatic imaging system with decision support for inspection of pigmented skin lesions and melanoma diagnosis," *IEEE Journal of Selected Topics in Signal Processing*, vol. 3, no. 1, pp. 14–25, 2009.

[84] M. Sahu and D. Narayan, "Computer image analysis of skin lesions," *Intl J Eng Res Appl*, vol. 3, pp. 494–7, 2013.

[85] I. Maglogiannis, E. Zafiropoulos, and C. Kyranoudis, "Intelligent segmentation and classification of pigmented skin lesions in dermatological images," in *Advances in Artificial Intelligence*. Springer, 2006, pp. 214–223.

[86] I. Pirnog, R. O. Preda, C. Oprea, and C. Paleologu, "Automatic lesion segmentation for melanoma diagnostics in macroscopic images," in *23rd European Signal Processing Conference (EUSIPCO) AUTOMATIC*, 2015.

[87] P. G. Cavalcanti, Y. Yari, and J. Scharcanski, "Pigmented skin lesion segmentation on macroscopic images," in *25th International Conference of Image and Vision Computing New Zealand (IVCNZ)*, 2010, pp. 1–7.

[88] D. H. Chung and G. Sapiro, "Segmenting skin lesions with partial-differential-equations-based image processing algorithms," *IEEE Transactions on Medical Imaging*, vol. 19, no. 7, pp. 763–767, 2000.

[89] J. Tang, "A multi-direction GVF snake for the segmentation of skin cancer images," *Pattern Recognition*, vol. 42, no. 6, pp. 1172–1179, 2009.

[90] J. E. Golston, R. H. Moss, and W. V. Stoecker, "Boundary detection in skin tumor images: an overall approach and a radial search algorithm," *Pattern Recognition*, vol. 23, no. 11, pp. 1235–1247, 1990.

[91] T. Donadey, C. Serruys, A. Giron, G. Aitken, J.-P. Vignali, R. Triller, and B. Fertil, "Boundary detection of black skin tumors using an adaptive radial-based approach," in *Medical Imaging 2000*. International Society for Optics and Photonics, 2000, pp. 810–816.

[92] L. Xu, M. Jackowski, A. Goshtasby, D. Roseman, S. Bines, C. Yu, A. Dhawan, and A. Huntley, "Segmentation of skin cancer images," *Image and Vision Computing*, vol. 17, no. 1, pp. 65–74, 1999.

[93] L. T. Dengel, G. R. Petroni, J. Judge, D. Chen, S. T. Acton, A. T. Schroen, and C. L. Slingluff, "Total body photography for skin cancer screening," *International Journal of Dermatology*, vol. 54, no. 11, pp. 1250–1254, 2015.

[94] P. Sabouri, H. GholamHosseini, and J. Collins, "Border detection of skin lesions on a single system on chip," in *Advanced Technologies, Embedded and Multimedia for Human-centric Computing*. Springer, 2014, pp. 465–471.

[95] S. E. Umbaugh, R. H. Moss, and W. V. Stoecker, "Automatic color segmentation of images with application to detection of variegated coloring in skin tumors," *IEEE Engineering in Medicine and Biology Magazine*, vol. 8, no. 4, pp. 43–50, 1989.

[96] S. E. Umbaugh, R. H. Moss, and V. Stoecker, "An automatic color segmentation algorithm with application to identification of skin tumor borders," *Computerized Medical Imaging and Graphics*, vol. 16, no. 3, pp. 227–235, 1992.

[97] S. E. Umbaugh, R. H. Moss, W. V. Stoecker, and G. A. Hance, "Automatic color segmentation algorithms with application to skin tumor feature identification," *IEEE Engineering in Medicine and Biology Magazine*, vol. 12, no. 3, pp. 75–82, 1993.

[98] J. Glaister, A. Wong, D. Clausi *et al.*, "Segmentation of skin lesions from digital images using joint statistical texture distinctiveness," *IEEE Transactions on Biomedical Engineering*, vol. 61, no. 4, pp. 1220–1230, 2014.

[99] J. M. John, S. Samual, and N. M. John, "Segmentation of skin lesions from digital images using texture distinctiveness with neural network," *International Journal of Advanced Research in Computer and Communication Engineering*, vol. 3, no. 8, pp. 7777–7780, 2014.

[100] J. Tang, "A multi-direction GVF snake for the segmentation of skin cancer images," *Pattern Recognition*, vol. 42, no. 6, pp. 1172–1179, 2009.

[101] S. Jeniva and C. Santhi, "An efficient skin lesion segmentation analysis using statistical texture distinctiveness," *International Journal of Advanced Research Trends in Engineering and Technology (IJARTET)*, 2015.

[102] A. P. Dhawan and A. Sim, "Segmentation of images of skin lesions using color and texture information of surface pigmentation," *Computerized Medical Imaging and Graphics*, vol. 16, no. 3, pp. 163–177, 1992.

[103] M. Takruri, A. Al-Jumaily, and M. K. Abu Mahmoud, "Automatic recognition of melanoma using support vector machines: A study based on wavelet, curvelet and color features," in *IEEE International Conference on Industrial Automation, Information and Communications Technology (IAICT)*, 2014, pp. 70–75.

[104] G. Hance, S. E. Umbaugh, R. H. Moss, W. V. Stoecker *et al.*, "Unsupervised color image segmentation: with application to skin tumor borders," *Engineering in Medicine and Biology Magazine*, vol. 15, no. 1, pp. 104–111, 1996.

[105] N. Otsu, "A threshold selection method from gray-level histograms," *Automatica*, vol. 11, no. 285-296, pp. 23–27, 1975.

[106] T. F. Chan, L. Vese *et al.*, "Active contours without edges," *IEEE transactions on Image processing*, vol. 10, no. 2, pp. 266–277, 2001.

[107] P. G. Cavalcanti, J. Scharcanski, L. E. Di Persia, and D. H. Milone, "An ICA-based method for the segmentation of pigmented skin lesions in macroscopic images," in *Annual International Conference of the IEEE Engineering in Medicine and Biology Society, (EMBC)*, 2011, pp. 5993–5996.

[108] P. G. Cavalcanti and J. Scharcanski, "Automated prescreening of pigmented skin lesions using standard cameras," *Computerized Medical Imaging and Graphics*, vol. 35, no. 6, pp. 481–491, 2011.

[109] P. G. Cavalcanti, J. Scharcanski, C. E. Martinez, and L. E. Di Persia, "Segmentation of pigmented skin lesions using non-negative matrix factorization," in *IEEE Instrumentation and Measurement Technology Conference (I2MTC)*, 2014, pp. 72–75.

[110] E. S. Flores and J. Scharcanski, "Segmentation of pigmented melanocytic skin lesions based on learned dictionaries and normalized graph cuts," in *27th SIBGRAPI Conference on Graphics, Patterns and Images (SIBGRAPI)*, 2014, pp. 33–40.

[111] J. F. Alcón, C. Ciuhu, W. Ten Kate, A. Heinrich, N. Uzunbajakava, G. Krekels, D. Siem, and G. De Haan, "Automatic imaging system with decision support for inspection of pigmented skin lesions and melanoma diagnosis," *IEEE Journal of Selected Topics in Signal Processing*, vol. 3, no. 1, pp. 14–25, 2009.

[112] G. Joel, S.-S. Philippe, G. David, C. Jean Philippe, B. Ralph, K. Joakim, S. Jean-Hilaire, and K. Murat, "Validation of segmentation techniques for digital dermoscopy," *Skin Research and Technology*, vol. 8, no. 4, pp. 240–249, 2002.

[113] X. Li, B. Aldridge, R. Fisher, and J. Rees, "Estimating the ground truth from multiple individual segmentations incorporating prior pattern analysis with application to skin lesion segmentation," in *IEEE International Symposium on Biomedical Imaging: From Nano to Macro*, 2011, pp. 1438–1441.

[114] R. Garnavi, M. Aldeen, M. E. Celebi, G. Varigos, and S. Finch, "Border detection in dermoscopy images using hybrid thresholding on optimized color channels," *Computerized Medical Imaging and Graphics*, vol. 35, no. 2, pp. 105–115, 2011.

[115] S. Tasoulis, C. Doukas, I. Maglogiannis, and V. Plagianakos, "Classification of dermatological images using advanced clustering techniques," in *Annual International Conference of the IEEE Engineering in Medicine and Biology Society (EMBC)*, 2010, pp. 6721–6724.

[116] A. G. Manousaki, A. G. Manios, E. I. Tsompanaki, and A. D. Tosca, "Use of color texture in determining the nature of melanocytic skin lesions - a qualitative and quantitative approach," *Computers in biology and medicine*, vol. 36, no. 4, pp. 419–427, 2006.

[117] S. Tomatis, M. Carrara, A. Bono, C. Bartoli, M. Lualdi, G. Tragni, A. Colombo, and R. Marchesini, "Automated melanoma detection with a novel multispectral imaging system: results of a prospective study," *Physics in Medicine and Biology*, vol. 50, no. 8, p. 1675, 2005.

[118] Y. Faziloglu, R. J. Stanley, R. H. Moss, W. Van Stoecker, and R. P. McLean, "Colour histogram analysis for melanoma discrimination in clinical images," *Skin Research and Technology*, vol. 9, no. 2, pp. 147–156, 2003.

[119] V. T. Ng and T. K. Lee, "Measuring border irregularities of skin lesions using fractal dimensions," in *Photonics China'96*. International Society for Optics and Photonics, 1996, pp. 64–72.

[120] M. E. Celebi, H. Iyatomi, W. V. Stoecker, R. H. Moss, H. S. Rabinovitz, G. Argenziano, and H. P. Soyer, "Automatic detection of blue-white veil and related structures in dermoscopy images," *Computerized Medical Imaging and Graphics*, vol. 32, no. 8, pp. 670–677, 2008.

[121] I. Maglogiannis and C. N. Doukas, "Overview of advanced computer vision systems for skin lesions characterization," *IEEE Transactions on Information Technology in Biomedicine*, vol. 13, no. 5, pp. 721–733, 2009.

[122] R. Maurya, S. K. Singh, A. K. Maurya, and A. Kumar, "GLCM and multi class support vector machine based automated skin cancer classification," in *IEEE International Conference on Computing for Sustainable Global Development (INDIACom)*, 2014, pp. 444–447.

[123] P. G. Cavalcanti and J. Scharcanski, "Texture information in melanocytic skin lesion analysis based on standard camera images," in *Computer Vision Techniques for the Diagnosis of Skin Cancer*. Springer, 2014, pp. 221–242.

[124] A. Masood and A. Ali Al-Jumaily, "Computer aided diagnostic support system for skin cancer: a review of techniques and algorithms," *International Journal of Biomedical Imaging*, vol. 2013, 2013.

[125] A. Karargyris, O. Karargyris, and A. Pantelopoulos, "Derma/care: An advanced image-processing mobile application for monitoring skin cancer," in *IEEE 24th International Conference on Tools with Artificial Intelligence (ICTAI)*, vol. 2, 2012, pp. 1–7.

[126] A. Jukić, I. Kopriva, and A. Cichocki, "Noninvasive diagnosis of melanoma with tensor decomposition-based feature extraction from clinical color image," *Biomedical Signal Processing and Control*, vol. 8, no. 6, pp. 755–763, 2013.

[127] J. S. Marques, C. Barata, and T. Mendonca, "On the role of texture and color in the classification of dermoscopy images," in *Annual International Conference of the IEEE Engineering in Medicine and Biology Society (EMBC)*, 2012, pp. 4402–4405.

[128] M. Faal, M. Baygi, M. Hossein, and E. Kabir, "Improving the diagnostic accuracy of dysplastic and melanoma lesions using the decision template combination method," *Skin Research and Technology*, vol. 19, no. 1, pp. e113–e122, 2013.

[129] K. Jarrett, K. Kavukcuoglu, M. Ranzato, and Y. LeCun, "What is the best multi-stage architecture for object recognition?" in *IEEE 12th International Conference on Computer Vision*, 2009, pp. 2146–2153.

[130] G. E. Hinton, N. Srivastava, A. Krizhevsky, I. Sutskever, and R. R. Salakhutdinov, "Improving neural networks by preventing co-adaptation of feature detectors," *arXiv preprint arXiv:1207.0580*, 2012.

[131] Q. V. Le, "A tutorial on deep learning part 1: Nonlinear classifiers and the backpropagation algorithm," 2015.

[132] R. Frank, "The perceptron a perceiving and recognizing automaton," Technical Report 85-460-1, Cornell Aeronautical Laboratory, Tech. Rep., 1957.

[133] J. Ba and R. Caruana, "Do deep nets really need to be deep?" in *Advances in neural information processing systems*, 2014, pp. 2654–2662.

[134] P.-S. Huang, H. Avron, T. N. Sainath, V. Sindhwani, and B. Ramabhadran, "Kernel methods match deep neural networks on timit," in *IEEE International Conference on Acoustics, Speech and Signal Processing (ICASSP)*, 2014, pp. 205–209.

[135] Y. LeCun, K. Kavukcuoglu, C. Farabet *et al.*, "Convolutional networks and applications in vision." in *ISCAS*, 2010, pp. 253–256.

[136] E. Culurciello, J. Bates, A. Dundar, J. Carrasco, and C. Farabet, "Clustering learning for robotic vision," *arXiv preprint arXiv:1301.2820*, 2013.

[137] A. Krizhevsky, I. Sutskever, and G. E. Hinton, "Imagenet classification with deep convolutional neural networks," in *Advances in neural information processing systems*, 2012, pp. 1097–1105.

[138] P. Sermanet, D. Eigen, X. Zhang, M. Mathieu, R. Fergus, and Y. LeCun, "Overfeat: Integrated recognition, localization and detection using convolutional networks," *arXiv preprint arXiv:1312.6229*, 2013.

[139] K. Simonyan and A. Zisserman, "Very deep convolutional networks for large-scale image recognition," *arXiv preprint arXiv:1409.1556*, 2014.

[140] C. Szegedy, W. Liu, Y. Jia, P. Sermanet, S. Reed, D. Anguelov, D. Erhan, V. Vanhoucke, and A. Rabinovich, "Going deeper with convolutions," in *Proceedings of the IEEE Conference on Computer Vision and Pattern Recognition*, 2015, pp. 1–9.

[141] R. Girshick, J. Donahue, T. Darrell, and J. Malik, "Rich feature hierarchies for accurate object detection and semantic segmentation," in *Proceedings of the IEEE conference on computer vision and pattern recognition*, 2014, pp. 580–587.

[142] C. Couprie, C. Farabet, L. Najman, and Y. LeCun, "Indoor semantic segmentation using depth information," *arXiv preprint arXiv:1301.3572*, 2013.

[143] I. Lenz, H. Lee, and A. Saxena, "Deep learning for detecting robotic grasps," *The International Journal of Robotics Research*, vol. 34, no. 4-5, pp. 705–724, 2015.

[144] H. Pan, B. Wang, and H. Jiang, "Deep learning for object saliency detection and image segmentation," *arXiv preprint arXiv:1505.01173*, 2015.

[145] J. Long, E. Shelhamer, and T. Darrell, "Fully convolutional networks for semantic segmentation," in *Proceedings of the IEEE Conference on Computer Vision and Pattern Recognition*, 2015, pp. 3431–3440.

[146] A. Torralba and A. A. Efros, "Unbiased look at dataset bias," in *IEEE Conference on Computer Vision and Pattern Recognition (CVPR)*, 2011, pp. 1521–1528.

[147] B. A. Olshausen *et al.*, "Emergence of simple-cell receptive field properties by learning a sparse code for natural images," *Nature*, vol. 381, no. 6583, pp. 607–609, 1996.

[148] A. Coates, A. Y. Ng, and H. Lee, "An analysis of single-layer networks in unsupervised feature learning," in *International conference on artificial intelligence and statistics*, 2011, pp. 215–223.

[149] M. Havaei, A. Davy, D. Warde-Farley, A. Biard, A. Courville, Y. Bengio, C. Pal, P.-M. Jodoin, and H. Larochelle, "Brain tumor segmentation with deep neural networks," *arXiv preprint arXiv:1505.03540*, 2015.

[150] K. Petersen, M. Nielsen, P. Diao, N. Karssemeijer, and M. Lillholm, "Breast tissue segmentation and mammographic risk scoring using deep learning," in *Breast Imaging*. Springer, 2014, pp. 88–94.

[151] J. Chen, J. Cong, M. Yan, and Y. Zou, "FPGA-accelerated 3D reconstruction using compressive sensing," in *Proceedings of the ACM/SIGDA international symposium on Field Programmable Gate Arrays*, 2012, pp. 163–166.

[152] J. Xu, N. Subramanian, A. Alessio, and S. Hauck, "Impulse C vs. VHDL for accelerating tomographic reconstruction," in *18th IEEE Annual International Symposium on Field-Programmable Custom Computing Machines (FCCM)*, 2010, pp. 171–174.

[153] C. Becker, T. Waggershauser, R. Tiling, S. Weckbach, T. Johnson, O. Meissner, K. Klingenbeck-Regn, M. Reiser, and R. T. Hoffmann, "C-arm computed tomography compared with positron emission tomography/computed tomography for treatment planning before radioembolization," *Cardiovascular and Interventional Radiology*, vol. 34, no. 3, pp. 550–556, 2011.

[154] A. N. Sazish, "Efficient architectures and power modelling of multiresolution analysis algorithms on FPGA," Ph.D. dissertation, Brunel University School of Engineering and Design PhD Theses, 2011.

[155] W. Gao and Q. Kemao, "Parallel computing in experimental mechanics and optical measurement: a review," *Optics and Lasers in Engineering*, vol. 50, no. 4, pp. 608–617, 2012.

[156] J. Xing, S. Liu, and W. Zhao, "FPGA-accelerated real-time volume rendering for 3D medical image," in *3rd International Conference on Biomedical Engineering and Informatics (BMEI)*, vol. 1, 2010, pp. 273–276.

[157] N. Dahnoun and J. Brand, "DSP evolution from a teaching point of view," in *IEEE International Conference on Acoustics, Speech and Signal Processing (ICASSP)*, 2011, pp. 2900–2903.

[158] C. González, J. Resano, D. Mozos, A. Plaza, and D. Valencia, "FPGA implementation of the pixel purity index algorithm for remotely sensed hyperspectral image analysis," *EURASIP Journal on Advances in Signal Processing*, vol. 2010, p. 68, 2010.

[159] C. Rinaldi, "Performance evaluation and optimization of an OMAP platform for embedded systems," Master's thesis, Royal Institute of Technology (KTH) Stockholm, Sweden, 2011.

[160] F. Guo, M. Ding, and X. Zhang, "Fast image matching based on multicore DSP," in *International Conference on Intelligent Computation and Bio-Medical Instrumentation (ICBMI)*. IEEE, 2011, pp. 68–70.

[161] J. Noguera, S. Neuendorffer, S. Van Haastregt, J. Barba, K. Vissers, and C. Dick, "Implementation of sphere decoder for MIMO-OFDM on FPGAs using high-level synthesis tools," *Analog Integrated Circuits and Signal Processing*, vol. 69, no. 2-3, pp. 119–129, 2011.

[162] M. Jiang and D. Crookes, "Area-efficient high-speed 3D DWT processor architecture," *Electronics Letters*, vol. 43, no. 9, pp. 502–503, 2007.

[163] J. Li, C. Papachristou, and R. Shekhar, "An FPGA-based computing platform for real-time 3D medical imaging and its application to cone-beam CT reconstruction," *Journal of Imaging Science and Technology*, vol. 49, no. 3, pp. 237–245, 2005.

[164] I. Sarasola, R. Cuerdo, J. Navarrete, P. G. de Acilu, P. R. Mendes, J. Cela, J. Oller, L. Romero, and C. Willmott, "Performance evaluation of a PET demonstrator for PET-MR imaging based on monolithic LYSO: Ce scintillators," *Journal of Instrumentation*, vol. 6, no. 12, p. C12041, 2011.

[165] Y. Wang, P. Zhang, X. Cheng, and J. Cong, "An integrated and automated memory optimization flow for FPGA behavioral synthesis," in *17th IEEE Asia and South Pacific Design Automation Conference (ASP-DAC)*, 2012, pp. 257–262.

[166] J. Li, M. V. Sarunic, and L. Shannon, "Scalable, high performance fourier domain optical coherence tomography: why FPGAs and not gpgpus," in *IEEE 19th Annual International Symposium on Field-Programmable Custom Computing Machines (FCCM)*, 2011, pp. 49–56.

[167] P. Sundararajan, "High performance computing using fpgas," *Xilinx White Paper: FPGAs*, pp. 1–15, 2010.

[168] D. Göhringer, M. Birk, Y. Dasse-Tiyo, N. Ruiter, M. Hübner, and J. Becker, "Reconfigurable MPSoC versus GPU: Performance, power and energy evaluation," in *9th IEEE International Conference on Industrial Informatics (INDIN)*, 2011, pp. 848–853.

[169] A. Ahmad, B. Krill, A. Amira, and H. Rabah, "Efficient architectures for 3D HWT using dynamic partial reconfiguration," *Journal of Systems Architecture*, vol. 56, no. 8, pp. 305–316, 2010.

[170] K. P. Sarawadekar, H. B. Indana, D. Bera, and S. Banerjee, "VLSI-DSP based real time solution of DSC-SRI for an ultrasound system," *Microprocessors and Microsystems*, vol. 36, no. 1, pp. 1–12, 2012.

[171] C.-L. Fang, T.-H. Tsai, and R.-C. Kuo, "Design and implementation of a videotext extractor on dual-core platform," in *Asia-Pacific Services Computing Conference (APSCC'08 IEEE)*, 2008, pp. 896–900.

[172] M. Dossis, "A formal design framework to generate coprocessors with implementation options," *International Journal of Research and Reviews in Computer Science (IJRRCS)*, vol. 2, no. 4, 2011.

[173] A. Gregerson, A. Farmahini-Farahani, M. Schulte, W. Plishker, Z. Xie, K. Compton, and S. Bhattacharyya, "Advances in architectures and tools for FPGAs and their impact on the design of complex systems for particle physics," *Topical Workshop on Electronics for Particle Physics*, pp. 21–25, 2009.

[174] P. Krejci and M. Bradac, "Using labview for developing of mechatronic system control unit," in *Mechatronics*. Springer, 2012, pp. 309–316.

[175] H. V. Nguyen and M. H. Tran, "Synchronization algorithm and FPGA implementation for transmit-reference UWB receiver," in *2012 Fourth International Conference on Communications and Electronics (ICCE)*, 2012.

[176] D. G. Bailey, *Design for embedded image processing on FPGAs*. John Wiley & Sons, 2011.

[177] Y. Shkvarko, A. C. Atoche, and D. Torres-Roman, "Near real time enhancement of geospatial imagery via systolic implementation of neural network-adapted convex regularization techniques," *Pattern Recognition Letters*, vol. 32, no. 16, pp. 2197–2205, 2011.

[178] S. Hasan, A. Yakovlev, and S. Boussakta, "Performance efficient FPGA implementation of parallel 2-D MRI image filtering algorithms using Xilinx system generator," in *7th IEEE International Symposium on Communication Systems Networks and Digital Signal Processing (CSNDSP)*, 2010, pp. 765–769.

[179] S. A. Christe, M. Vignesh, and A. Kandaswamy, "An efficient FPGA implementation of MRI image filtering and tumor characterization using XILINX system generator," *arXiv preprint arXiv:1201.2542*, 2012.

[180] S. Hasan, S. Boussakta, and A. Yakovlev, "FPGA-based architecture for a generalized parallel 2-D MRI filtering algorithm," *Am. J. Engg. & Applied Sci*, vol. 4, no. 4, pp. 566–575, 2011.

[181] J. Cong, B. Liu, S. Neuendorffer, J. Noguera, K. Vissers, and Z. Zhang, "High-level synthesis for FPGAs: From prototyping to deployment," *IEEE Transactions on Computer-Aided Design of Integrated Circuits and Systems,*, vol. 30, no. 4, pp. 473–491, 2011.

[182] A. Bui, K.-T. Cheng, J. Cong, L. Vese, Y.-C. Wang, B. Yuan, and Y. Zou, "Platform characterization for domain-specific computing," in *17th IEEE Asia and South Pacific Design Automation Conference (ASP-DAC)*, 2012, pp. 94–99.

[183] J. Cong, K. Guruaj, M. Huang, S. Li, B. Xiao, and Y. Zou, "Domain-specific processor with 3D integration for medical image processing," in *IEEE International Conference on Application-Specific Systems, Architectures and Processors (ASAP)*, 2011, pp. 247–250.

[184] J. Cong, P. Zhang, and Y. Zou, "Combined loop transformation and hierarchy allocation for data reuse optimization," in *Proceedings of the International Conference on Computer-Aided Design*. IEEE Press, 2011, pp. 185–192.

[185] T. Papenfuss and H. Michel, "A platform for high level synthesis of memory-intensive image processing algorithms," in *Proceedings of the 19th ACM/SIGDA international symposium on Field programmable gate arrays*. ACM, 2011, pp. 75–78.

[186] A. N. Sazish, M. S. Sharif, and A. Amira, "Hardware implementation and power analysis of HWT for medical imaging," in *16th IEEE International Conference on Electronics, Circuits, and Systems (ICECS)*, Dec 2009, pp. 775–778.

[187] W. M. Chiew, F. Lin, K. Qian, and H. S. Seah, "Online volume rendering of incrementally accumulated LSCEM images for superficial oral cancer detection," *World J Clin Oncol*, vol. 2, no. 4, pp. 179–186, 2011.

[188] K. Appiah, A. Hunter, P. Dickinson, and H. Meng, "Accelerated hardware video object segmentation: From foreground detection to connected components labelling," *Computer vision and image understanding*, vol. 114, no. 11, pp. 1282–1291, 2010.

[189] Xcell journal solution for programmabe world. [Date]= Dec 2014. [Online]. Available: http://www.xilinx.com/publications/archives/xcell/Xcell82.pdf

[190] D. H. Kekre and M. S. M. Gharge, "Image segmentation using extended edge operator for mammographic images," *International Journal on Computer Science and Engineering*, vol. 2, no. 04, pp. 1086–1091, 2010.

[191] J. Canny, "A computational approach to edge detection," *IEEE Transactions on Pattern Analysis and Machine Intelligence*, no. 6, pp. 679–698, 1986.

[192] S. Ribarić, N. Pavešić *et al.*, "Efficient edge detection method by using focus of attention area," in *Proceedings of the IEEE International Symposium on Industrial Electronics (ISIE'99)*, vol. 3, 1999, pp. 1218–1223.

[193] A. P. Dhawan, *Medical image analysis*. John Wiley & Sons, 2011, vol. 31.

[194] S. E. Umbaugh, *Digital Image Processing and Analysis: Human and Computer Vision Applications with CVIPTools*. CRC press, 2010.

[195] I. H. Witten and E. Frank, *Data Mining: Practical Machine Learning Tools and Techniques*. Morgan Kaufmann, 2005.

[196] Y. Lecun, L. Bottou, Y. Bengio, and P. Haffner, "Gradient-based learning applied to document recognition," *Proceedings of the IEEE*, vol. 86, no. 11, pp. 2278–2324, Nov 1998.

[197] Y. LeCun *et al.*, "Generalization and network design strategies," *Connections in Perspective. North-Holland, Amsterdam*, pp. 143–55, 1989.

[198] C. Garcia and M. Delakis, "Convolutional face finder: A neural architecture for fast and robust face detection," *IEEE Transactions on Pattern Analysis and Machine Intelligence*, vol. 26, no. 11, pp. 1408–1423, 2004.

[199] C. Couprie, C. Farabet, L. Najman, and Y. Lecun, "Convolutional nets and watershed cuts for real-time semantic labeling of RGBD videos," *The Journal of Machine Learning Research*, vol. 15, no. 1, pp. 3489–3511, 2014.

[200] Y. LeCun, Y. Bengio, and G. Hinton, "Deep learning," *Nature*, vol. 521, no. 7553, pp. 436–444, 2015.

[201] V. Nair and G. E. Hinton, "Rectified linear units improve restricted boltzmann machines," in *Proceedings of the 27th International Conference on Machine Learning (ICML-10)*, 2010, pp. 807–814.

[202] W. K. Pratt, *Introduction to Digital Image Processing*. CRC Press, 2013.

[203] I. H. Sarker and S. Iqbal, "Content-based image retrieval using haar wavelet transform and color moment," *Smart Computing Review*, vol. 3, no. 3, pp. 155–165, 2013.

[204] J. Sun, X. Zhang, J. Cui, and L. Zhou, "Image retrieval based on color distribution entropy," *Pattern Recognition Letters*, vol. 27, no. 10, pp. 1122–1126, 2006.

[205] F. Alamdar and M. Keyvanpour, "A new color feature extraction method based on dynamic color distribution entropy of neighborhoods," *arXiv preprint arXiv:1201.3337*, 2012.

[206] A. Rao, R. K. Srihari, and Z. Zhang, "Spatial color histograms for content-based image retrieval," in *11th IEEE International Conference on Tools with Artificial Intelligence*, 1999, pp. 183–186.

[207] M. Gipp, G. Marcus, N. Harder, A. Suratanee, K. Rohr, R. König, and R. Männer, "Haralick's texture features computation accelerated by GPUs for biological applications," in *Modeling, Simulation and Optimization of Complex Processes*. Springer, 2012, pp. 127–137.

[208] H. Liu and L. Yu, "Toward integrating feature selection algorithms for classification and clustering," *IEEE Transactions on Knowledge and Data Engineering*, vol. 17, no. 4, pp. 491–502, 2005.

[209] M. A. Hall, "Correlation-based feature selection for machine learning," Ph.D. dissertation, The University of Waikato, 1999.

[210] H. T. Nguyen, S. Petrović, and K. Franke, "A comparison of feature-selection methods for intrusion detection," in *Computer Network Security*. Springer, 2010, pp. 242–255.

[211] P. D. Zegzhda, D. P. Zegzhda, and M. O. Kalinin, "A new approach to security evaluation of operating systems," in *Computer Network Security*. Springer, 2007, pp. 254–259.

[212] H. Nguyen, K. Franke, and S. Petrovic, "Optimizing a class of feature selection measures," in *NIPS 2009 Workshop on Discrete Optimization in Machine Learning: Submodularity, Sparsity & Polyhedra (DISCML), Vancouver, Canada*, 2009.

[213] M. Hall, E. Frank, G. Holmes, B. Pfahringer, P. Reutemann, and I. H. Witten, "The WEKA data mining software: an update," *ACM SIGKDD Explorations Newsletter*, vol. 11, no. 1, pp. 10–18, 2009.

[214] M. Mohri, A. Rostamizadeh, and A. Talwalkar, *Foundations of Machine Learning*. MIT press, 2012.

[215] C. Cortes and V. Vapnik, "Support-vector networks," *Machine learning*, vol. 20, no. 3, pp. 273–297, 1995.

[216] R. Priya and P. Aruna, "Review of automated diagnosis of diabetic retinopathy using the support vector machine," *International Journal of Applied Engineering Research*, vol. 1, no. 4, p. 844, 2010.

[217] B. E. Boser, I. M. Guyon, and V. N. Vapnik, "A training algorithm for optimal margin classifiers," in *Proceedings of the Fifth Annual Workshop on Computational Learning Theory*. ACM, 1992, pp. 144–152.

[218] T. M. Cover and P. E. Hart, "Nearest neighbor pattern classification," *IEEE Transactions on Information Theory*, vol. 13, no. 1, pp. 21–27, 1967.

[219] B. V. Dasarathy, "Nearest neighbor (NN) norms: NN pattern classification techniques," 1991.

[220] S. Sabitha, D. Mehrotra, and A. Bansal, "A data mining approach to improve re-accessibility and delivery of learning knowledge objects," *Interdisciplinary Journal of E-Learning and Learning Objects*, vol. 10, pp. 247–268, 2014.

[221] X. Bai, X. Yang, L. J. Latecki, W. Liu, and Z. Tu, "Learning context-sensitive shape similarity by graph transduction," *IEEE Transactions on Pattern Analysis and Machine Intelligence,*, vol. 32, no. 5, pp. 861–874, 2010.

[222] A. Masood and A. Ali Al-Jumaily, "Computer aided diagnostic support system for skin cancer: a review of techniques and algorithms," *International journal of biomedical imaging*, vol. 2013, 2013.

[223] T. R. Patil and S. Sherekar, "Performance analysis of Naive Bayes and J48 classification algorithm for data classification," *International Journal of Computer Science and Applications*, vol. 6, no. 2, pp. 256–261, 2013.

[224] Z. Xiaoliang, W. Jian, Y. Hongcan, and W. Shangzhuo, "Research and application of the improved algorithm c4. 5 on decision tree," in *IEEE International Conference on Test and Measurement (ICTM'09)*, vol. 2, 2009, pp. 184–187.

[225] A. Rahman and S. Tasnim, "Ensemble classifiers and their applications: A review," *arXiv preprint arXiv:1404.4088*, 2014.

[226] R. E. Schapire, "The boosting approach to machine learning: An overview," in *Nonlinear estimation and classification*. Springer, 2003, pp. 149–171.

[227] B. Zhang, "Reliable classification of vehicle types based on cascade classifier ensembles," *IEEE Transactions on Intelligent Transportation Systems*, vol. 14, no. 1, pp. 322–332, 2013.

[228] K.-H. Liu and D.-S. Huang, "Cancer classification using rotation forest," *Computers in Biology and Medicine*, vol. 38, no. 5, pp. 601–610, 2008.

[229] D. de Ridder, J. de Ridder, and M. J. Reinders, "Pattern recognition in bioinformatics," *Briefings in bioinformatics*, vol. 14, no. 5, pp. 633–647, 2013.

[230] N. A. Obuchowski, "Receiver operating characteristic curves and their use in radiology 1," *Radiology*, vol. 229, no. 1, pp. 3–8, 2003.

[231] X.-H. Zhou, D. K. McClish, and N. A. Obuchowski, *Statistical methods in diagnostic medicine*. John Wiley & Sons, 2009, vol. 569.

[232] S. H. Park, J. M. Goo, and C.-H. Jo, "Receiver operating characteristic (ROC) curve: practical review for radiologists," *Korean Journal of Radiology*, vol. 5, no. 1, pp. 11–18, 2004.

[233] E. R. DeLong, D. M. DeLong, and D. L. Clarke-Pearson, "Comparing the areas under two or more correlated receiver operating characteristic curves: a nonparametric approach," *Biometrics*, pp. 837–845, 1988.

[234] J. A. Hanley and B. J. McNeil, "The meaning and use of the area under a receiver operating characteristic (ROC) curve." *Radiology*, vol. 143, no. 1, pp. 29–36, 1982.

[235] D. Bamber, "The area above the ordinal dominance graph and the area below the receiver operating characteristic graph," *Journal of mathematical psychology*, vol. 12, no. 4, pp. 387–415, 1975.

[236] A. Stuart, M. G. Kendall *et al.*, *The advanced theory of statistics*. Charles Griffin, 1968.

[237] A. Field, *Discovering statistics using SPSS*. Sage publications, 2009.

[238] M. R. Berthold, N. Cebron, F. Dill, T. R. Gabriel, T. Kötter, T. Meinl, P. Ohl, C. Sieb, K. Thiel, and B. Wiswedel, *KNIME: The Konstanz information miner*. Springer, 2008.

[239] D. Morent, K. Stathatos, W.-C. Lin, and M. R. Berthold, "Comprehensive PMML preprocessing in KNIME," ACM, pp. 28–31, 2011.

[240] E. Culurciello, J. Jin, A. Dundar, and J. Bates, "An analysis of the connections between layers of deep neural networks," *arXiv preprint arXiv:1306.0152*, 2013.